



Dissertation

Ordered Equilibrium Structures
of Two-Dimensional Soft Matter Systems

ausgeführt zum Zwecke der Erlangung des akademischen Grades
eines Doktors der technischen Wissenschaften
unter der Leitung von

Ao. Univ.-Prof. Dr. Gerhard Kahl
Institut für Theoretische Physik
Technische Universität Wien

eingereicht an der Technischen Universität Wien
Fakultät für Physik

von

Dipl.-Ing. Julia Fornleitner
Matr.-Nr. 9825102
Czartoryskigasse 159/12, 1170 Wien

Wien, im November 2008

Kurzfassung

Systeme der weichen Materie nehmen beim Übergang von der flüssigen zur festen Phase selbst in zwei Dimensionen komplexe Strukturen an. Mit Hilfe von Optimierungsstrategien, die auf genetischen Algorithmen beruhen, ist es möglich, die globalen Energieminima, denen diese stabilen Konfigurationen entsprechen, auf systematische und zuverlässige Weise zu identifizieren und so die Bildung der unterschiedlichen Strukturen zu studieren. In dieser Arbeit betrachten wir drei verschiedene Systeme: erstens ein Einkomponentensystem, dessen Teilchen über ein rein repulsives Kastenpotential, das sogenannte "square-shoulder"-Potential, in Wechselwirkung stehen, zweitens eine binäre Mischung von dipolaren Kolloidteilchen und drittens ein System in dem ebenfalls dipolare Teilchen zu einem bestimmten Ausmaß von der zweidimensionalen Geometrie abweichen können und das somit einen Übergang von zwei- zu dreidimensionalen Systeme darstellt. In Hinblick auf zukünftige technologische Anwendungen untersuchen wir zusätzlich die Phononenspektren jener Gleichgewichtsstrukturen binärer Mischungen, die in Experimenten als stabile Anordnungen identifiziert werden konnten.

Abstract

Even if confined to a plane, particles of soft matter systems are able to self-assemble in a vast variety of complex equilibrium structures upon solidification. In an effort to gain deeper insight into the various strategies how particles arrange in an energetically favourable and therefore stable pattern, we investigate three exemplary model systems: a one-component system, where the particles interact via a square-shoulder potential, a binary mixture of dipolar colloids, and a system considered to be at the cross-over from two to three dimensions, where particles are allowed to detach vertically from the strict two-dimensional setup to a certain amount. By employing a search technique based on genetic algorithms, we are able to systematically explore the broad variety of ordered structures encountered for these three systems and present results that surpass previous investigations. The unbiased search strategies of genetic algorithms make us confident that the identified sequences of stable configurations are reliable and complete. With future, technologically relevant applications in mind, we determine the phonon band structures for those ordered equilibrium configurations of the binary mixture of dipolar colloids that were also encountered in experiments.

*Die Neugier steht immer an erster Stelle eines Problems,
das gelöst werden will.*

Galileo Galilei

Contents

1	Introduction	3
2	Investigated systems	7
2.1	Square-shoulder systems	8
2.2	Binary mixtures of dipolar colloids	10
2.3	Quasi-planar dipolar colloids	14
3	Statistical mechanics & Thermodynamics	17
3.1	Basic concepts of statistical mechanics	17
3.1.1	The canonical ensemble	19
3.1.2	The isobaric-isothermal ensemble	19
3.2	Thermodynamics	20
3.2.1	Thermodynamic potentials	20
3.2.2	Equilibrium and stability	23
3.3	The solid state	24
3.3.1	Description of two-dimensional lattices	24
3.3.2	Lattice sums	26
4	Theoretical Tools I: Genetic algorithms	29
4.1	General principles	29
4.2	Genetic algorithms and solidification	36
4.2.1	Parametrisation of lattice structures	37
4.2.2	The fitness function	46
5	Theoretical Tools II: Phonon band structures	47
5.1	Basic concepts of harmonic lattice dynamics	47
5.1.1	The harmonic approximation	48
5.1.2	Normal modes and dispersion relations	50
5.2	On the lattice dynamics of colloidal crystals	52

6	Results	55
6.1	Square-shoulder systems	55
6.1.1	Ordered equilibrium structures	55
6.2	Binary mixture of dipolar colloids	66
6.2.1	Ordered equilibrium structures	66
6.2.2	Comparison to simulations and experiments	80
6.2.3	Phonon band structures	85
6.3	Quasi-planar dipolar colloids	92
6.3.1	Ordered equilibrium structures	92
6.3.2	Comparison to experiments and simulations	96
7	Conclusions	103
A	An unambiguous lattice parametrisation	107
B	Square-Shoulder System: Minimum energy configurations	109
	Full sequence of MECs for $\lambda = 1.5\sigma$	109
	Full sequence of MECs for $\lambda = 3\sigma$	111
	Full sequence of MECs for $\lambda = 5\sigma$	113
	Full sequence of MECs for $\lambda = 7\sigma$	115
	Full sequence of MECs for $\lambda = 10\sigma$	117

Chapter 1

Introduction

Soft matter physics ranges among the fast expanding fields of material science of the last decade. The concentrated interest it receives is mainly due to two reasons: first, soft matter is ubiquitous in our daily lives. Many everyday substances classify as soft matter, as their rigidity against mechanical deformation is much smaller than in atomic materials. The field thus comprises a broad variety of different substances, ranging from various organic materials, like blood or protein solutions, over comestibles like milk, mayonnaise or ice cream, to all kinds of industrial products, for example paint, ink, all varieties of foam, or liquid crystals [1, 2]. This diversity of substances leads to a plethora of technological applications, warranting the applied aspect of the interest in soft matter.

The second reason for the broad attention that soft matter receives is related to its role in academic research, as their special properties make soft materials valuable model systems. Soft matter systems, also known as *colloidal dispersions* or *complex fluids*, are not only characterised by their low shear modulus, but also by their composition. A colloidal dispersion consists of mesoscopic particles suspended in a microscopic solvent. The mesoscopic particles, or *colloids*, are of a size between 1 nm and $1\text{ }\mu\text{m}$, and can be of various shapes and nature: solid particles made of silica or polystyrene, solid rods, platelets or ellipsoids all classify as colloids, as well as so called "fractal" objects like polymer chains or dendrimers. To facilitate the investigation of colloidal dispersions, *effective interactions* between colloidal particles, obtained via suitable coarse-graining procedures, are employed [3–5]: instead of taking the whole system with its huge number of particles into account, those degrees of freedom that belong to the solvent are averaged out, incorporating the influence of the much smaller solvent particles in the pair-interaction of the larger colloidal particles. If necessary, also the internal degrees of freedom of the constituent mesoscopic aggregates, e.g. the different building-blocks of a polymeric chain, can be incorporated into "effective" spherical particles [6]. By altering the salt concentration in the solvent, by varying the temperature or by changing the chemical and physical architecture of the mesoscopic particles, the effective interactions can be almost deliberately influenced by the investigator in many, well-

defined ways, leading to interaction potentials tailored to the wish of the scientist and the need of the application.

Another attractive feature of soft matter, besides the freedom to create model systems with designed interactions, are the special conditions concerning observation and handling of the materials in experiments: instead of depending on indirect methods like the various scattering techniques known from the investigation of atomic substances, the comparatively large size of the colloids allows for a direct observation of the particles' motions and behaviour via light or video microscopy [7]. Additionally, optical tweezers enable experimentalists to easily trap, move and arrange single particles, as well as they grant direct measurements of the forces acting between the colloids [8–10].

In the present work, we focus on the solidification of soft matter systems in two dimensions. Every substance, if sufficiently cooled, self-arranges in an ordered structure. Contrary to atomic materials, soft matter systems are known to exhibit a broad range of complex structures: the spectrum of ordered configurations encountered does not only comprise micellar and inverse-micellar structures [11,12]; soft matter systems can also aggregate in cluster phases [13], chain-like and layered arrangements [14,15] or gyroid phases [16–18]. There exist many different theoretical techniques to investigate the transition from the liquid to the solid phase and the thermodynamic properties of both, liquid and solid, can be determined accurately via, e.g., density functional theory [19–21], liquid state theory [22] or perturbation theory [23–25]. However, the missing tool in the theoretician's arsenal is a way to reliably predict the ordered structure a system adopts upon solidification – especially if the effective interactions of the involved particles are to represent the sole input. The conventional approaches often used for atomic substances rely on a biased preselection of possible candidate structures and are therefore insufficient for soft matter systems with their rich and unpredictable wealth of stable structures, as suitable, especially complex, candidates can be easily forgotten in the preselection process.

Knowing about the difficulties encountered by conventional approaches, genetic algorithms were introduced as an alternative way to determine the stable structures adopted upon freezing. Genetic algorithms were developed in the late 1960ies, early 1970ies by John Holland and coworkers [26], to deal with complex, high-dimensional optimisation problems in a broad range of different fields. They are modelled after natural evolutionary processes and employ mechanisms like mating, mutation and recombination, as well as Darwin's principle of "survival of the fittest" to find the optimal solution to a given problem. Genetic algorithms have been successfully applied to such different fields as economics, business administration, biology, logistics or computational sciences over decades, but their use in optimising ordered structures was acknowledged only a few years ago [27–29]. In this work, we extend and employ a search technique, introduced by Dieter Gottwald to predict stable configurations of three dimensional systems [30,31], to two-dimensional soft matter systems.

The main aim of this thesis lies with the investigation of the structural properties of three different model systems: first, a one-component system of particles interacting via a repulsive square-shoulder potential. The simple form of the interaction makes this system the ideal testing ground for our adapted and refined search technique, as emerging structures are easily classified by the number of overlapping coronas and can also be conveniently visualised. Additionally, the two-dimensional square-shoulder system has been extensively investigated in the past, using geometric arguments and computer simulations [12, 15, 32, 33]. In these previous investigations, a large number of different, often asymmetric equilibrium structures have been discovered. The revealed variety of complex structures fostered the hope that the alternative method of genetic algorithms is able to thoroughly revise – and if necessary, correct – the established phase diagram for the square-shoulder system, as it was successfully done previously in the case of three-dimensional systems of starpolymers and ionic microgels [34, 35]. Besides the square-shoulder system’s importance as a “quintessential” test system [25], it is also widely used to model the behaviour of realistic soft systems, such as polymer-grafted colloids [36] and micellar structures built of dendritic polymers [37] or diblock co-polymers [38, 39].

The second system we investigate is a binary mixture of dipolar colloidal particles. The two different species vary in size and thus in their dipole moment. Besides changing the particle size ratio, we investigate systems of different composition, leading to a systematic scan of the structural properties. The motivation for studying this particular system came from two different experimental setups, that can be seen as realisations of the model system: in the first experiment, polystyrene particles floating at an oil–water–interface are considered, which are interacting via an induced effective dipole potential. Although experiments on this setup have been performed for the one-component case only [40, 41], there exist computer simulations, mimicking the experimental setup for a binary mixture [42] and thus providing results to test our findings against. The second setup uses super-paramagnetic colloids that are suspended on a pendant water droplet. A magnetic field, applied perpendicular to the water–air–interface and trapping the particles in a two-dimensional geometry, polarises the colloids and leads to a repulsive dipolar interaction. The second experimental setup has been the centre of experimentalists’ attention for some years [43–47], yielding ample data on the static and dynamic properties of the system. Both experiments and simulations have given evidence of a rich variety of complex alloy phases, but both experience difficulties if confronted with the task of providing a systematic investigation of the system’s response to varying parameters due to, e.g. finite size effects, or local fluctuations of the density or limits in computational power. Again, we believe that our genetic algorithm-based search technique, that is highly appropriate for optimisations in complex search spaces, is the ideal method to complete the results of these studies.

The third system covered in this thesis considers the cross-over from a two- to a three-dimensional setup: colloidal particles are trapped in a thin cell, slightly thicker than the particle’s

diameter. The colloids are thus allowed to deviate from the two-dimensional plane and buckle in the vertical direction. The particles are super-paramagnetic and interact via an ideal dipole-dipole potential as an external magnetic field is used to induce magnetic moments perpendicular to the plane in the colloids. Depending on the cell thickness, the interaction is either purely repulsive, softened repulsive, or attractive at small distances, leading to a variety of solid phases [9,10]. Our genetic algorithm-based search technique was included in the survey as a third, complementary method, besides the current investigations by experiment and simulations.

We have chosen these three systems in particular with respect to their realisability in experiments and their relevance as model systems. In this way, we can guarantee the verification of our findings, not only by comparison to results obtained in computer simulations, but also to experimental data on colloidal systems. With the possibility of future applications in mind, we also investigate the dynamic and elastic properties of some of the emerging structures by determining their phonon band structures.

This work is organised as follows:

Chapter 2 introduces the investigated systems. The interparticle potentials used in our studies are presented along with a discussion of their relevance as model systems and their realisations in experiments.

Chapter 3 provides the theoretical concepts of statistical mechanics and thermodynamics essential to the understanding of this work. A description of ordered solid states and the calculation of their defining properties complete the chapter.

Chapter 4 is dedicated to the method employed to determine the equilibrium structures – genetic algorithms. An introduction to their general concepts and the specific implementations necessary to adapt a generic genetic algorithm to the problem of finding stable solid structures is given in this chapter.

Chapter 5 gives an introduction to the harmonic theory of lattice dynamics. It covers the calculation of the dispersion curves or phonon band structures of harmonic crystals and also includes a short overview on the lattice dynamics of solid colloidal dispersions.

Chapter 6 presents the results obtained for the systems introduced in chapter 2: we discuss the identified sequences of minimum energy configurations of all three systems and study the phonon band structures obtained for those stable structures of the binary mixture of dipolar colloids that have been verified in experiments.

Chapter 7 contains a brief summary of the results and provides the conclusions drawn from this work. A short outlook on future work completes the last chapter.

Chapter 2

Investigated systems

In the following chapter, we present the three systems investigated in this thesis: in Section 2.1, we start with the one-component, two-dimensional square-shoulder system. The next section is dedicated to binary monolayers of dipolar, colloidal particles and in Section 2.3 a one-component system of dipolar colloids is considered, which represents a link between two- and three-dimensional systems. Besides introducing the respective interparticle potentials, we also discuss their relevance as model systems and introduce their various realisations in experiments.

All systems have the following features in common: They classify as soft matter or *colloidal dispersions*, meaning that each of the three systems investigated in this thesis consists of mesoscopic particles, with a size ranging from 1 nm to $1\text{ }\mu\text{m}$, which are suspended in a microscopic solvent.

Neither the behaviour of the considerably faster and smaller solvent particles, nor the inner structure of the mesoscopic particles is of direct concern in our investigations. Both influences are therefore subsumed in suitably coarse-grained, effective pair potentials that describe the interaction between spherical, effective particles [5].

These effective potentials $\Phi(\mathbf{r})$ are all radially symmetric and isotropic. The interaction between two particles is therefore only dependent on their distance $r = |\mathbf{r}|$, so that

$$\Phi(\mathbf{r}) = \Phi(r) \quad .$$

We are also able to define an energy scale ε in all three cases, so that the interparticle potential can be written as

$$\Phi(\mathbf{r}) = \varepsilon f(r) \quad .$$

Furthermore, all investigated particles exhibit an impenetrable hard-core region of diameter σ , which is called on as a length scale.

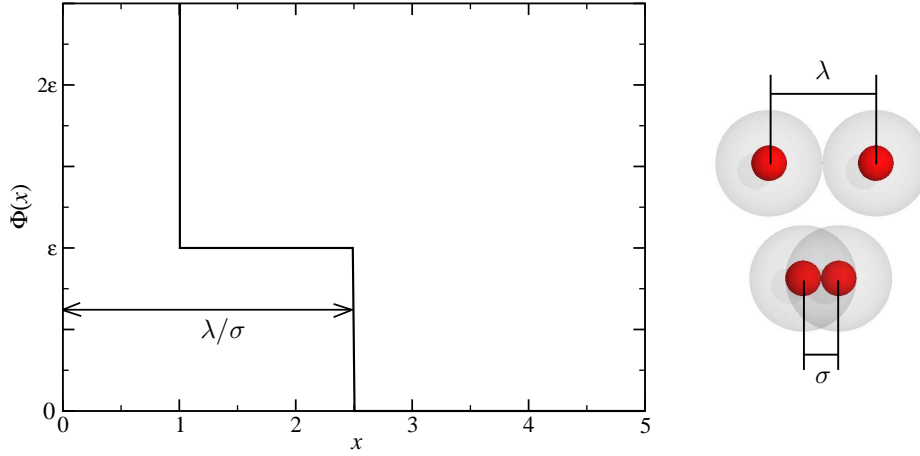


Figure 2.1: *Pair potential for the square-shoulder system, corresponding to equation (2.1) (left panel), and the two configurations corresponding to the two characteristic lengths of the system (right panel).*

The pair potentials of all three systems thus are of the same general form,

$$\Phi(\mathbf{r}) = \Phi\left(x = \frac{r}{\sigma}\right) = \begin{cases} \infty & x \leq 1 \\ \varepsilon g(x) & x > 1 \end{cases},$$

with $g(x)$ being a dimensionless function.

2.1 Square-shoulder systems

In a square-shoulder system, hard particles of diameter σ interact via a soft, repulsive, step-shaped corona of width λ and height ε . The spherically symmetric pair potential for this system reads as

$$\Phi(x) = \begin{cases} \infty & x \leq 1 \\ \varepsilon & 1 < x < \lambda/\sigma \\ 0 & \lambda/\sigma \leq x \end{cases}, \quad (2.1)$$

(see figure 2.1, left panel). We choose the particle diameter σ to act as a length scale in this system and the shoulder height ε as an energy scale. The pair potential (2.1) is thus characterised by the height of the shoulder ε and by the ratio of shoulder width to particle diameter λ/σ . The right panel of figure 2.1 shows the two configurations typical to the defining lengths λ and σ of the system: first, at the top of the right panel in figure 2.1, a configuration where the repulsive coronas of two particles are just in touch with each other, and second, a schematic representation of two particles in hard-core contact (see figure 2.1, right panel, bottom).

The square-shoulder potential with its short repulsive step is typical for steric interactions

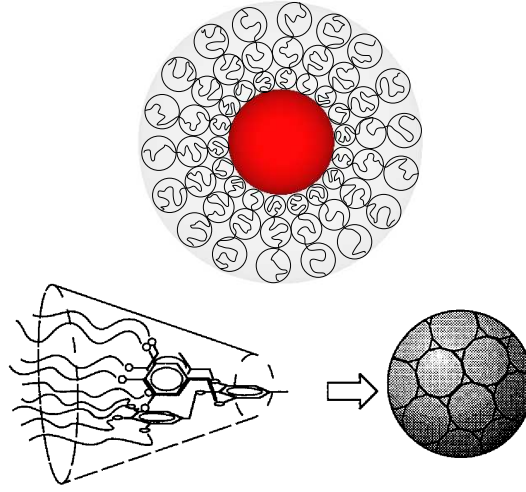


Figure 2.2: *Schematic representation of two systems exhibiting a distinct core-corona architecture: A polymer-grafted colloid (top panel) and a micell assembled by dendritic polymers (bottom panel, taken from ref. [37]).*

and is therefore often used to model the behaviour of particles that exhibit a distinct core-corona architecture. A common example for this particle class are polymer-grafted colloids, i.e. hard, colloidal particles with a brush of flexible polymer chains attached to their surface [36]. A schematic representation of such a polymer-grafted colloid is given in the top panel of figure 2.2. The colloids themselves are impenetrable, thus forming the hard core visible in the potential. The soft coronas on the other hand, that consist of the polymer chains, can interpenetrate at some energy cost, leading to the soft, repulsive, step-shaped shoulder adjacent to the hard-core region. The parameters of the potential – the height of the repulsive step ϵ and the shoulder width λ – can be controlled by changes in the grafting density and in the length of the polymer chains, respectively.

Other examples of particles whose pair interaction has been modelled using the square-shoulder potential are micells of dendritic polymers [37] and diblock co-polymers [38, 39]. The micells formed by these two types of polymers display two distinct regions: the inner core, composed of the solvophobic parts of the constituent polymers, is characterised by a high polymer density, whereas the solvophilic polymer groups form a diffuse corona considerably less dense and thus interpenetrable, leading to the characteristic inner architecture. For a schematic representation of a micell assembled by dendritic polymers see figure 2.2, bottom panel. Other systems, where the square-shoulder potential has been successfully employed to model the particle interactions, include Cs and Ce [48], water [49, 50], and electron liquids in weak magnetic fields [51, 52].

In addition to its role as a model for experimentally realisable soft systems, the square-shoulder potential constitutes a valuable potential in the investigations of solid-solid transitions. Due to the sharp cutoff and the flat plateau in the pair potential, the square-shoulder system is extremely sensitive to changes in the pair-correlation function [25]. Its simple potential form makes it also especially easy to interpret obtained results, as the energy of an emerging lattice is simply given

as the number of overlaps of the particles' coronas.

Besides the above mentioned applications of the square-shoulder system, we have chosen to investigate this particular potential due to another reason: it is a well tested system. Results of previous investigations on the two-dimensional square-shoulder system employing various different methods, such as computer simulations [12, 15, 32, 33], geometric analysis [15, 33], or mean-field methods [12], show a remarkably rich variety of stable structures, providing us with ample data to test our findings against. Additionally, the often asymmetric structures encountered and the known drawbacks of the employed methods raise doubts whether the spectra of stable structures determined in these previous studies are complete, thus leading to the hope that our method of genetic algorithms will offer deeper insight on the square-shoulder system's strategies to form stable structures.

2.2 Binary mixtures of dipolar colloids

The second class of systems studied in this thesis is a binary mixture of polystyrene particles floating at an oil–water interface to ensure the two-dimensional geometry of the setup. The interaction between the particles of the species A and B , which differ in size, is given by an effective dipole-dipole-potential of the form

$$\Psi_{ij}(r) = \begin{cases} \infty & r \leq (R_i + R_j) \\ \Psi_{ij}^I = \frac{P_i P_j}{16\pi\epsilon R_i R_j} \frac{1}{r} \ln \left[\frac{r^2 - (R_i - R_j)^2}{r^2 - (R_i + R_j)^2} \right] & r > (R_i + R_j) \end{cases} \quad i, j = A, B \quad . \quad (2.2)$$

In (2.2), ϵ denotes the dielectric constant of water, R_i , $i = A$ or B , stands for the radius of the particle species i and P_i for the corresponding dipole moment [42].

These effective interactions are believed to have their origin in the formation of surface charge dipoles on the particle's interface with the oil phase, as indicated in figure 2.3 [53]: On contact with water, hydrophilic sulfate head groups on the particles' surface dissociate and surface charge dipoles are formed. Since the particles are covered by a thin water film when poured into the setup, dipole charges are found on the whole surface of the particle. In the aqueous phase, the interaction of these dipoles is shielded due to the small Debye length in water, resulting in an effective dipole moment. This net dipole moment can be calculated via the vector sum of all the surface charge dipoles sitting at the particles' interface with the oil phase (see figure 2.3). Computer simulations were able to affirm the potential form (2.2), as they reproduced the equilibrium structures observed in experiments on a one-component system of polystyrene particles when using this particular potential [40, 41, 53].

The interaction potentials given in (2.2) can be simplified by introducing the diameter of the larger species $\sigma_A = 2R_A$ as a length scale to the system, so that $x = r/\sigma_A$. Additionally, we set

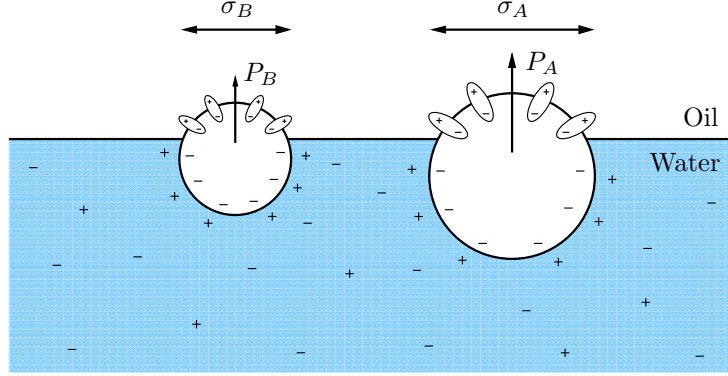


Figure 2.3: Two polystyrene particles of different size floating at an oil-water interface. The net dipole moments P_A and P_B are given by the vector sums of the surface charge dipoles sitting on the particle-oil-interface (picture inspired by ref. [53]).

$z = R_B/R_A \leq 1$, and, following the arguments presented in reference [42], assume

$$P_i = \alpha R_i^{\frac{n+2}{2}} \quad . \quad (2.3)$$

With these parameters, the interactions $\Psi_{ij}^I(r)$ of equation (2.2) can finally be written as

$$\Phi_{AA}^I(x) = \varepsilon_I \frac{1}{x} \ln \left[\frac{x^2}{x^2 - 1} \right] \quad \text{for } x \geq 1; \quad (2.4)$$

$$\Phi_{BB}^I(x) = \varepsilon_I \frac{z^n}{x} \ln \left[\frac{x^2}{x^2 - z^2} \right] \quad \text{for } x \geq z; \quad (2.5)$$

$$\Phi_{AB}^I(x) = \varepsilon_I \frac{z^{n/2}}{x} \ln \left[\frac{4x^2 - (1 - z)^2}{4x^2 - (1 + z)^2} \right] \quad \text{for } x \geq (1 + z)/2 \quad , \quad (2.6)$$

with a common prefactor

$$\varepsilon_I = \frac{\alpha^2}{16\pi\epsilon} R_A^n \quad .$$

The two potential parameters z and n have a distinct influence on the form of the interaction potential. In the following considerations, the interaction between large particles Φ_{AA}^I acts as a reference, since it depends neither on z nor on n . If the particle size ratio $z = 1$, all Φ_{ij}^I coincide, representing the trivial one-component case. Decreasing z corresponds to shrinking the size of one of the particle species and thus weakens the adjoint repulsive tail in $\Phi_{BB}^I(x)$ and $\Phi_{AB}^I(x)$, as the particles' dipole moment was chosen to be proportional to the radius of the colloid in equation (2.3) (see figure 2.4). The exponent n , on the other hand, changes the strength of the repulsive tail, without changing its position: the smaller the exponent n , the softer is the interaction between the particles. Following the argumentation put forward in reference [42], we distinguish between two different interaction regimes in our survey, corresponding to two values of the exponent n : a

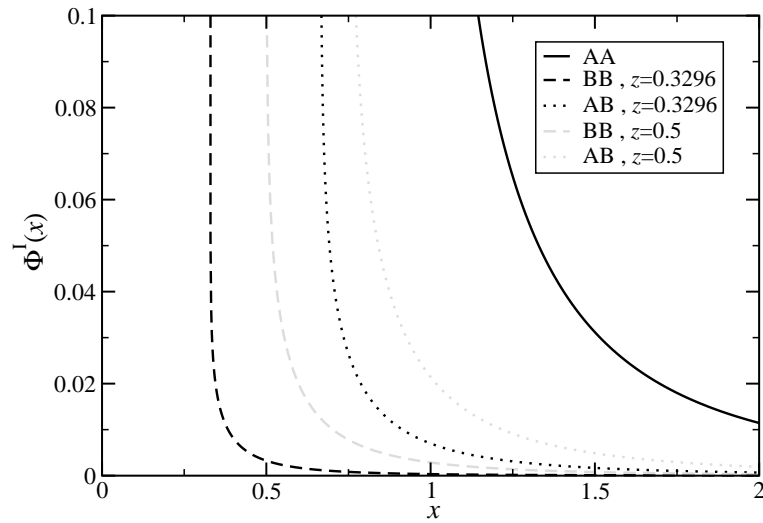


Figure 2.4: Interaction potentials Φ_{ij}^I in a binary mixture of dipolar colloids floating at an oil-water interface for different values of the particle size ratio z for $n = 3$.

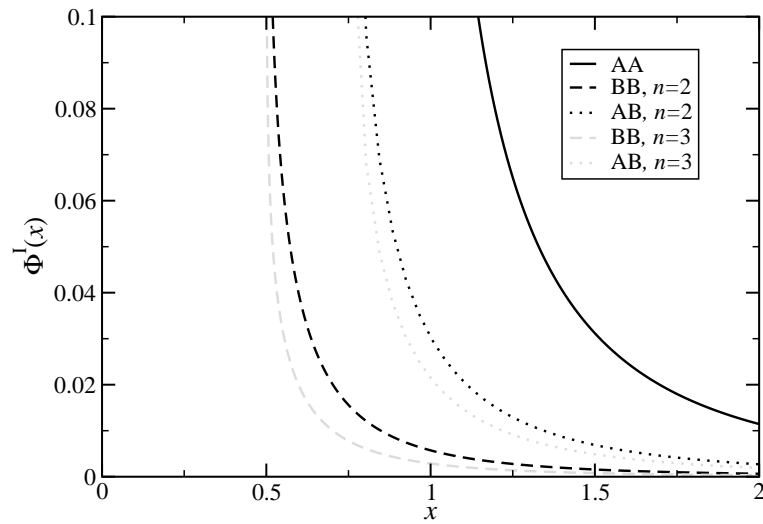


Figure 2.5: Interaction potentials Φ_{ij}^I in a binary mixture of dipolar colloids floating at an oil-water interface for different values of the exponent n and for a particle size ratio $z = 0.5$

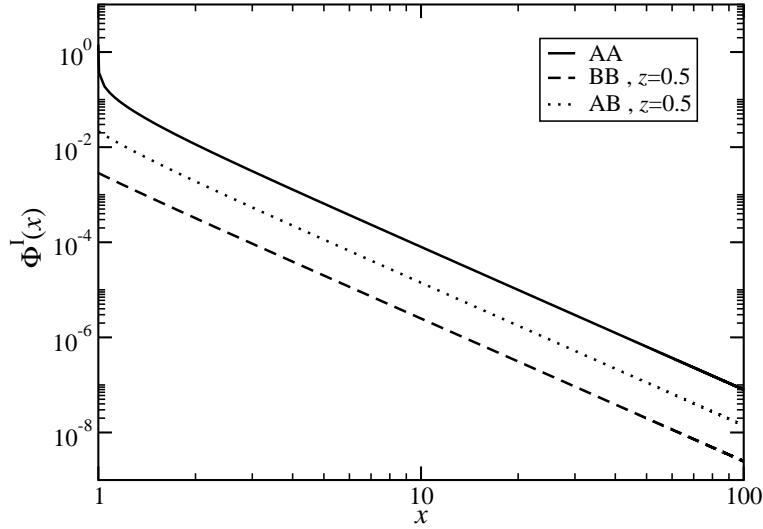


Figure 2.6: *Double logarithmic plots of the interaction potentials Φ_{ij}^I in a binary mixture of dipolar colloids floating at an oil-water interface for $z = 0.5$. The power-law dependence of the interaction for large and intermediate values of x is clearly visible, as well as deviations from the ideal dipole behaviour at short distances.*

”weak” interaction regime, where the dipolar moment scales with the particles surface ($n = 2$); and a ”strong” interaction regime with $n = 3$ (see figure 2.5).

A double logarithmic plot of the interactions (2.4)-(2.6) reveals that the potentials deviate from the ideal $1/r^3$ -behaviour of a pure dipole-dipole-interaction only at small distances (see figure 2.6). This behaviour becomes more obvious as we expand the logarithms in (2.4)-(2.6) in a Taylor-series, yielding

$$\Phi_{ij}^I(x) \sim \frac{(z_i z_j)^{\frac{n+2}{2}}}{x^3} + \mathcal{O}(x^{-5}) \quad , \quad i, j = A, B \quad (2.7)$$

with $z_A = 1$ and $z_B = z$, leading to a functional form that represents an ideal dipole-dipole interaction.

Retaining the first term in equation (2.7), the interaction potentials correspond to another system, extensively investigated in the past [43–47, 54, 55]: In their experimental realisation of this system, Ebert et al. [47] use super-paramagnetic colloidal particles, suspended on a pendant water droplet to ensure the two-dimensional geometry (see figure 2.7). By applying a strong external magnetic field \mathbf{B} perpendicular to the plane of the droplet, magnetic moments are induced in the particles, which align parallel to the external field,

$$\mathbf{M}_i = \chi_i \mathbf{B} \quad ,$$

where χ_i is the susceptibility of a particle of species i , and $i = A$ or B . Introducing the susceptibility ratio $m_i = \chi_i / \chi_A$, the dipole-dipole potentials acting between the particles can be written

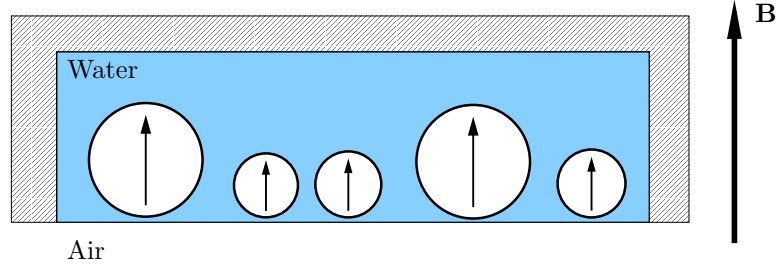


Figure 2.7: Schematic representation of the experimental setup described in ref. [47]: super-paramagnetic colloids are trapped at the air-water interface in a pendant water droplet. An external magnetic field \mathbf{B} is used to tune the interactions between the particles (picture inspired by ref. [47]).

as

$$\Phi_{ij}^{\text{II}}(x) = \varepsilon_{\text{II}} \frac{m_i m_j}{x^3} \quad (2.8)$$

with

$$\varepsilon_{\text{II}} = \frac{\mu_0 \chi_A^2}{32\pi R_A^2} B^2 \quad ,$$

acting as an energy scale and $x = r/\sigma_A$ being the reduced distance between the interacting particles.

At low and intermediate densities, where the particles are separated sufficiently far from each other, the two sets of potentials, (2.4)-(2.6) and (2.8) are practically identical and are therefore expected to lead to the same particle arrangements. The equivalence relation between the particle size ratio z and the susceptibility ratio m , that allows for a direct comparison of results obtained in both cases, is given by

$$m_i B \Leftrightarrow z_i^{(n+2)/2} \quad .$$

Furthermore, one of the two potential parameters used to describe system I becomes superfluous in (2.7), as, e.g., a change in the exponent, $n \rightarrow \tilde{n}$, can always be translated to a change in the particle size ratio,

$$n \rightarrow \tilde{n} \Leftrightarrow z \rightarrow \tilde{z} = z^{\frac{n+2}{\tilde{n}+2}} \quad . \quad (2.9)$$

At high densities, however, the Taylor expansion (2.7) is no longer valid and differences in the ordered equilibrium structures will occur.

2.3 Quasi-planar dipolar colloids

In this system, super-paramagnetic colloids are confined to a horizontally oriented cell of variable thickness D . The monodisperse, impenetrable particles interact via a dipole-dipole potential, induced by an external magnetic field, which is applied perpendicular to the cell. Depending on the thickness of the cell, the interaction can either be repulsive, softened repulsive or even attractive at short distances: for very small values of D , i.e. $D \approx \sigma$, the system resembles a two-dimensional

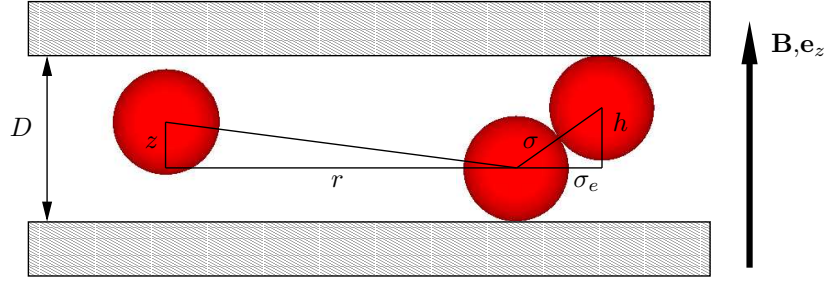


Figure 2.8: *Schematic cross section of the quasi-planar setup discussed in section 2.3. The particles are confined to a cell of thickness $D = \sigma + h$ and interact via a dipole-dipole potential, induced by an external magnetic field $\mathbf{B} = B\mathbf{e}_z$, perpendicular to the x, y -plane.*

setup of dipolar colloids with its characteristic dipole-dipole repulsion. As the cell widens, the particles are allowed to detach from the strictly two-dimensional arrangement at the bottom of the cell and the repulsion starts to soften. In sufficiently wide cells, where the particles can detach sufficiently far from the bottom, the interaction becomes attractive at short distances [9, 10]. This behaviour of the interaction will be discussed in more detail below. Apart from the possibility to investigate these different interaction regimes, the setup enables to study the behaviour of systems at the cross-over from two to three dimensions.

We choose the magnetic field to be perpendicular to the vertical direction z of our setup, so that the cell has infinite extension in x - and y -direction. For convenience, we use the particles' hard-core diameter to express the cell thickness D as $D = \sigma + h$, in order to directly access the the maximal vertical shift h the particles can obtain (see figure 2.8).

As the particles are allowed to detach from the strict two-dimensional setup, we introduce an effective hard-core diameter σ_e , which depends on h :

$$\sigma_e = \sqrt{\sigma^2 - h^2} \quad .$$

With this effective particle diameter, the interaction between two particles separated by an in-plane distance $x = r/\sigma$ and a vertical displacement $\tilde{z} = z/\sigma$, $z \in [0, h]$, can be written as

$$\Phi(x, \tilde{z}) = \begin{cases} \infty & x \leq \sigma_e/\sigma \\ \varepsilon \frac{x^2 - 2\tilde{z}^2}{(x^2 + \tilde{z}^2)^{5/2}} & x > \sigma_e/\sigma \end{cases} \quad . \quad (2.10)$$

The interaction constant ε depends on the magnetic field strength B and the particles' susceptibility χ ,

$$\varepsilon = \frac{\pi\sigma^6\chi^2 B^2}{144\mu_0} \quad .$$

The potential was verified in experiments through a measurement of the in-plane force F_r , acting

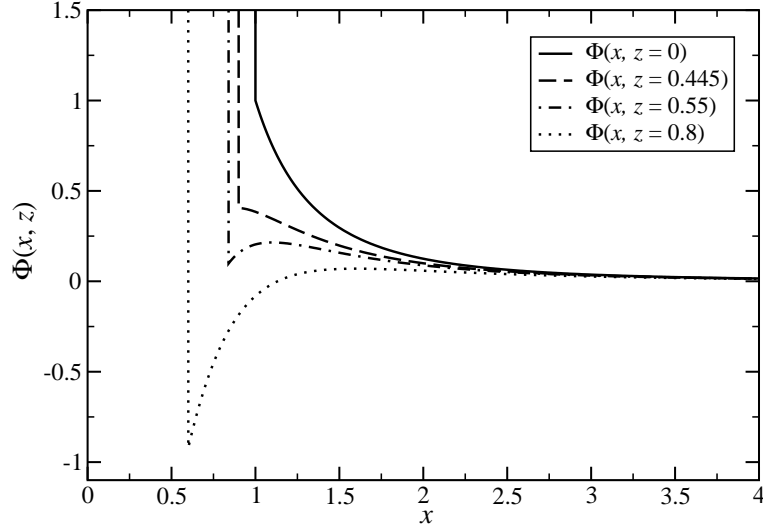


Figure 2.9: Interaction potential $\Phi(r, z)$ between two dipolar colloids at four different vertical displacements: for $z = 0$, the interaction potential resembles the two-dimensional case. The potential for $z = 0.445\sigma$ is close to the crossover to the attractive regime but still purely repulsive whereas for $z = 0.55\sigma$ it exhibits a region of relative attraction. At $z = 0.8\sigma$, the interaction is attractive at short distances.

between two isolated spheres at varying distances [9],

$$F_r(x, \tilde{z}) = \frac{\partial \Phi}{\partial x}(x, \tilde{z}) = -3\epsilon x \frac{4\tilde{z}^2 - x^2}{(x^2 + \tilde{z}^2)^{7/2}} \quad (2.11)$$

As argued above, it is possible to change the characteristic features of the interparticle potential by controlling the maximal vertical shift h . Widening the cell, three regimes can be distinguished: Starting from $h = 0$, at which the two-dimensional behaviour, $\Phi(x, \tilde{z}) \sim 1/x^3$, is recovered, the interaction is purely repulsive. For increasing h , the potential softens until a first "critical" value h_m is reached. For vertical displacements $h > h_m = \sigma/\sqrt{5}$, a regime of relative attraction is reached, where the in-plane force between two touching particles,

$$F_r(x = \sigma_e/\sigma, \tilde{z}) = -3\epsilon \frac{\sigma_e}{\sigma} \left[5(\tilde{z})^2 - 1 \right]$$

is attractive, but the pair potential $\Phi(x, \tilde{z})$ is still positive on contact. Only beyond a second critical vertical displacement $h_c = \sigma/\sqrt{3}$, both, the in-plane force F_r and the interparticle potential $\Phi(x, \tilde{z})$ are negative at small distances, $x \approx \sigma_e/\sigma$, leading us to the attractive regime. At $h = \sigma$, the effective hard-core diameter vanishes, as the particles are able to arrange atop of each other. This formation of "towers" resembles the behaviour of dipolar colloids in three dimensions, where the particles form columns parallel to the applied external field. Figure 2.9 shows pair potentials for all three interaction regimes.

Chapter 3

Statistical mechanics & Thermodynamics

When a system solidifies, it adopts a certain ordered structure, depending on the constraints put on the system. In order to predict these ordered structures, it is necessary to define the characteristic properties which set them apart from all other possible configurations of the system.

In this chapter we introduce the theoretical framework needed to describe the states of a system and formulate the concepts of thermodynamic stability and equilibrium [56–60]. We start by outlining the basic concepts of statistical mechanics that allow us to derive the macroscopic properties of a system from the behaviour of its microscopic constituents, before concentrating on the macroscopic theory of thermodynamics and the description of systems in equilibrium. The end of this chapter is dedicated to the solid state and the calculation of the characterising properties of the stable solid.

3.1 Basic concepts of statistical mechanics

Statistical mechanics derives the macroscopic properties of a system from its microscopic behaviour, employing classical or quantum mechanics and the laws of probability theory to cope with the large number of degrees of freedom. The basis for this deduction is the Hamiltonian \mathcal{H} , that governs the dynamics of the N particles in the system. \mathcal{H} depends on the positions $\mathbf{r}^N = \{\mathbf{r}_1, \mathbf{r}_2, \dots, \mathbf{r}_N\}$ and momenta $\mathbf{p}^N = \{\mathbf{p}_1, \mathbf{p}_2, \dots, \mathbf{p}_N\}$ of the particles,

$$\mathcal{H} = \mathcal{H}(\mathbf{r}^N, \mathbf{p}^N) \quad .$$

The positions \mathbf{r}^N and momenta \mathbf{p}^N span the $6N$ -dimensional phase space of the system, where every microscopic state that the system can take on, is represented by a single point.

In the case of particles obeying the rules of classical mechanics, the Hamiltonian \mathcal{H} leads to

the $6N$ equations of motion,

$$\frac{\partial \mathcal{H}}{\partial \mathbf{r}_i}(\mathbf{r}^N, \mathbf{p}^N) = -\dot{\mathbf{p}}_i \quad , \quad (3.1)$$

and

$$\frac{\partial \mathcal{H}}{\partial \mathbf{p}_i}(\mathbf{r}^N, \mathbf{p}^N) = \dot{\mathbf{r}}_i \quad , \quad (3.2)$$

where the dot denotes a derivative with respect to time t . Solving the equations given in (3.1) and (3.2) yields the trajectory $(\mathbf{r}^N(t), \mathbf{p}^N(t))$ in phase space and thus the evolution of the system in time.

Due to the huge number of constituents in a typical macroscopic system, $N \sim 10^{23}$, which makes an explicit treatment of the equations of motion impossible, we have to resort to a statistical description of the system. To this end, it is convenient to introduce the concept of *ensembles*: a macroscopic state, characterised by certain macroscopic constraints, such as particle number N , volume V , and temperature T , can be realised by a large number of different, but yet equivalent microscopic configurations. The idea of ensembles is to subsume all microscopic configurations that correspond to the same macroscopic state into one set - an *ensemble*.

To extract the value of macroscopic observables from an ensemble, methods of statistics are employed, involving in particular the concept of averaging. We distinguish two different ways to take the average: in an *ensemble average*, the value of a macroscopic property \mathcal{O} is determined as the average over all S microscopic states in the ensemble,

$$\langle \mathcal{O} \rangle_{\text{ens.}}^S = \frac{1}{S} \sum_{i=1}^S \mathcal{O}_i \quad ,$$

with \mathcal{O}_i being the value of the observable obtained from the i -th member of the ensemble. If we introduce $\rho(\mathbf{r}^N, \mathbf{p}^N)$, the probability density for the specific microscopic state characterised by $(\mathbf{r}^N, \mathbf{p}^N)$ to be taken on by the macroscopic system, the ensemble average can be written in its continuous form as

$$\langle \mathcal{O} \rangle_{\text{ens.}} = \frac{1}{Z} \iint d\mathbf{r}^N d\mathbf{p}^N \mathcal{O}(\mathbf{r}^N, \mathbf{p}^N) \rho(\mathbf{r}^N, \mathbf{p}^N) \quad , \quad (3.3)$$

with the partition function Z representing the sum over all states in the ensemble.

In a *time average*, the value of a macroscopic property, that is macroscopically time independent itself, is determined by the evolution of one single microscopic system in the time interval t ,

$$\langle \mathcal{O} \rangle_{\text{time}}^t = \frac{1}{t} \int_0^t dt' \mathcal{O}(\mathbf{r}^N(t'), \mathbf{p}^N(t')) \quad . \quad (3.4)$$

Assuming that the investigated system is *ergodic*, which means that in an infinite amount of time, the system will indeed adopt all microscopic states in an ensemble, the time average and the ensemble average are equivalent:

$$\langle \mathcal{O} \rangle_{\text{time}}^{t \rightarrow \infty} = \langle \mathcal{O} \rangle_{\text{ens.}}^{S \rightarrow \infty} \quad .$$

With this general notions on ensembles and on the deduction of macroscopic quantities of a system from the microscopic behaviour of the constituent particles, we introduce the two specific ensembles important to the investigations carried out in this thesis: the canonical and the isobaric-isothermal ensemble.

3.1.1 The canonical ensemble

The canonical ensemble is used to describe systems of fixed particle number N and volume V , that are in contact with a heat bath. This contact fixes the temperature of the system, whereas the energy is free to fluctuate.

The states that are available to the so called NVT -system in phase space are distributed according to Boltzmann's law,

$$\rho_{\text{can.}}(\mathbf{r}^N, \mathbf{p}^N) \propto e^{-\beta \mathcal{H}(\mathbf{r}^N, \mathbf{p}^N)} \quad , \quad (3.5)$$

where \mathcal{H} is the Hamiltonian and $\beta = 1/(k_B T)$ the inverse temperature of the system, with Boltzmann's constant, $k_B = 1.38065 \text{ J/K}$.

In the case of identical and indistinguishable particles, the partition function of the canonical or NVT -ensemble can be written as

$$Z_{\text{can.}}(N, V, T) = \frac{1}{h^{3N} N!} \iint d\mathbf{r}^N d\mathbf{p}^N e^{-\beta \mathcal{H}(\mathbf{r}^N, \mathbf{p}^N)} \quad , \quad (3.6)$$

where the factor $1/N!$ accounts for the indistinguishability of the particles and $h = 6.626 \cdot 10^{-34} \text{ Js}$ denotes Planck's constant.

All thermodynamic, i.e. macroscopic, properties of the system can be derived from the partition function (3.6). The Helmholtz free energy is connected to it via

$$F(N, V, T) = -k_B T \log Z_{\text{can.}}(N, V, T) \quad , \quad (3.7)$$

and acts as the thermodynamic potential for the NVT -systems (see Section 3.2.1).

3.1.2 The isobaric-isothermal ensemble

If a system is under fixed pressure instead of being of fixed volume, the isobaric-isothermal or NPT -ensemble is used to describe the system. It contains a fixed number of particles N and is in contact with a heat bath, guaranteeing a fixed temperature T . Additionally, it is connected to another reservoir, e.g. through a freely moveable piston, so that the volume V at the disposal of the system adjust to keep the pressure fixed.

The probability density of the isobaric-isothermal ensemble is given by

$$\rho_{\text{iso.}}(\mathbf{r}^N, \mathbf{p}^N) = e^{-\beta P V} e^{-\beta \mathcal{H}(\mathbf{r}^N, \mathbf{p}^N)} \quad , \quad (3.8)$$

so that its partition function is linked to the partition function of the canonical ensemble (3.6) through a Laplace transformation:

$$\begin{aligned} Z_{\text{iso.}}(N, P, T) &= \int dV e^{-\beta PV} Z_{\text{can.}}(N, V, T) = \\ &= \frac{1}{h^{3N} N!} \int dV e^{-\beta PV} \iint d\mathbf{r}^N d\mathbf{p}^N e^{-\beta \mathcal{H}(\mathbf{r}^N, \mathbf{p}^N)} \quad . \end{aligned} \quad (3.9)$$

The appropriate thermodynamic potential for a system of constant N , P and T is the Gibbs free energy, which is related to the partition function (3.9) through

$$G(N, P, T) = -k_B T \log Z_{\text{iso.}}(N, P, T) \quad . \quad (3.10)$$

With equations (3.7) and (3.10), the link between the microscopic behaviour of the NVT - and NPT -ensemble and the systems' macroscopic properties is established.

3.2 Thermodynamics

Thermodynamics is the phenomenological theory used to describe and predict the macroscopic properties of systems in equilibrium. Its laws are expressed in terms of macroscopic quantities only, without any reference to the underlying microscopic structure of the system. The link from the behaviour of the microscopic constituents to the macroscopically observable properties of a system is provided by statistical mechanics, thus acting as the "microscopic foundation" of thermodynamics.

It is convenient to distinguish three different types of thermodynamic systems:

- The isolated system, which does not interact with its surroundings in any form. Energy and the number of particles are therefore fixed quantities.
- The closed system, where particles are neither allowed to escape nor join the system, but interaction with the surroundings in the form of heat exchange is possible.
- The open system, which freely exchanges both, energy and matter, with its surroundings.

All systems considered in this work belong to the class of closed systems.

3.2.1 Thermodynamic potentials

The thermodynamic potential is the central state function of a macroscopic system in equilibrium, as it guarantees the complete knowledge of all the system's thermodynamic properties. It fully describes a system via a function of its respective natural variables. The latter quantities can be divided into two groups: extensive variables like the number of particles N in a system or a system's volume V , which scale with the amount of substance present in the system, and intensive

variables of state like the temperature T or the pressure P , that are independent of the system size.

All thermodynamic potentials are interrelated through Legendre transformations. We here introduce the thermodynamic potential of the isolated system, the *internal energy*

$$U = U(N, V, S) \quad ,$$

as a starting point from which all other potentials are accessible: The natural variables of the internal energy – particle number N , volume V , and entropy S – are all extensive quantities, so that $U(N, V, S)$ itself is a first order homogeneous function,

$$U(\lambda N, \lambda V, \lambda S) = \lambda U(N, V, S) \quad , \quad (3.11)$$

with λ an arbitrary factor. We can therefore expand equation (3.11) in a Taylor-series and write

$$U(N, V, S) = N \left(\frac{\partial U}{\partial N} \right)_{V, S} + V \left(\frac{\partial U}{\partial V} \right)_{N, S} + S \left(\frac{\partial U}{\partial S} \right)_{N, V} \quad . \quad (3.12)$$

As it follows from the first and second law of thermodynamics that

$$TdS = dU + PdV - \mu dN \quad ,$$

equation (3.12) yields Euler's equation,

$$U(N, V, S) = \mu N - PV + TS \quad , \quad (3.13)$$

from which expressions for all other thermodynamic potentials can be derived by exchanging the appropriate independent variables.

Closed systems (NVT)

As stated in section 3.1.1, a closed system is characterised by constant particle number N , constant volume V and constant temperature T , and its corresponding thermodynamic potential is the *Helmholtz free energy*,

$$F = F(N, V, T) \quad .$$

$F(N, V, T)$ is related to the internal energy $U(N, V, S)$ via a Legendre transformation,

$$F(N, V, T) = U[N, V, S(T)] - S(T) \frac{\partial U}{\partial S} = \mu N - PV \quad . \quad (3.14)$$

All thermodynamic properties of a closed system are accessible from the Helmholtz free energy by differentiation of F with respect to its variables N , V and T . For instance the internal energy

U of the system is given by

$$U = \left(\frac{\partial(\beta F)}{\partial \beta} \right)_{N,V} ,$$

the pressure P can be calculated via

$$P = - \left(\frac{\partial F}{\partial V} \right)_{N,T} ,$$

and the chemical potential via

$$\mu = \left(\frac{\partial F}{\partial N} \right)_{P,T} .$$

The second derivatives of the thermodynamic potential with respect to the natural variables correspond to the so-called *response functions*. These thermodynamic properties are most easily accessible to experimental investigations and indicate the physical stability of macroscopic states (see Section 3.2.2). As examples, we here present the heat capacity c_V , which is a measure for the heat needed to raise the temperature of the system by a given amount at constant volume,

$$c_V = \left(\frac{\partial U}{\partial T} \right)_V = -T \left(\frac{\partial^2 F}{\partial T^2} \right)_V ,$$

and the isothermal compressibility κ_T , which determines the change in volume corresponding to a given change in pressure, as

$$\kappa_T^{-1} = -V \left(\frac{\partial P}{\partial V} \right)_T = V \left(\frac{\partial^2 F}{\partial V^2} \right)_T .$$

Closed systems under external pressure (NPT)

The appropriate thermodynamic potential for a system of fixed particle number N , pressure P , and temperature T is the *Gibbs free energy*,

$$G = G(N, P, T) ,$$

which is related to the Helmholtz free energy and thus the internal energy via

$$G(N, P, T) = F[N, V(P), T] - V(P) \frac{\partial F}{\partial V} = U[N, V(P), S(T)] - S(T)T + PV(P), \quad (3.15)$$

yielding

$$G(N, P, T) = \mu N .$$

Again, all properties of the system are contained in this thermodynamic potential and can be calculated via partial derivatives: the internal energy U of the system is given by

$$U = \left(\frac{\partial \beta G}{\partial \beta} \right)_{N,P} ,$$

the volume V by

$$V = \left(\frac{\partial G}{\partial P} \right)_{N,T} ,$$

and the chemical potential μ by

$$\mu = \left(\frac{\partial G}{\partial N} \right)_{T,P} .$$

The response functions are again determined via second derivatives of the thermodynamic potential $G(N, P, T)$: the heat capacity at constant pressure c_P and the isothermal compressibility κ_T are calculated via

$$c_P = -T \left(\frac{\partial^2 G}{\partial T^2} \right)_P ,$$

and

$$\kappa_T = -\frac{1}{V} \left(\frac{\partial^2 G}{\partial P^2} \right)_T .$$

3.2.2 Equilibrium and stability

A macroscopic system is in equilibrium, if its macroscopic properties are independent of time and if the intensive variables of state – temperature T , pressure P , and chemical potential μ – are constant throughout the whole system. Additionally, the equilibrium state of a non-isolated system is characterised by a global minimum of the appropriate thermodynamic potential, as can be derived from the second law of thermodynamics [57].

Following LeChatelier's principle, a system is in a stable equilibrium state, if spontaneous fluctuations in the system induce processes which drive it back to equilibrium and thus counter the initially inducing fluctuations. We can formulate this principle in terms of the response functions:

A system is *thermally stable* if its heat capacity is not negative,

$$c_{V,P} = \left(\frac{\partial U}{\partial T} \right)_{V,P} \geq 0 . \quad (3.16)$$

In this way, it is guaranteed that if some small part of the system spontaneously absorbs more heat than its surroundings, its temperature will increase. Due to the resulting temperature gradient, energy is again dissipated, leading the system back to the equilibrium state.

A *mechanically stable* equilibrium state of a system is reached, if its compressibility is zero or positive,

$$\kappa_{S,T} = -\frac{1}{V} \left(\frac{\partial V}{\partial P} \right)_{S,T} \geq 0 , \quad (3.17)$$

so that, if a small subsystem spontaneously increases in volume, the pressure in this subsystem lowers with respect to its surroundings. The local decrease in pressure not only stops the spontaneous growth of the subsystem, the subsystem is also again compressed, restoring the equilibrium state.

The conditions (3.16) and (3.17) correspond to constraints on the curvature of the thermody-

dynamic potential of the system. In the case of a closed system, the Helmholtz free energy $F(N, V, T)$ of a stable state has to be concave in T and convex in V , as

$$-\left(\frac{\partial^2 F}{\partial T^2}\right)_V = \frac{1}{T}c_V \geq 0 \quad \text{and} \quad \left(\frac{\partial^2 F}{\partial V^2}\right)_T = (V\kappa_T)^{-1} \geq 0 \quad . \quad (3.18)$$

If we are to consider a closed system under constant pressure, the Gibbs free energy $G(N, P, T)$ of a stable equilibrium state is concave in both, T and P , as

$$-\left(\frac{\partial^2 G}{\partial T^2}\right)_P = \frac{1}{T}c_P \geq 0 \quad \text{and} \quad -\left(\frac{\partial^2 G}{\partial P^2}\right)_T = V\kappa_T \geq 0 \quad . \quad (3.19)$$

3.3 The solid state

In this work we investigate the equilibrium structures a two-dimensional system obtains upon freezing. As we choose to determine the system's behaviour at zero temperature, the possible equilibrium structures comprise only ordered monolayers. In order to conduct our investigations, we first have to define the notion of an "ordered solid state" by introducing a suitable description of periodic structures, before discussing how to determine the thermodynamic potential for these structures.

3.3.1 Description of two-dimensional lattices

We describe the ordered solid as an infinite, periodic arrangement of discrete, motionless particles. To this end, the structure is considered to be built of two parts: first, we introduce an underlying periodic array, the *Bravais lattice*. Its so-called *lattice points* are given by linear combinations of two vectors, \mathbf{a} and \mathbf{b} ,

$$\mathbf{A}_{ij} = i\mathbf{a} + j\mathbf{b} \quad , \quad i, j \in \mathbb{Z} \quad . \quad (3.20)$$

The two *primitive vectors*, \mathbf{a} and \mathbf{b} , have to be linearly independent and span the unit cell of the structure, which contains exactly one point of the lattice (see figure 3.1). It is often convenient to subsume the two indices, i and j , that define the linear combination into one index n , that labels the unit cell:

$$\mathbf{A}_{ij} \rightarrow \mathbf{A}_n \quad .$$

Second, we decorate each point \mathbf{A}_n in the lattice with the identical assembly of particles – the so-called *basis* of the lattice. The basis thus describes the arrangement of the particles within a unit cell: If each unit cell is to contain n_p particles, their positions in the unit cell are given by n_p position or *basis vectors* \mathbf{B}_ν , $\nu = 1, \dots, n_p$. We are free to choose the first one \mathbf{B}_1 to be equal to zero, $\mathbf{B}_1 = 0$, so that the origin of the unit cell coincides with the position of the first particle in this cell (see figure 3.1).

With the above definitions, the position of an arbitrary particle in the ordered structure is

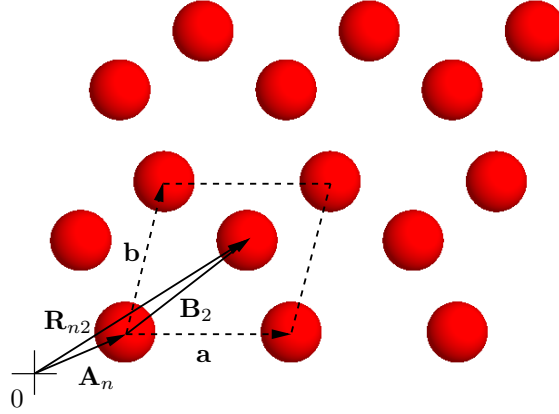


Figure 3.1: Schematic representation of a lattice structure, whose unit cell (broken lines) is spanned by the two primitive vectors \mathbf{a} and \mathbf{b} . The cell contains two particles: one at the chosen origin of the cell and one at the position given by the vector \mathbf{B}_2 . The overall position vector $\mathbf{R}_{n2} = \mathbf{A}_n + \mathbf{B}_2$ is also indicated in the picture.

determined by the vector

$$\mathbf{R}_{n\nu} = \mathbf{A}_n + \mathbf{B}_\nu \quad , \quad (3.21)$$

with $n \in \mathbb{N}$ and $\nu = 1, \dots, n_p$.

At this point we also introduce the concept of *reciprocal lattices* of ordered structures for later use in chapter 5: The reciprocal lattice of a given structure is determined by two reciprocal lattice vectors, \mathbf{c} and \mathbf{d} . These vectors are related to the primitive vectors of the Bravais or *direct lattice*, \mathbf{a} and \mathbf{b} via

$$[\mathbf{cd}]^{-1} = 2\pi[\mathbf{ab}]^T \quad , \quad (3.22)$$

where the two sets of vectors were written as matrices

$$[\mathbf{cd}] = \begin{bmatrix} c_x & d_x \\ c_y & d_y \end{bmatrix} \quad \text{and} \quad [\mathbf{ab}] = \begin{bmatrix} a_x & b_x \\ a_y & b_y \end{bmatrix} \quad ,$$

and $[\dots]^{-1}$ and $[\dots]^T$ indicate the inverse or transposed matrix, respectively.

In analogy to the situation in Bravais lattices (3.20), an arbitrary vector in the reciprocal lattice, \mathbf{Q}_n , can thus be expressed as a linear combination of the two primitive vectors of the reciprocal lattice:

$$\mathbf{Q}_n = i\mathbf{c} + j\mathbf{d} \quad , \quad i, j \in \mathbb{Z} \quad . \quad (3.23)$$

It is important to note that the basis of a structure has no influence on the reciprocal lattice.

Being defined by equations (3.22) and (3.23) the reciprocal lattice represents the set of wave vectors, $\{\mathbf{Q}\}$, that yields plane waves of the same periodicity as the corresponding Bravais lattice

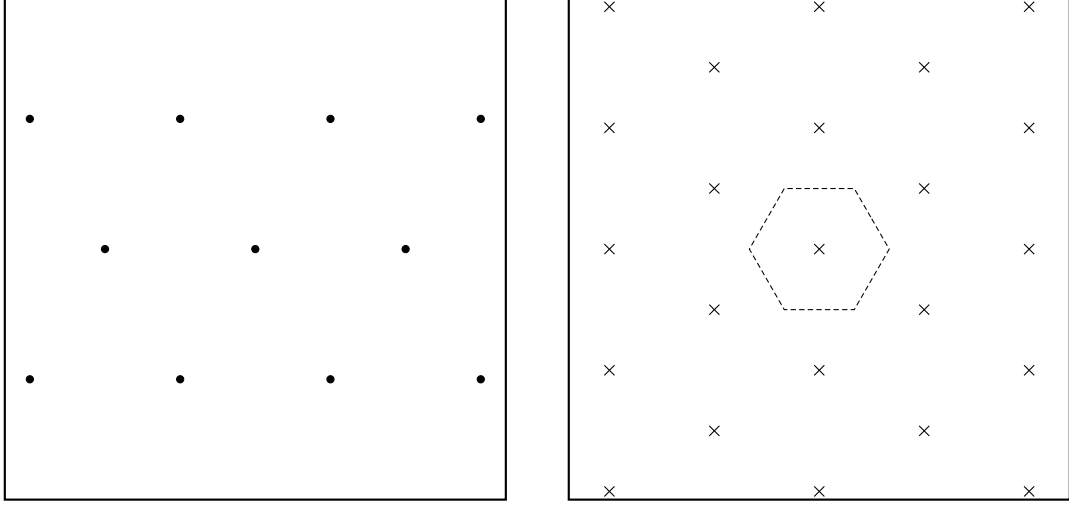


Figure 3.2: A Bravais lattice of sixfold symmetry (left). The corresponding reciprocal lattice with the border of the first Brillouin zone marked by broken lines is given on the right.

[61]:

$$e^{i\mathbf{Q}_n \mathbf{r}} = e^{i\mathbf{Q}_n (\mathbf{r} + \mathbf{A}_n)} \quad \text{or} \quad e^{i\mathbf{Q}_n \mathbf{A}_m} = 1 \quad ,$$

with \mathbf{A}_m a vector in the Bravais lattice of the structure.

As a primitive unit cell – i.e. a volume of space that, if translated by all possible lattice vectors fills space gaplessly and completely – we choose to introduce the *first Brillouin zone* of the reciprocal lattice: it is given by the region in \mathbf{Q} -space, that is closer to one \mathbf{Q} -point than to any other (see figure 3.2). It thus reflects the symmetry of the corresponding lattice and is used to determine distinct solutions to the equations of motion in the harmonic approximation of lattice dynamics (see chapter 5).

3.3.2 Lattice sums

In order to investigate the ordered equilibrium structure of a system under given constraints like fixed particle number N , volume V , and temperature T , we have to determine the corresponding thermodynamic potential. As the influence of the entropy of the structure is irrelevant due to the chosen constraint $T = 0$, the expressions (3.14) and (3.15) for the Helmholtz and Gibbs free energy simplify to

$$F(N, V, T = 0) = U(N, V) \quad \text{and} \quad G(N, P, T = 0) = U[N, V(P)] + PV(P) \quad . \quad (3.24)$$

We therefore first focus on the calculation of the internal energy of an ordered structure in the following. For a general ordered structure, the internal energy per particle at zero temperature

is given by the sum over the pair interactions between all particles contained in this structure. With $\Phi(r)$ being the interaction potential between two particles at distance r , and $\{\mathbf{R}_{n\nu}\}$ the set of possible lattice sites, we can write for the internal energy per particle

$$\frac{U}{N} = \frac{1}{2} \sum'_{\{\mathbf{R}_{n\nu}\}} \Phi(R_{n\nu}) \quad , \quad (3.25)$$

where the sum in (3.25) has to be suitably taken to avoid self-interactions [31].

One component systems

For a known two-dimensional structure whose unit cell is spanned by the two vectors \mathbf{a} and \mathbf{b} and contains only one single particle, equation (3.25) can be written as

$$\frac{U}{N} = \frac{1}{2} \sum'_{i,j} \Phi(i\mathbf{a} + j\mathbf{b}) \quad . \quad (3.26)$$

The sum in (3.26) runs over all values of $i, j \in \mathbb{Z}$, except the term for $i = j = 0$, which is omitted in order to avoid self-interactions. This omission of the $(0, 0)$ -term is denoted by a prime in equation (3.26).

For lattices with more than one particle in the unit cell, equation (3.26) reads as

$$\frac{U}{N} = \frac{1}{2} \sum'_{i,j} \Phi(i\mathbf{a} + j\mathbf{b}) + \frac{1}{n_p} \sum_{i,j} \sum_{k>m} \Phi(i\mathbf{a} + j\mathbf{b} + \mathbf{B}_k - \mathbf{B}_m) \quad , \quad (3.27)$$

where \mathbf{B}_i denotes the position vector of the i -th particle in the unit cell and n_p is the total number of particles present in the cell. It is important to note that the first summation in the second term of equation (3.27) runs over all possible values $i, j \in \mathbb{Z}$, whereas in the sum of the first contribution the $(0, 0)$ -term, which corresponds to a self-interaction of the particle located in the origin of the chosen coordinate system, is omitted again.

Binary mixtures

If the lattice we consider does not consist of only one species but rather of two different sorts of particles, additional changes to equation (3.27) are necessary: let n_A be the number of particles per unit cell that belong to species A and n_B the number of particles of species B . The total number of particles in the cell is thus given by $n_p = n_A + n_B$. We choose to label the particles of species A as the "first" particles in the cell, so that particle p_i is of sort A if $i \leq n_A$ and of sort B , if $n_A < i \leq n_p$, (see figure 3.3).

As the interaction between different particle species varies, we distinguish between three cases: $\Phi_{AA}(r)$, the interaction between two particles of species A at a distance r , $\Phi_{BB}(r)$, the interaction between two particles of species B , and $\Phi_{AB}(r)$, the interspecies interaction. The internal energy

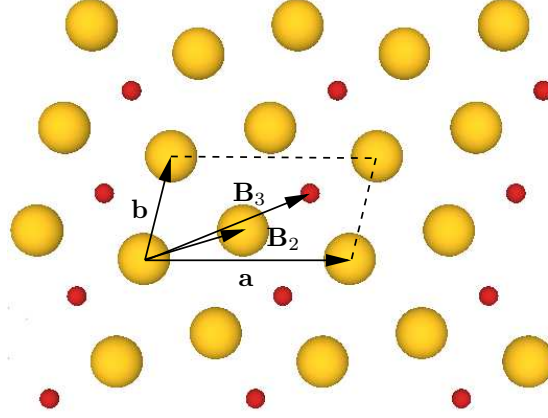


Figure 3.3: *Example for an ordered structure of a binary mixture. The origin of the unit cell is chosen to coincide with the position of the first particle in the cell, p_1 , so that $B_1 = (0, 0)$.*

per particle for a binary mixture can thus be written as [62]

$$\begin{aligned} \frac{U}{N} = \frac{1}{n_p} & \left[\frac{n_A}{2} \sum'_{i,j} \Phi_{AA}(i\mathbf{a} + j\mathbf{b}) + \frac{n_B}{2} \sum'_{i,j} \Phi_{BB}(i\mathbf{a} + j\mathbf{b}) + \right. \\ & \left. \sum_{ij} \sum_{k=1}^{n_p-1} \sum_{m=k+1}^{n_p} \Phi_{\epsilon(k)\epsilon(m)}(i\mathbf{a} + j\mathbf{b} + \mathbf{B}_k - \mathbf{B}_m) \right] . \end{aligned} \quad (3.28)$$

$\Phi_{\epsilon(k)\epsilon(m)}(r)$ stands for the appropriate interaction potential, depending on the involved particle species, $\epsilon(i) = A$ for $i \leq n_A$ and $\epsilon(i) = B$ for $n_A < i \leq n_p$.

Chapter 4

Theoretical Tools I: Genetic algorithms

Genetic Algorithms (abbreviated "GAs", "GA" in singular) are widely applicable optimisation techniques, invented in the late 1960ies, early 1970ies by John Holland [26]. They were developed with the information-theoretical aspects of natural evolution in mind and closely resemble biological processes: Information is stored by encoding it in sequences of "genes" and is propagated from step to step using operations like recombination, mating and mutation. The iterative search process is guided by a principle resembling Darwin's "survival of the fittest". The main feature of a GA is its inherent ability to simultaneously explore large areas of the search space, but to concentrate its numerical efforts on promising regions at the same time. It is this *global scope* that leads to the GA's efficiency in finding global extrema in rough and high-dimensional search spaces.

The first applications of GAs ranged from biology – modelling the development of cells [63,64] – to computer science, namely designing artificial intelligence [65] and controlling image recognition [66]. In the meantime, GAs have taken over many different fields, including business administration, economics, game theory, logistics, circuit design and, of course, physics.

4.1 General principles

One of the main characteristics of a GA is the way in which information is stored: Every solution to the problem at hand is translated to a sequence of genes, usually a binary vector. Thus, every solution has two representations: a *phenotype*, the "physical appearance" like the actual values of a set of parameters, and a *genotype*, which comprises all hereditary information, i.e. the exact sequence of genes. In the context of GAs, a possible solution is also often called an *individual*, meaning both, the pheno- and the genotype specific to this solution. The GA acts solely on the "genetic" level, i.e. the genotype, to find the optimal solution.

0. Find suitable *encoding* of the individuals.
1. Initialise a random starting population ("generation $\mathcal{G}(0)$ ").
2. *Evaluate* every single individual in the current generation, using a fitness function.
3. *Select* individuals for reproduction.
4. *Recombine* selected "parent" individuals to create offspring.
5. *Mutate* the offspring.
6. *Replace* individuals of the current generation by offspring, thus creating a new generation.
7. Check termination condition and either terminate the algorithm or cycle through steps 2. - 7. once more.

Table 4.1: *Pseudo-code of a generic genetic algorithm*

There exist many different versions of GAs nowadays, all adapted and trimmed to best solve one special set of problems. The general work-flow of GAs is nonetheless easily explained as it normally remains unchanged in all varieties (see table 4.1 for a summary): Before to start the GA, an encoding suitable to the parameters of the problem at hand has to be found. The GA is then initialised with a number of randomly generated individuals, the starting *generation* $\mathcal{G}(0)$. In the next step, each individual in $\mathcal{G}(0)$ is evaluated by assigning a fitness value: the better an individual is suited to solve the problem, the higher its assigned fitness. After this evaluation of the current generation, *parents* are selected for reproduction. The selection process is governed by the fitness, so that fitter individuals have a higher probability to reproduce. The information stored in the selected parent individuals is then recombined and new individuals are created. The offspring is mutated and replaces individuals of the current population according to the chosen replacement scheme and a new generation $\mathcal{G}(1)$ is formed. In the last step, the termination condition – usually a maximal number of generations to be created – is checked and the algorithm is either aborted or the cycle of evaluation, selection, recombination, mutation, and replacement is iterated once more. The different versions of GAs vary in how the structures emphasised in table 4.1 are implemented. We will therefore explain them in more detail, including the implementations used to carry out the investigations described in Chapter 6:

Encoding

In the encoding step, a mapping from pheno- to genotype and vice versa has to be found. Every solution is encoded in a string of genes x_i , usually called a *chromosome*, $c = \langle x_1, \dots, x_l \rangle$. The l genes in the chromosome can take on values out of a given alphabet $\mathcal{M} = \{m_1, \dots, m_n\}$. The most commonly used alphabets are:

- Binary alphabet

The possible values a gene can take on are $\mathcal{M}_{binary} = \{0, 1\}$. This encoding allows for efficient use of computational time, as memory access is compact and most programming languages support operations directly on the binary level. Its main drawback lies with the fact that the encoding in binary is highly dependent on the positioning of bits: The binary

decimal	binary	gray code
0	0000	0000
1	0001	0001
2	0010	0011
3	0011	0010
4	0100	0110
5	0101	0111
6	0110	0101
7	0111	0100
8	1000	1100

Table 4.2: *The first nine decimal numbers (left) in their binary (middle) and gray code representation (right).*

representations of two "adjacent" decimal numbers n and $n + 1$ mostly differ in more than one bit, so that small changes in one encoding (e.g. decimal) does not necessarily result in a small change in the binary code. For an example, consider the numbers "3" and "4". A value of "4" is given by the sequence "100" whereas "3" is encoded as "011", a sequence in which all significant bits are different. Additionally the different positions in a binary number are not of equal importance. Leading digits in a binary number correspond to higher powers of two by definition, so that a change in one of the leading genes of a chromosome can yield a drastic change in the encoded parameter value. These effects can cause severe problems in the recombination or mutation of individuals and have to be taken into account by choosing an appropriate mating and/or mutation routine (see below).

- Gray code

Gray code was developed to overcome one of the drawbacks of binary code stated above. It uses the same alphabet, $\mathcal{M}_{\text{gray}} = \{0, 1\}$, to encode decimal numbers, but the translation follows different rules: Instead of splitting each decimal number in powers of two, they are encoded such that the gray code representation of two neighbouring decimal numbers differs always only in one bit. For examples, see table 4.2, where the decimal numbers 0 to 8 are encoded using both schemes.

Besides the chosen alphabet, also the way in which the information is arranged on the chromosome has major influence on the performance of the search algorithm. In general, contentually related information should be stored close together on the chromosome and segments essential to an individual's ability to solve the given problem are to be encoded as compact as possible, so that they are not easily destroyed in mutation or reproduction processes [67]. When encoding in binary, one possible way of paying respect to these two rules is to order the genes on the chromosome not by parameter, but by their corresponding power of two: Each decimal parameter is encoded in its binary representation and those bits of each parameter, that correspond to the same power of two, are stored next to each other on the chromosome. Figure 4.1 depicts a schematic example of such an "importance arrangement".

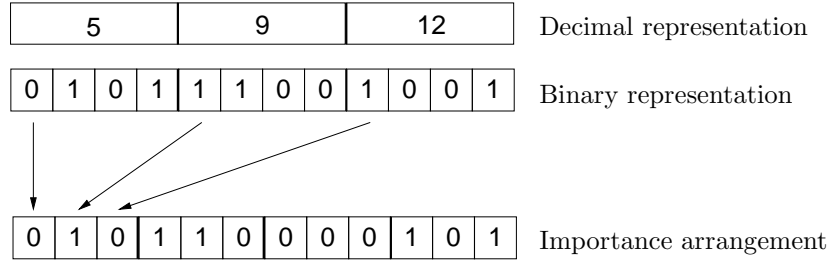


Figure 4.1: A schematic representation of an "importance arrangement". Bits corresponding to the same power of two in the binary representation of every parameter are stored next to each other.

The main disadvantage of a genetic algorithm has its origin in the encoding process. Due to the finite number of genes available, a GA is not converging to the exact global extremum. Additional refining mechanisms are needed to reach the solution that corresponds to the global extremum exactly.

Evaluation

In the evaluation step, the "quality" of every individual is assessed and a value is assigned to each individual, measuring its ability to approximate the optimal solution. According to this value, the probability of an individual to be selected for reproduction is determined. Strictly speaking, there thus exist two different quantities: a *rating* and a *fitness* value; the first expresses the quality of an individual and the latter determines an individual's chance to partake in the reproduction process and pass on its genes. Since the fitness is given as a function of – or can even be set equal to – the rating, the two terms are often used synonymously. There are no constraints on both functions, although continuous functions are best suited to achieve efficient convergence, since small changes in the rating and/or fitness thus correspond to small changes in the chromosomes. The actual form of the rating and fitness function depends strongly on the specific problem as they in general contain the function to optimise (see Subsection 4.2.2).

Selection

The selection process determines which individuals are used to produce the offspring forming the next generation. It is governed by the fitness of the individuals in a sense that individuals with a high fitness have a higher probability to reproduce and the offspring of "fit" parents are over-proportionally frequent in the newly generated populations. In this way, the average fitness can increase from generation to generation.

The two different selection schemes used in our surveys are

- Roulette selection

In this routine, the selection probability $p_{\text{select}}(\mathcal{I}_i)$ of individual \mathcal{I}_i is directly correlated to the individuals fitness:

$$p_{\text{select}}(\mathcal{I}_i) = \frac{f(\mathcal{I}_i)}{\sum_{j=1}^N f(\mathcal{I}_j)} \quad ,$$

with $f(\mathcal{I}_i)$ being the fitness of the i -th individual \mathcal{I}_i and $\sum_{j=1}^N f(\mathcal{I}_j)$ the total fitness of the population. Strategies how to implement this scheme efficiently can be found in [67].

- Linear ranking

Individuals are ordered according to their fitness and a fixed reproduction probability is assigned to each individual, depending on their rank in this sequence. No direct correlation exists between the fitness of an individual and the probability to be selected for reproduction.

Recombination

The recombination procedure – or ”cross-over mechanism”, as it is often called following biological nomenclature – governs in which fashion information is passed on from one generation to the next. It determines how new individuals – also called *offspring* or *children* – are created from the selected parent individuals. It thus defines the way in which the search space is sampled and has to be adapted to both, the specific problem, as well as the chosen encoding to ensure an efficient performance of the GA. A suitable recombination mechanism allows to reach regions with an above-average ranking fast and then to keep to such regions by preserving sequences of genes that lead to especially fit individuals. Common examples of cross-over mechanisms are

- One-point cross-over

Two selected parent chromosomes are cut at the same, randomly chosen point and genetic information is interchanged to form the chromosomes of two new individuals (see figure 4.2, top).

- Two-point cross-over

In this case, both chosen parent chromosomes are cut at two arbitrary positions before the cross-over of genetic material takes place to create new individuals (see figure 4.2, bottom).

- Random cross-over

The random cross-over routine represents a generalisation of the n -point cross-over. It employs a random assembly vector \mathcal{A} to determine the genes a child inherits from each parent. At the beginning of a recombination step, \mathcal{A} , which is of the same length as the chromosomes, is filled with an arbitrary sequence of genes. The first child \mathcal{C}_0 is constructed gene by gene from the parent chromosomes \mathcal{P}_0 and \mathcal{P}_1 following the ”rules” posed by the assembly vector: at every position of a 0 (1) in the assembly vector, the gene is inherited from parent \mathcal{P}_0 (\mathcal{P}_1). If using binary or gray code, the second child \mathcal{C}_1 is generated from child \mathcal{C}_0 via a simple bit-inversion. For a schematic representation of a random cross-over of two binary or gray coded chromosomes, see figure 4.3, bottom. Of the examples given, this cross-over routine allows for the highest mobility in search space, although the random ”jumbling” of genetic material hinders the development of stable, high-quality gene-sequences.

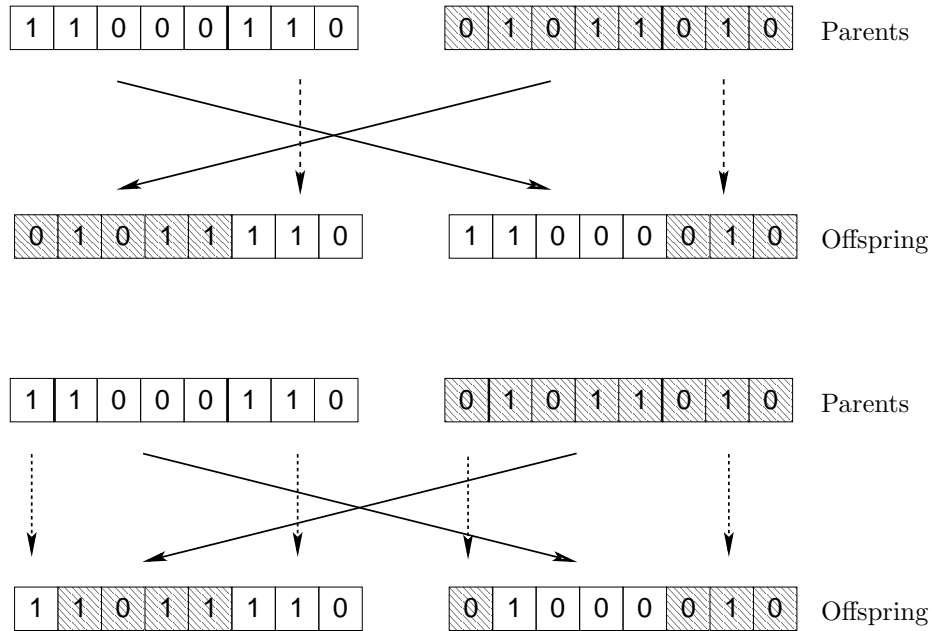


Figure 4.2: Schematic representations of a one-point cross-over (top) and a two-point cross-over (bottom) of two binary or gray coded chromosomes. The two cutting positions are marked by thick lines in both cases.

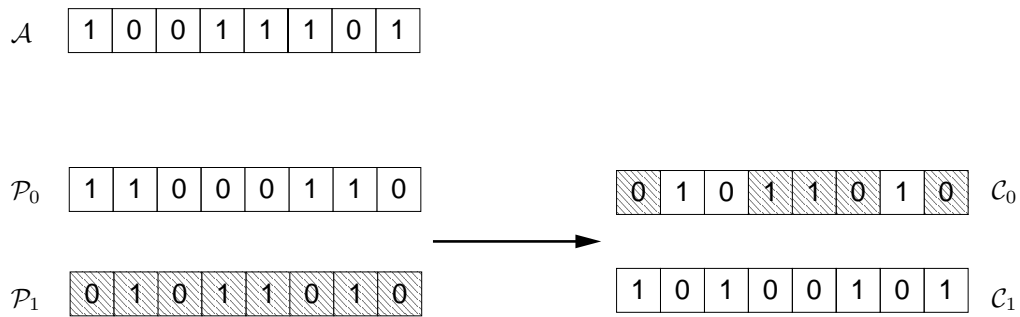


Figure 4.3: Schematic representation of a random cross-over of two binary or gray coded chromosomes. Genes are passed on from the parent chromosomes \mathcal{P} to the children \mathcal{C} according to the bits of an assembly vector \mathcal{A} . The second child \mathcal{C}_1 is given by a simple bit-inversion of child \mathcal{C}_0 .

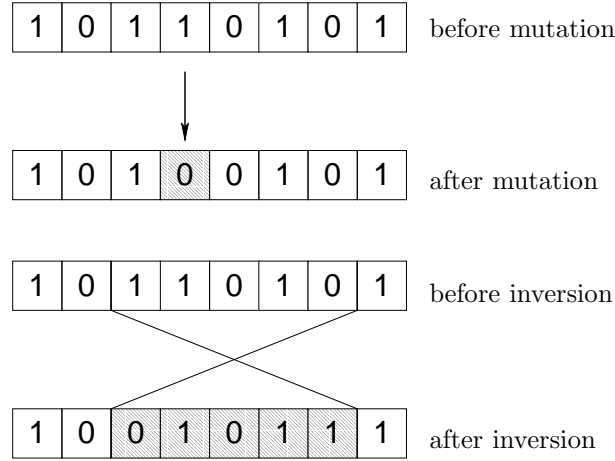


Figure 4.4: *Schematic representation of a general mutation step (top) and of an inversion (bottom) in a binary or gray coded chromosome.*

Mutation

In a mutation step, genes are changed at random to a different value of the chosen encoding alphabet \mathcal{M} . Every gene has a certain probability p_{mutate} to mutate, typically ranging from $p_{\text{mutate}} = 0.001 - 0.01$. Its function is to reintroduce lost genetic material and thus to avoid inbreeding. It is also essential to the GA's ability to escape local extrema as it averts premature convergence to a local minimum. For an example of a general mutation step, see figure 4.4, top. Common mutation routines contain:

- Uniform mutation

Every gene in the chromosome has the same probability to be mutated. Normally, p_{mutate} is a fixed, external parameter, although there do exist GAs that use a uniform mutation where the probability changes with increasing number of generations produced.

- Position-dependent mutation

Position-dependent mutation is a variation of the uniform mutation. Instead of one probability value p_{mutate} for all genes, every gene x_i in the chromosome is assigned an individual mutation probability $p_{\text{mutate}}(x_i)$. It is often employed together with binary encoding, as it allows to pay respect to the varying importance of digits in a binary number.

- Inversion

This procedure mimics a mutation process known from natural biological evolution, namely the inversion of whole sequences of genes on a chromosome. An inversion procedure is given by the following rules: first, choose two arbitrary genes x_i and x_j with $i \leq j$ on the chromosome. Then invert the sequence between x_i and x_j so that

$$x_{i+n}^{\text{new}} = x_{j-n}^{\text{old}} \quad , \quad \forall n \leq j - i \quad .$$

For a schematic representation of an inversion on a binary or gray coded chromosome, see figure 4.4, bottom.

Replacement

The replacement scheme determines which individuals form a new generation $\mathcal{G}(n+1)$. The possible candidates to choose from are the individuals of the generation $\mathcal{G}(n)$, their mutated and their unmutated offspring. The various schemes differ in the number of individuals they accept from each of these three populations and the criteria used for choosing them.

- **Generational replacement**

Generational replacement is the most simple replacement scheme possible. All individuals of generation $\mathcal{G}(n)$ are replaced by their mutated offspring to form generation $\mathcal{G}(n+1)$. Because the whole population is replaced disregarding the respective quality of the individuals, both, maximum and average rating can decrease from one generation to the next, slowing down convergence. Despite this drawback, generational replacement is widely used as it helps to avoid premature convergence due to a too homogeneous gene pool. It makes it impossible for a small number of fit individuals to dominate populations from an early stage on.

- **Elitism**

Elitism tries to overcome the disadvantages of generational replacement by including the best m individuals of generation $\mathcal{G}(n)$ in the next generation $\mathcal{G}(n+1)$. The maximum rating in the population is thus guaranteed to monotonically increase. The number of best individuals to pass on unchanged from one generation to the next is usually small ($m \approx 1$). Problems occurring because of lacking diversity in the gene pool are of course enhanced by elitism.

Additional information on the general concepts of GAs can be found in [26, 31, 67].

4.2 Genetic algorithms and solidification

When investigating the phase behaviour of a given system, we are confronted with the task of determining its equilibrium states for varying values of the different thermodynamic quantities. Concepts based on statistical mechanics like liquid state theories [22], density functional theory [20] and computer simulations [68] provide reliable information on a system's thermodynamic properties for a broad range of state points. To explore the whole phase diagram, it is also necessary to determine the ordered configurations a system adopts on freezing. The conventional approach to this task relies heavily on the experience and intuition of the investigator: A set of candidate structures is selected, the thermodynamic potential corresponding to each structure is calculated via suitable methods and the candidate with the lowest value of the thermodynamic potential is taken to be the stable equilibrium configuration at the specific state point. Especially for systems that tend to show a broad variety of complex structures, this procedure, based on

a biased preselection of configurations, is bound to fail as it is extremely likely that relevant structures are not included in the preselected set and are therefore missing in the phase diagram. Another approach of using computer simulations, namely a simulated annealing technique [69,70], is time-consuming and runs the risk of getting trapped in local minima due to the rough and complex search space of the problem. Additionally, computer simulations most often require some input concerning the expected structure – e.g. to determine the shape of the simulation box – to work efficiently. Thus, also simulation techniques are often biased in their search for an ordered equilibrium structure.

Knowing about this drawback of conventional methods, GAs were introduced as an alternative, independent approach to the problem of finding ordered equilibrium structures in condensed matter [27–29,71]. They are particularly suited to deal with rough, complex and/or high-dimensional search spaces, making them less time consuming than most computer simulations. However, the more relevant feature of a GA-based search strategy is, that it allows for an *unbiased* search for the optimal ordered structure, as crystal lattices can be parametrised and encoded in a very general way (see Subsection 4.2.1). The only constraint posed on the search stems from the limited number of parameters a GA can optimise efficiently. Using a GA thus minimises the risk of overlooking suitable structures.

Dieter Gottwald introduced a GA-based search strategy able to predict ordered equilibrium structures for systems of fixed particle density, requiring only the particle interactions as sole input [30,31]. Remarkable results for three-dimensional soft systems like ionic microgels [34,35], amphiphilic dendrimers [13,72,73], and star polymers [30] were obtained: Not only was it possible to correct established phase diagrams, the genetic algorithm was also able to find highly asymmetric, open structures to be stable equilibrium structures. In order to investigate hard-core particles in three dimensions, the algorithm was adapted by Gernot Pauschenwein and tested on a three-dimensional square-shoulder system [74,75].

When the same search strategy was to be employed for two-dimensional systems for the present work, a number of changes became necessary to ensure the algorithm’s capacity to reliably find the global minimum representing the equilibrium lattice structure: The parametrisation of two-dimensional lattices presented in [31] was refined and adapted to the special geometries of the systems to investigate. Furthermore, the algorithm was adapted to deal with systems of constant pressure. In the following, all extensions are described in detail, starting with the parametrisations of the various (quasi-) two-dimensional lattices in the following subsection.

4.2.1 Parametrisation of lattice structures

The various parameterisations presented in this chapter are all based on the general description of two-dimensional lattices proposed in [31]. To facilitate discussion, we therefore repeat this ”standard” description of two-dimensional lattices at this point.

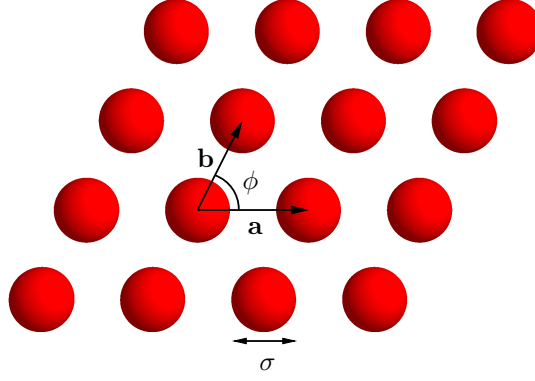


Figure 4.5: *Example of a general two-dimensional lattice with the two lattice vectors \mathbf{a} and \mathbf{b} spanning the unit cell. The angle between the lattice vectors ϕ , acting as a parameter in the chosen description, and the length scale σ are also depicted.*

4.2.1.1 One-component systems

A general, two-dimensional lattice can be described by two lattice vectors \mathbf{a} and \mathbf{b} and n_p vectors \mathbf{B}_i ($i = 1, \dots, n_p$) that determine the positions of the particles in the unit cell, as described in section 3.3.

The two lattice vectors can be parametrised as

$$\mathbf{a} = a \begin{pmatrix} 1 \\ 0 \end{pmatrix}, \quad \mathbf{b} = ax \begin{pmatrix} \cos \phi \\ \sin \phi \end{pmatrix}, \quad (4.1)$$

with

$$\frac{a}{\sigma} = \left(\frac{n_p}{\eta \sigma^2 x \sin \phi} \right)$$

fixing the overall size of the lattice, σ being a problem-specific length scale, usually the particle diameter (see figure 4.5), and η the particle area density. The two parameters used are the length ratios of the two lattice vectors,

$$x = \frac{|\mathbf{b}|}{|\mathbf{a}|},$$

and the angle ϕ between the primitive vectors \mathbf{a} and \mathbf{b} (see figure 4.5).

The position vector of the first particle in the unit cell can be set to

$$\mathbf{B}_1 = \begin{pmatrix} 0 \\ 0 \end{pmatrix}$$

without loss of generality. The vectors of the remaining $n_p - 1$ particles in the cell are given as linear combinations of the two lattice vectors \mathbf{a} and \mathbf{b} ,

$$\mathbf{B}_i = \alpha_i \mathbf{a} + \beta_i \mathbf{b}, \quad i = 2, \dots, n_p.$$

In this way, the unit cell of a general, two-dimensional lattice is described by the $n_q = 2 + 2(n_p - 1)$ parameters $x, \phi, \alpha_1, \beta_1, \dots, \alpha_{n_p}, \beta_{n_p}$. Requiring \mathbf{a} to be the longer of the two vectors spanning the unit cell and all n_p particles to lie inside the cell spanned by \mathbf{a} and \mathbf{b} leads to the following constraints

$$0 < x \leq 1 \quad , \quad 0 < \phi \leq \frac{\pi}{2} \quad (4.2)$$

$$0 \leq \alpha_i < 1 \quad , \quad 0 \leq \beta_i < 1 \quad \text{with } i = 1, \dots, n_p \quad . \quad (4.3)$$

To facilitate encoding, the real valued parameters are translated to integer numbers, using the scheme described in [31]:

$$\begin{aligned} x &= \frac{m_x + 1}{2^{l_n}}, \\ \phi &= \frac{\pi}{2} \frac{m_\phi + 1}{2^{l_a}}, \\ \alpha_i &= \frac{m_{\alpha_i}}{2^{l_n}}, \\ \beta_i &= \frac{m_{\beta_i}}{2^{l_n}} \quad . \end{aligned}$$

The integers $m_x, m_\phi, m_{\alpha_i}$ and m_{β_i} are then converted to binary or gray code (see Section 4.1) before they are encoded and stored in a chromosome. Depending on whether the quantity is an angle or not, l_n or l_a bits are used for encoding the corresponding integer. This encoding scheme is used, independent of the chosen parametrisation of lattices.

Since the choice of lattice vectors is not unique, different individuals may translate to the same lattice structure, thus diminishing the variety in a population and reducing the performance of the algorithm significantly. To guarantee an efficient search algorithm, a mechanism has to be included which reduces the number of parameter sets that translate to the same lattice and which allows for an unambiguous mapping between geno- and phenotype. A way to achieve this unambiguity is the strategy described in [31], where each set of lattice vectors found by the algorithm is modified such that the circumference of the described unit cell reaches a minimum, thus minimising the existing ambiguities. The utilised transformations of vector sets are

$$(\mathbf{a}, \mathbf{b}) \rightarrow (\mathbf{a} \pm \mathbf{b}, \mathbf{b}) \quad (4.4)$$

$$(\mathbf{a}, \mathbf{b}) \rightarrow (\mathbf{a}, \mathbf{b} \pm \mathbf{a}) \quad . \quad (4.5)$$

Instead of employing an iteration of transformations of the form (4.4) and (4.5) as described in [31], it is also possible to reduce the search space of the algorithm *a priori* so that it only contains unambiguous configurations. As explained in appendix A, the constraint on the parameters x and ϕ that correspond to the usage of a unit cell of minimal circumference can be written as

$$2 \cos \phi \leq x \quad , \quad (4.6)$$

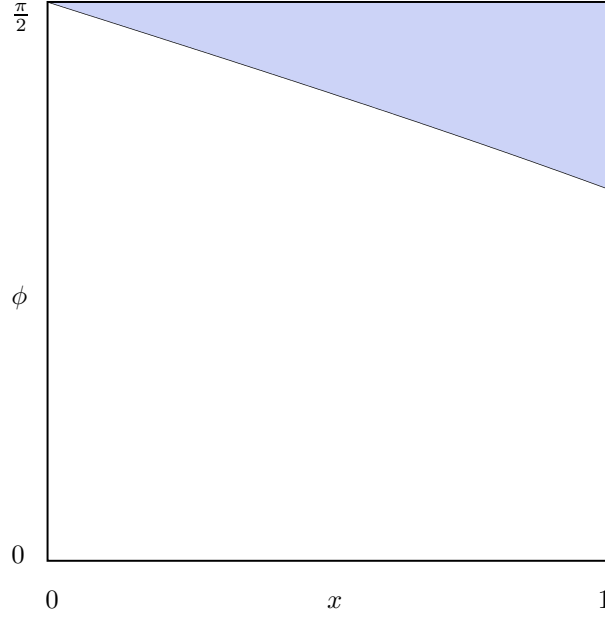


Figure 4.6: *Reduced search space due to unambiguous lattice parametrisation. The region of (x, ϕ) -pairs corresponding to unit cells with minimal circumference is coloured blue.*

leading to a reduction of the search space as depicted in figure 4.6.

To implement the constraint posed by (4.6), the domains of the parameters change from (4.2) and (4.3) to

$$0 < x \leq 1 \quad , \quad \arccos\left(\frac{x}{2}\right) \leq \phi \leq \frac{\pi}{2} \quad (4.7)$$

$$0 \leq \alpha_i < 1 \quad , \quad 0 \leq \beta_i < 1 \quad , \quad (4.8)$$

with $i = 1, \dots, n_p$.

4.2.1.2 Systems with constant pressure

For calculations in the NPT-ensemble, i.e., if the external pressure P on the system is fixed instead of the particle number density η , the latter enters as an additional parameter to be optimised. It is encoded in the chromosome via the quantity σ/a , which correlates to the number density as

$$\eta = \frac{n_p}{\sigma^2 x \sin \phi} \left(\frac{\sigma}{a}\right)^2 \quad , \quad (4.9)$$

with σ/a in the range

$$0 \leq \frac{\sigma}{a} \leq 1 \quad . \quad (4.10)$$

4.2.1.3 Hard-core systems

If the particles in a system interact via a potential of the form

$$\Phi(r) = \begin{cases} \infty & \forall r \leq \sigma \\ \tilde{\Phi}(r) & \text{else} \end{cases}, \quad (4.11)$$

i.e. if the particles are impenetrable hard spheres, the system is not allowed to take on configurations containing overlapping particles. The basic parametrisation of two-dimensional lattices as described above does not exclude such "forbidden" configurations *a priori*. Due to the highly stochastic character of GAs, our search algorithm is likely to produce large numbers of useless, forbidden (or "illegal") individuals, slowing down convergence, if not preventing it completely.

There exist two conceptually different strategies to guarantee the efficiency of the algorithm in this case: first, by excluding all illegal structures from search space by finding a suitable parametrisation of the lattice, and second, by enabling the GA to distinguish between different degrees of overlap, so that the undesired configurations are gradually ruled out in the evolutionary process. A combination of both approaches has been opted for in this work: For the primitive lattice – i.e. concerning the parameters x and ϕ – the additional constraints due to hard-core exclusion are taken into account *a priori*. Restraining the cores of the particles from overlapping is equivalent to demanding all possible vectors \mathbf{x} in the lattice to be larger than the particle diameter σ ,

$$|\mathbf{x}| = |\chi\mathbf{a} + \xi\mathbf{b}| \geq \sigma, \quad \forall \chi, \xi \in \mathbb{Z}. \quad (4.12)$$

Translating the conditions given in (4.12) to constraints on the parameters x and ϕ leads to the porous search space of allowed configurations depicted in red in figure 4.7. If we combine these conditions with (4.6), that was introduced to reduce the ambiguity of the parametrisation, we see that most of the constraints posed in (4.12) are superfluous. The only constraint, that remains relevant as a consequence of relation (4.12), is the one corresponding to the curve that connects the points $(x, \phi) = (0, 0)$ and $(1, \pi/2)$ in figure 4.7,

$$|b| \geq \sigma. \quad (4.13)$$

This constraint can be written in terms of x and ϕ as

$$x \geq \frac{\eta\sigma^2 \sin \phi}{n_p},$$

leading to the following domains of the two parameters

$$\frac{\pi}{3} \leq \phi \leq \min \left[\arcsin \left(\frac{n_p}{\eta\sigma^2} \right), \frac{\pi}{2} \right], \quad (4.14)$$

$$\max \left(2 \cos \phi, \frac{\eta\sigma^2 \sin \phi}{n_p} \right) \leq x \leq 1, \quad (4.15)$$

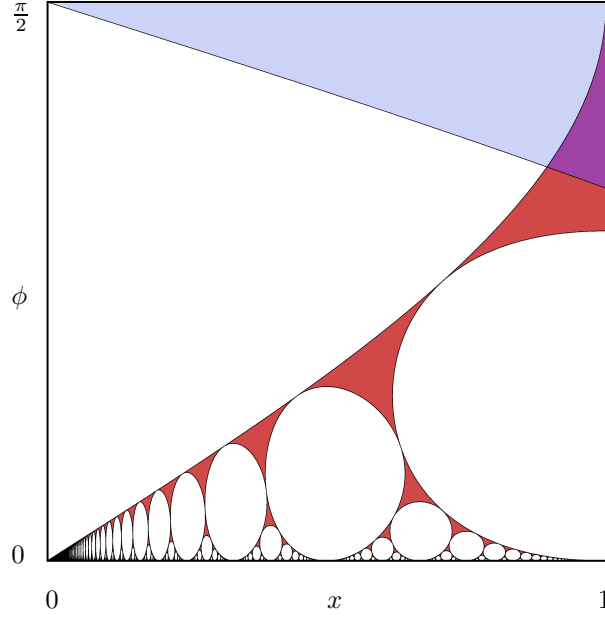


Figure 4.7: *Reduced search space including constraints due to the unambiguity of the lattice parametrisation (blue) and the hard core conditions (red) for $\eta\sigma^2 = 1.0$. The remaining legal search space is coloured violet.*

as x and ϕ can no longer be chosen independently. The reduced search space that results from this intersection of the two conditions (4.6) and (4.13) is coloured violet in figure 4.7.

For the parameters α_i and β_i , which fix the positions of additional particles in the unit cell, the hard-core condition was not implemented directly in our parametrisation. Instead, the hard-core in the interaction potential (see equation (4.11)) was softened to a linear ramp

$$\Phi(r) = \Phi_0(2 - \frac{r}{\sigma}) \quad \forall r \leq \sigma$$

with Φ_0 being a sufficiently large constant, typically $\Phi_0 \sim \mathcal{O}(10^3)$. Thus, configurations in which particles overlap only slightly are rated higher than those structures with large overlaps, and inept structures can be ruled out step by step in the evolutionary cycle of the GA. For two-dimensional lattices with a maximum of eight particles per unit cell, this workaround approach to hard-core systems has proven to be efficient and a full implementation of the hard-core exclusion was refrained from.

4.2.1.4 Cluster-biased lattices

For one-component systems that are known to exhibit clustering, the standard parametrisation of Section 4.2.1.1 was altered in the following way: We interpret the clustered lattice as a standard two-dimensional lattice whose n_s lattice sites are not occupied by single particles, but by regular dimers or triangular trimers. Thus, the parametrisation described in 4.2.1.1 can be utilised for

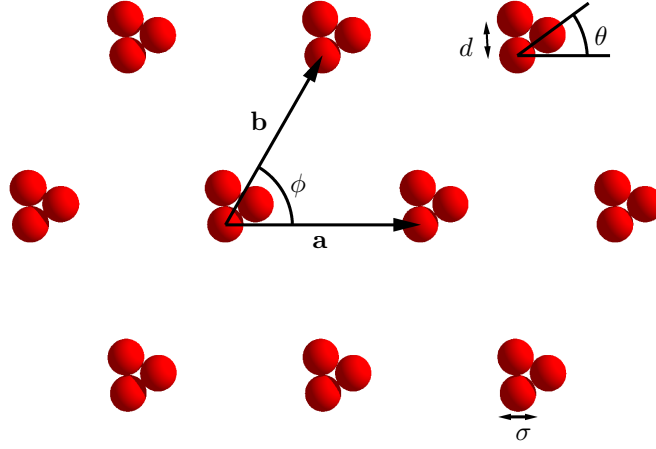


Figure 4.8: *Example of a clustered lattice, in which each cluster contains three particles. The additional parameters d , the separation of particles in the cluster and θ , the tilting angle of the cluster are indicated in the figure.*

the underlying structure, but additional parameters are introduced to determine the shape and respective orientation of the clusters: a tilting angle θ_i of the cluster at site i , $i = 1, \dots, n_s$ in the unit cell and the separation of particles in the cluster d (see figure 4.8).

As only clustered lattices are of interest, the interparticle distance d is not allowed to take on the largest distance in the unit cell, i.e. $|\mathbf{a} + \mathbf{b}|$, but is limited to the length of the smaller lattice vector \mathbf{b} . In the case of soft particles, the additional parameters of cluster-biased lattices read

$$0 \leq d < xa \quad , \quad 0 \leq \theta_j \leq \pi \quad , \quad (4.16)$$

with $j = 1, \dots, n_s$.

If hard-core particles are to be considered, these domains change to

$$\sigma < d < xa - \sigma \quad , \quad 0 \leq \theta_j \leq \pi \quad . \quad (4.17)$$

The main advantage of the cluster-biased parameterisation is that it allows to describe unit cells with $n_p \geq 2$ with a smaller number of parameters as the standard parametrisation of two-dimensional lattices given in Section 4.2.1.1: In the case of the standard description, $2n_p$ parameters are necessary to fix the positions of n_p particles in the unit cell. Using the cluster-biased parametrisation with dimers at the n_s sites of the unit cell, we need $2n_s$ parameters to determine the underlying two-dimensional lattice and $n_s + 1$ to describe the dimers. Since the total number of particles in the cell is twice the number of available sites, $n_p = 2n_s$, $3n_p/2 + 1$ parameters are used to describe a lattice with n_p particles per unit cell. Therefore, the cluster-biased description and the standard parametrisation need the same number of parameters to describe the lattice if $n_p = 2$, namely $2 \cdot 2 = 4$. In the case of $n_p > 2$, the cluster-biased parametrisation manages to

standard parametrisation:	$2n_p$,	$\forall n_p \in \mathbb{N}$
cluster-biased (dimers):	$\frac{3}{2}n_p + 1$,	$\forall n_p \in \{2, 4, 6, \dots\}$
cluster-biased (trimers):	$n_p + 1$,	$\forall n_p \in \{3, 6, 9, \dots\}$

Table 4.3: *Comparison of the numbers of parameters necessary to describe a lattice with n_p particles in the unit cell, using the standard parametrisation introduced in Section 4.2.1.1 and the two versions of the cluster-biased description.*

describe the lattice with fewer parameters.

If the sites in the cell are populated by triangular trimers instead of dimers, this advantage gets even more pronounced. We again need $2n_s + (n_s + 1)$ parameters for the whole lattice, which in the case of trimers, contains $n_p = 3n_s$ particles in the unit cell. We therefore need only $n_p + 1$ parameters, to describe a lattice with n_p particles per cell (see table 4.3 for a summary).

4.2.1.5 Binary mixtures

In a binary mixture, two different particle species, A and B , populate the sites of an ordered equilibrium structure. A binary mixture is characterised by the concentration C of one of the two species, e.g. $C = n_B/(n_A + n_B)$. Since a unit cell of an ordered structure can only contain an integer number of each particle species, only non-primitive lattices, i.e. lattices with more than one particle in the unit cell ($n_p \geq 2$) occur in this case. We identify the first n_A particles in the cell to belong to species A and the remaining $n_B = n_p - n_A$ particles to be of species B . No additional parameters are necessary to describe the lattice. The random case, where the different sites in the crystal lattice are not associated with a species but the two sorts of particles are randomly distributed, was not considered.

4.2.1.6 Quasi-planar geometries

In Section 2.3, we introduced a system, in which the particles are allowed to detach from the strict two-dimensional geometry. We choose the two-dimensional lattice to lie in the (x, y) -plane, so that the particles' deviation is perpendicular to the z -axis. To describe this system, we employ the basic parametrisation of two-dimensional lattices, but include n_p additional parameters $z_i \in [0, 1]$, that determine each particle's deviation χ_i from the plane:

$$\chi_i = z_i h \quad , \quad i = 1, \dots, n_p \quad ,$$

with h the maximum deviation possible (see figure 4.9, top).

In the case that the particles exclusively populate the bottom ($\chi_i = 0$) and top positions ($\chi_i = h$), the system can also be described using the parametrisation of layered systems introduced in [31]. In this case, the structure is formed by n_l monolayers, all of which exhibit the same lattice structure and are shifted with respect to each other. The layers are chosen to lie perpendicular

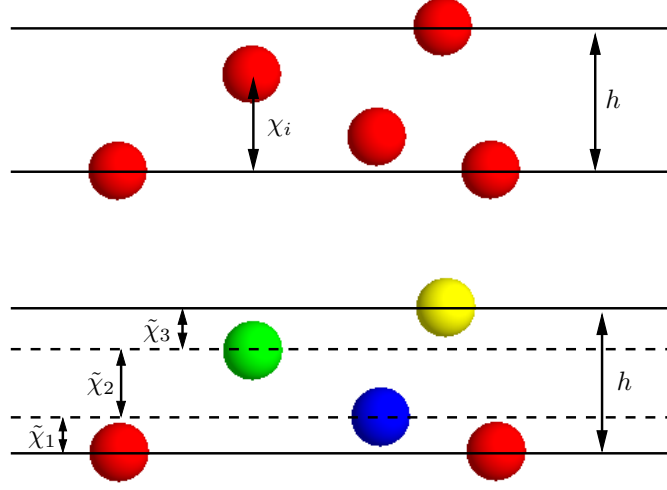


Figure 4.9: Sketches of a quasi-planar lattice (top) and of a lattice structure parametrised using two-dimensional layers (bottom). The planes of the different layers in the bottom picture are marked by straight lines; particles belonging to different layers have different colour.

to the z -axis and are described using the basic parametrisation of two-dimensional lattices. The mutual displacements of the n_l layers are given by $n_l - 1$ interlayer vectors \mathbf{c}_i , connecting the origins of subsequent layers,

$$\mathbf{c}_i = \alpha_i \mathbf{a} + \beta_i \mathbf{b} + \tilde{\chi}_i \begin{pmatrix} 0 \\ 0 \\ 1 \end{pmatrix}, \quad i = 1, \dots, n_l - 1.$$

\mathbf{a} and \mathbf{b} are the lattice vectors of the two-dimensional lattice in each layer and $\tilde{\chi}_i$ is the displacement of the i -th layer from the $(i - 1)$ -th layer in z -direction (see figure 4.9, bottom), so that

$$\sum_{i=1}^{n_l-1} \tilde{\chi}_i = h.$$

Instead of the $\tilde{\chi}_i$, the quantities $z_i \in [0, 1)$, $i = 1, \dots, n_l - 2$ are introduced as parameters to simplify encoding. These z_i are related to the displacements $\tilde{\chi}_i$ via

$$\begin{aligned} \tilde{\chi}_i &= z_i \left(h - \sum_{j=1}^{i-1} \tilde{\chi}_j \right), \quad i = 1, \dots, n_l - 2 \quad \text{and} \\ \tilde{\chi}_{n_l-1} &= h - \sum_{j=1}^{n_l-2} \tilde{\chi}_j. \end{aligned}$$

To compare the two parametrisations presented in this section for efficiency, we again determine the number of parameters used in both descriptions. In the first case, $3n_p$ parameters describe the positions of n_p particles in the unit cell: $2n_p$ from the standard description fixing the position of the particles in the plane and n_p parameters for the position in z -direction. In the case of a layered

lattice, the total number of parameters is $2n_{2D} + 2(n_l - 1) + n_l - 2$: $2n_{2D}$ are needed to describe the two-dimensional lattice structures of the layers, $2(n_l - 1)$ determine the components of the interlayer vectors in the x, y -plane and $n_l - 2$ parameters fix the components of these vectors in the z -direction. The layer-parametrisation can therefore describe a unit cell containing $n_p = n_{2D}n_l$ particles with only $2n_{2D} + 3n_l - 4$ parameters, making it the more efficient description.

4.2.2 The fitness function

We employ a fitness function similar to the one proposed in [31] to evaluate the individuals. In the case of a fixed particle number density η , the fitness of individual \mathcal{I} is given by

$$f(\mathcal{I}) = \exp\left(1 - \frac{\tilde{F}(\mathcal{I})}{\tilde{F}_0}\right) . \quad (4.18)$$

$\tilde{F}(\mathcal{I})$ stands for the the free energy per particle of the lattice structure represented by individual \mathcal{I} and \tilde{F}_0 is the free energy per particle of a suitable chosen reference structure, usually a hexagonal lattice of the same particle density. At zero temperature, the free energy is simply given by the lattice sum of the crystal, as the entropic contribution to the free energy vanishes (see section 3.3.2).

If calculations are conducted in an NPT -ensemble, i.e., for fixed pressure P , the Gibbs free energy $G(N, P, T)$ acts as a thermodynamic potential, and the equilibrium structure is characterised by a minimum in $G(N, P, T)$. At $T = 0$, the Gibbs free energy reduces to $G = U + P/\eta$, with η the particle number density of the crystal and U its lattice sum (see section 3.3.2). The form of the fitness function remains unchanged,

$$f(\mathcal{I}) = \exp\left(1 - \frac{\tilde{G}(\mathcal{I})}{\tilde{G}_0}\right) . \quad (4.19)$$

$\tilde{G}(\mathcal{I})$ and \tilde{G}_0 are the Gibbs free energies per particle of individual \mathcal{I} and of the reference structure, respectively.

Chapter 5

Theoretical Tools II: Phonon band structures

Besides the static equilibrium configurations, we are interested in the dynamic properties of the investigated systems, as the motion of the particles in the ordered structure accounts for a number of effects and properties, e. g. the thermal conductivity of a material, its elastic properties, and its melting behaviour. Also the propagation of sound through the solid is closely connected to the dynamics of the system.

In this chapter, we summarise the tools necessary to study the dynamics of an ordered solid structure, focusing on the calculation of the dispersion relation, or *phonon band structure*, for a given two-dimensional system. We start with the framework of the classical theory of harmonic crystals, presenting the formalism that leads to the dispersion relation [61,76,77], before discussing the changes necessary to describe colloidal crystals [78–80].

5.1 Basic concepts of harmonic lattice dynamics

In order to investigate the dynamics of a given system, we have to consider finite temperature, as the description of solid structures as given in section 3.3 cannot account for various of a materials properties. Although the equilibrium structures are identified for zero temperature in this thesis, we can assume that at sufficiently low temperature, $T \sim 0$, these configurations will prevail as stable equilibrium structures and we can determine their dynamics.

We have chosen to investigate the dynamics of our systems within the theory of harmonic crystals, which is based on two assumptions:

1. the movement of the particles in the ordered structure is given by oscillations around their respective lattice sites, which are identified as the average position of the particles in the structure.

2. the deviation of a particle from its mean position shall be small compared to the average spacing between neighbouring sites in the lattice.

With these two assumptions, the Hamiltonian of the system, which governs the dynamics of all constituent particles, can be simplified to the harmonic approximation of lattice dynamics and every motion possible to the particles in the lattice can be described as a superposition of a small set of harmonic oscillations – the so-called *normal modes* of the system.

5.1.1 The harmonic approximation

The Hamiltonian of a system of N particles is given by the sum of kinetic and potential energies:

$$\mathcal{H}(\mathbf{r}^N, \mathbf{p}^N) = \sum_{n,\nu} \frac{\mathbf{p}_{n\nu}^2}{2M_\nu} + V(\mathbf{r}^N) \quad , \quad (5.1)$$

where $\mathbf{p}_{n\nu}$ is the momentum of the ν -th particle in the n -th unit cell of the lattice structure. The index ν thus runs from 1 to n_p , the total number of particles in one unit cell (see section 3.3). We will also introduce an index i to distinguish the three Cartesian components of vector-valued quantities in the following.

If the interactions between particles are described by the radially symmetric pair potential $\Phi(r)$, the potential energy $V(\mathbf{r}^N)$ is represented by the interactions between all particles in the lattice,

$$V(\mathbf{r}^N) = \frac{1}{2} \sum_{n\nu} \sum_{n'\nu'} \Phi(|\mathbf{r}_{n\nu} - \mathbf{r}_{n'\nu'}|) \quad . \quad (5.2)$$

As the particles are allowed to oscillate around their associated lattice site, the actual position of a particle $\mathbf{r}_{n\nu}$ (see figure 5.1), can be written as

$$\mathbf{r}_{n\nu} = \mathbf{R}_{n\nu} + \mathbf{u}_{n\nu} \quad , \quad (5.3)$$

so that the deviation from the lattice site at $\mathbf{R}_{n\nu}$ is given by the vector $\mathbf{u}_{n\nu}$. With (5.3), equation (5.2) becomes

$$V(\mathbf{r}^N) = \frac{1}{2} \sum_{n\nu} \sum_{n'\nu'} \Phi(|\mathbf{R}_{n\nu} - \mathbf{R}_{n'\nu'} + \mathbf{u}_{n\nu} - \mathbf{u}_{n'\nu'}|) \quad . \quad (5.4)$$

According to our second assumption – the deflection $\mathbf{u}_{n\nu}$ is small for all particles – the potential energy (5.4) can be expanded following Taylor's theorem:

$$V(\mathbf{r}^N) = V_0 + \sum_{n\nu i} k_{n\nu i} u_{n\nu i} + \frac{1}{2} \sum_{n\nu i} \sum_{n'\nu' i'} k_{n\nu i, n'\nu' i'} u_{n\nu i} u_{n'\nu' i'} + \mathcal{O}(\mathbf{u}^3) \quad , \quad (5.5)$$

with

$$V_0 = \frac{1}{2} \sum_{n\nu} \sum_{n'\nu'} \Phi(|\mathbf{R}_{n\nu} - \mathbf{R}_{n'\nu'}|)$$

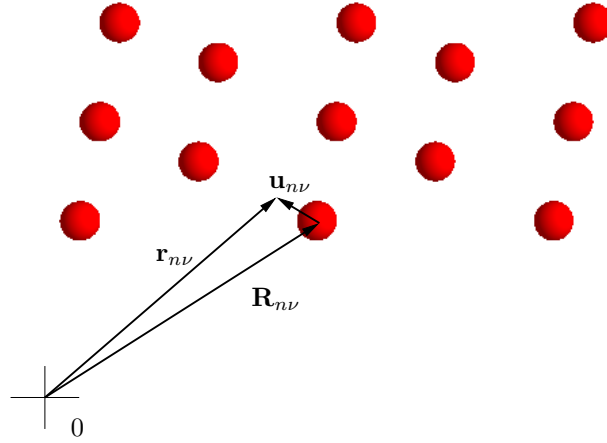


Figure 5.1: Schematic representation of a two-dimensional lattice with the average position of a particle in this lattice given by $\mathbf{R}_{n\nu}$, the displacement $\mathbf{u}_{n\nu}$ and the resulting, actual position $\mathbf{r}_{n\nu}$.

being the potential energy of the equilibrium structure at rest, and the *coupling parameters*

$$k_{n\nu i} = \left. \frac{\partial V(\mathbf{r}^N)}{\partial u_{n\nu i}} \right|_{\mathbf{u}=0}, \quad (5.6)$$

$$k_{n\nu i, n'\nu' i'} = \left. \frac{\partial^2 V(\mathbf{r}^N)}{\partial u_{n\nu i} \partial u_{n'\nu' i'}} \right|_{\mathbf{u}=0}. \quad (5.7)$$

The parameters $k_{n\nu i}$ corresponds to individual Cartesian components i of the force exerted on the particle labeled $n\nu$ by all other particles at their respective equilibrium positions. Since there is by definition no net force acting on the particles in equilibrium, the coupling parameters $k_{n\nu i}$ have to vanish for all values of n , ν , and i ,

$$k_{n\nu i} = 0 \quad , \quad \forall \quad n, \nu, i \quad .$$

Taking the translational invariance of the lattice and its symmetric properties into account, one of the indices n or n' is superfluous in the $k_{n\nu i, n'\nu' i'}$: the properties of the lattice have to be left unchanged if the whole lattice is shifted, e.g. by a lattice vector $\mathbf{R}_{n''}$,

$$k_{n\nu i, n'\nu' i'} = k_{n+n''\nu i, n'+n''\nu' i'} \quad .$$

If we choose $n'' = -n'$, we see that $k_{n\nu i, n'\nu' i'}$ is only dependent on the difference $n - n'$,

$$k_{n\nu i, n'\nu' i'} = k_{n-n'\nu i, 0\nu' i'} \quad , \quad (5.8)$$

reflecting the translational invariance of the lattice structure. Following the definition of the $k_{n\nu i, n'\nu' i'}$ in equation (5.7), we can express the coupling parameters in terms of the pair potential

$\Phi(r)$:

$$k_{n\nu i, n'\nu' i'} = \frac{r_i r_{i'}}{r^2} \left[\frac{1}{r} \frac{\partial \Phi(r)}{\partial r} - \frac{\partial^2 \Phi(r)}{\partial r^2} \right] - \frac{1}{r} \delta_{ii'} \frac{\partial \Phi(r)}{\partial r} \quad , \quad (5.9)$$

with

$$r_i = R_{n\nu i} - R_{n'\nu' i} \quad \text{and} \quad r_{i'} = R_{n\nu i'} - R_{n'\nu' i'} \quad .$$

For sufficiently small deviations \mathbf{u} , the anharmonic terms $\mathcal{O}(\mathbf{u}^3)$ can be neglected in the expansion of the potential energy in (5.5), and we arrive at the harmonic approximation for the Hamiltonian:

$$\mathcal{H}(\mathbf{r}^N, \mathbf{p}^N) = \sum_{n,\nu} \frac{\mathbf{p}_{n\nu}^2}{2M_\nu} + V_0 + V_{\text{harm}}(\mathbf{r}^N)$$

with

$$V_{\text{harm}}(\mathbf{r}^N) = \frac{1}{2} \sum_{n\nu i} \sum_{n'\nu' i'} k_{n\nu i, n'\nu' i'} u_{n\nu i} u_{n'\nu' i'} \quad . \quad (5.10)$$

5.1.2 Normal modes and dispersion relations

Within the classic theory of harmonic lattices, the motion of every particle in a structure can be described by a superposition of a small set of "elementary waves" or normal modes characteristic to the system. To determine the normal modes of a given lattice consisting of n_p particles in the unit cell and determined by the lattice vectors $\{\mathbf{R}_{n\nu}\}$, we start with the harmonic approximation of the system's Hamiltonian,

$$\mathcal{H}(\mathbf{u}^N, \mathbf{p}^N) = \sum_{n\nu i} \frac{p_{n\nu i}^2}{2M_\nu} + V_0 + \frac{1}{2} \sum_{n\nu i} \sum_{n'\nu' i'} k_{n\nu i, n'\nu' i'} u_{n\nu i} u_{n'\nu' i'} \quad . \quad (5.11)$$

By introducing the canonic variables

$$\pi_{n\nu i} = \frac{p_{n\nu i}}{\sqrt{M_\nu}} \quad \text{and} \quad s_{n\nu i} = u_{n\nu i} \sqrt{M_\nu}$$

we can rewrite equation (5.11) as

$$\mathcal{H}(\mathbf{s}^N, \boldsymbol{\pi}^N) = \sum_{n\nu i} \frac{\pi_{n\nu i}^2}{2} + V_0 + \frac{1}{2} \sum_{n\nu i} \sum_{n'\nu' i'} D_{n\nu i, n'\nu' i'} s_{n\nu i} s_{n'\nu' i'} \quad , \quad (5.12)$$

where we identify

$$D_{n\nu i, n'\nu' i'} = \frac{k_{n\nu i, n'\nu' i'}}{\sqrt{M_\nu M_{\nu'}}} \quad (5.13)$$

as the dynamical matrix of our system.

Hamilton's equations of motion (see chapter 3) lead to $3N$ partial differential equations to describe the movement of the N particles in the system,

$$\frac{\partial^2 s_{n\nu i}(t)}{\partial t^2} = - \sum_{n'\nu' i'} D_{n\nu i, n'\nu' i'} s_{n'\nu' i'}(t) \quad , \quad (5.14)$$

where the time-dependence of $s_{n\nu i}$, $s_{n'\nu' i'}$ is now explicitly marked. We solve these equations by using an ansatz of the form of simple plane waves – the normal modes:

$$\mathbf{s}_{n\nu}(t) = \mathbf{c}_\nu e^{i\mathbf{q}\mathbf{R}_n - i\omega t} \quad , \quad (5.15)$$

where $\mathbf{c}_\nu = \mathbf{c}_\nu(\mathbf{q})$ is the polarisation vector and $\omega = \omega(\mathbf{q})$ is the frequency of the normal mode, both yet undetermined, and \mathbf{q} is the wave vector of the plane wave.

Inserting relation (5.15) in equation (5.14) yields

$$\omega^2 c_{\nu i} e^{i\mathbf{q}\mathbf{R}_n} = \sum_{n'\nu' i'} c_{\nu' i'} D_{n\nu i, n'\nu' i'} e^{i\mathbf{q}\mathbf{R}_{n'}} \quad . \quad (5.16)$$

Due to the definition of the dynamical matrix in equation (5.13), $D_{n\nu i, n'\nu' i'}$ has to share the symmetry properties of the coupling parameter $k_{n\nu i, n'\nu' i'}$:

$$D_{n\nu i, n'\nu' i'} = D_{n-n'\nu i, 0\nu' i'}$$

in analogy to equation (5.8). We can therefore define the Fourier-transform of the dynamical matrix,

$$\tilde{D}_{\nu i, \nu' i'}(\mathbf{q}) = \sum_{n'} D_{n\nu i, n'\nu' i'} e^{-i\mathbf{q}(\mathbf{R}_n - \mathbf{R}_{n'})} \quad , \quad (5.17)$$

which is independent of the index n and allows us to write the equations of motion from equation (5.16) as

$$\omega^2 c_{\nu i} = \sum_{\nu' i'} \tilde{D}_{\nu i, \nu' i'}(\mathbf{q}) c_{\nu' i'} \quad . \quad (5.18)$$

In this way, we retrieve $2n_p$ relations, from which the frequencies $\omega(\mathbf{q})$ and polarisation vectors $\mathbf{c}_\nu(\mathbf{q})$ of the normal modes can be extracted as the eigenvalues and eigenvectors of the Fourier-transformed dynamical matrix.

From equation (5.17) we see that the Fourier-transform of the dynamic matrix is periodic in \mathbf{q} -space:

$$\tilde{D}_{\nu i, \nu' i'}(\mathbf{q} + \mathbf{Q}_n) = \tilde{D}_{\nu i, \nu' i'}(\mathbf{q}) \quad ,$$

where \mathbf{Q}_n is a vector of the reciprocal lattice. The eigenvalues $\omega(\mathbf{q})$ and the eigenvectors $\mathbf{c}_\nu(\mathbf{q})$ are fully determined by the Fourier-transform of the dynamical matrix and share its periodicity,

$$\omega(\mathbf{q} + \mathbf{Q}_n) = \omega(\mathbf{q}) \quad \text{and} \quad \mathbf{c}_\nu(\mathbf{q} + \mathbf{Q}_n) = \mathbf{c}_\nu(\mathbf{q}) \quad .$$

As the first Brillouin zone is a smallest repeat unit of the reciprocal lattice and reflects its symmetry, it is sufficient to determine the dispersion relations $\omega(\mathbf{q})$ and the polarisation vectors $\mathbf{c}_\nu(\mathbf{q})$ only for wave vectors inside the first Brillouin zone in order to define both, $\omega(\mathbf{q})$ and $\mathbf{c}_\nu(\mathbf{q})$,

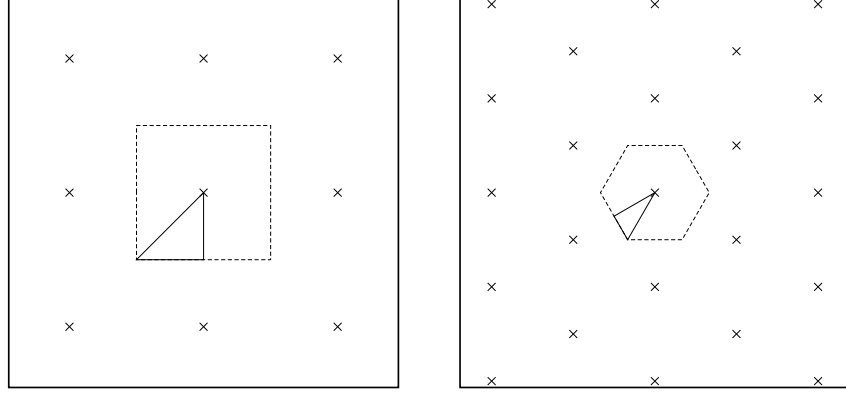


Figure 5.2: *Reciprocal lattice of a square Bravais lattice (left) and of a hexagonal Bravais lattice (right). The first Brillouin zone is marked by broken lines in both cases, the full line encloses the irreducible section of the respective zone (see text).*

in the entire reciprocal space. In addition, we can define a so-called “*irreducible section*” within the first Brillouin zone, which represents the smallest repeat unit of the Brillouin zone itself (see figure 5.2). The border of this irreducible section usually links the points of high symmetry and runs along the symmetry lines present in the Brillouin zone [77]. By convention, phonon band structures are presented for paths along this border.

The $2n_p$ curves for $\omega(\mathbf{q})$ forming the phonon band structure of the given lattice can belong to two fundamentally different sorts of branches (see figure 5.3 for an example): There always exist two *acoustic branches*, where the frequencies vanish in the limit of long wave lengths $|\mathbf{q}| \rightarrow 0$, and which correspond to a collective movement of all particles in the lattice. If the considered structure contains more than one particle in the unit cell, i.e. if $n_p > 1$, the remaining $2n_p - 2$ branches are so-called *optical branches*, which are characterised by a finite frequency at $|\mathbf{q}| = 0$. In an oscillation corresponding to an optical branch of the phonon band structure, the particles in the unit cell are deflected such that the centre of mass of the unit cell remains fixed.

5.2 On the lattice dynamics of colloidal crystals

Although colloidal dispersions often act as suitable model systems for conventional, “atomic” materials, the lattice dynamics of a solid colloidal dispersion crucially differs from the respective behaviour of an atomic system. The main reason for these differences lies in the special setup of a colloidal dispersion: a colloidal solid – or *colloidal crystal* as it is also called – consists of macroscopic particles forming a periodic structure while suspended in a microscopic solvent. Contrary to the classic atomic theory of harmonic crystals, the dynamics of a colloidal crystal is not fully determined by the particle interactions and the form of the lattice structure, but the influence of the solvent on the particles’ motion has to be taken into account as well.

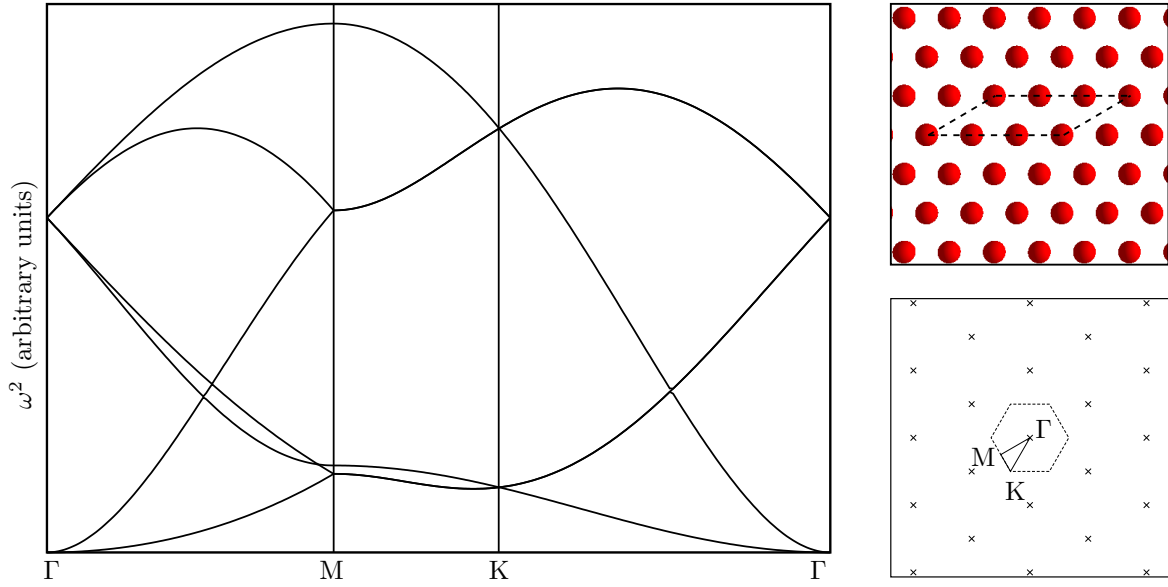


Figure 5.3: *The phonon band structure of a hexagonal lattice with three particles per unit cell (left), interacting via an ideal dipole-dipole potential. The corresponding structure is shown on the top, right; the chosen unit cell is marked by a broken line. The reciprocal lattice of the structure is shown on the bottom right, with the first Brillouin zone (broken line) and the irreducible path along which the band structure was calculated (full line). The points of special symmetry are also marked (Γ , M, and K).*

The presence of the solvent has various effects: it introduces friction, and thus a damping of the lattice vibrations, and it allows for an exchange of momenta between particles, leading to hydrodynamic forces. There exist various models to describe and derive the dynamical behaviour of colloidal crystals, which consider the influence of the solvent to various extent, e.g. simple models treating the colloidal dispersion as a spring-bead-lattice immersed in a viscous medium [79], descriptions including Stokes friction to the standard treatment known from solid state theory [80, 81], or theoretical approaches that treat both influences on the particles motion, friction and hydrodynamic forces [78, 82, 83].

By employing these models, it can be shown that due to these additional forces acting on the particles in the colloidal solid, no modes travelling through the colloidal crystal can exist. The typical lattice vibrations are strongly damped, as the ratio of the frequencies of the normal modes $\omega(\mathbf{q})$ over the also wave-vector dependent friction factors [78], $\Lambda(\mathbf{q})$, is usually very small,

$$\frac{\omega(\mathbf{q})}{\Lambda(\mathbf{q})} \sim 10^{-3} - 10^{-4} \quad .$$

The travelling phonon modes of the classical, harmonic crystal are thus transformed into normal *relaxation modes* [78, 79, 84–87], and an arbitrary movement of the particles in a colloidal crystal is described as a superposition of these relaxation modes.

In our investigations on the dynamics of solid colloidal systems, we focus on the calculation of the phonon band structure. The dispersion curves $\omega(\mathbf{q})$ are still fully determined by the interparticle potential and the lattice structure, so that despite all the changes necessary in the description of the dynamics of colloidal crystal, the phonon band structures retain their role as an important source of information on the system's properties.

In experiments, there exist various techniques to determine the phonon band structure of a colloidal crystal. Most of these approaches depend on an accurate model of the particles' movement [78, 88, 89], as the dispersion relations are deduced from the decay rate of the autocorrelation function of the normal modes. There are some techniques though, that circumvent the complex problem of modelling the different influences on the particle dynamics through the extensive use of video microscopy: instead of recording dynamical data, the dispersion curves are directly accessed via the measurement of spatial correlations [80, 87, 90], rendering the complex problem of modelling the influences of the solvent on the colloidal particles superfluous.

Chapter 6

Results

6.1 Square-shoulder systems

The two-dimensional square-shoulder system presented in section 2.1 has been investigated in the past by various different methods [12, 15, 25, 32, 33]. In these studies, a remarkably rich variety of stable ordered configurations was discovered, where the particles were found to arrange in often highly asymmetric structures, despite the radially symmetric interaction potential (see section 2.1, equation (2.1)).

Knowing about the deficiencies in identifying complex particle configurations of the conventional search algorithms that have been employed in these previous works [12, 15, 25, 32, 33], GA-based optimisation techniques as described in chapter 4 were introduced in this thesis to provide a reliable and systematic survey of the square-shoulder system's strategies to form stable ordered configurations.

In this section, we present the results of our investigations on the equilibrium structures of the two-dimensional square-shoulder system.

6.1.1 Ordered equilibrium structures

We investigate the formation of ordered structures in the system by systematically varying the pressure P for five different values of shoulder width, $\lambda = 1.5\sigma, 3\sigma, 5\sigma, 7\sigma$, and 10σ , where σ is the diameter of the impenetrable core of the particles. All calculations are performed in an NPT -ensemble, so that the equilibrium structures are characterised by a minimal Gibbs free energy (cf. section 3.2),

$$G = U - ST + PA \quad , \quad (6.1)$$

where U is the internal energy of the structure, S the system's entropy, T is the temperature, P the applied external pressure, and A the area of the system. As we choose to investigate the zero-temperature phase diagram of the square-shoulder system, the entropic contribution to the

Gibbs free energy vanishes, due to the constraint $T = 0$ (cf. section 3.3.2).

Instead of the Gibbs free energy given in equation (6.1), we use the Gibbs free energy per particle in standard reduced units in our investigations:

$$G^* = \frac{G}{N\varepsilon} = U^* + \frac{P^*}{\eta\sigma^2} \quad , \quad (6.2)$$

where $U^* = U/(N\varepsilon)$, $P^* = (P\sigma^2)/\varepsilon$, and $\eta = N/A$ is the particle area density of the system, with N being the number of particles present. In order to compare the results for the different values of λ , we additionally scale all thermodynamic quantities with the maximal internal energy U_{\max}^* obtained for each shoulder width.

To find the global minimum of the Gibbs free energy for every pressure value and shoulder width λ , we employ genetic algorithms, as they were introduced in section 4.2. The ordered lattice structures were either parametrised using the standard description of crystal lattices or via a cluster-biased parametrisation according to section 4.2.1. As the investigated particles exhibit an impenetrable hard core, the parametrisations were adapted accordingly (see section 4.2.1.3).

The special form of the interaction potential (2.1) leads to characteristic forms of U^* and G^* as functions of P^* : each structure is characterised by its number of corona overlaps, so that the internal energy U^* of this structure has a fixed rational value, given by the number of corona overlaps per particle. As long as the structure does not change, the internal energy is the same, irrespective of the applied pressure. The same is true for the particle area density: as long as the structure remains the same, the density retains its value. The corresponding Gibbs free energy $G^*(P^*)$ of a single structure is therefore given by a straight line of slope $1/\eta$ in a G^* - P^* -diagram according to equation (6.2). We can identify two limiting structures in this context, which occur for all values of the shoulder width λ : at very low pressure, the system will arrange so that discs of diameter λ form a hexagonally close-packed structure. As no overlaps of coronas occur in this configuration, the internal energy vanishes, $U_{\text{low}}^* = 0$, and we can write

$$\eta_{\text{low}} = \frac{N}{A_{\text{hex}}(\lambda)} = \frac{2}{\sqrt{3}\lambda^2}$$

for the particle area density. The configuration of maximal internal energy and density is encountered at high values of the pressure and is given by another hexagonally close-packed structure, where the hard core of each particle is in direct contact with its six nearest neighbours. The internal energy thus reaches its maximal value, $U_{\text{high}}^* = U_{\max}^*(\lambda)$ and the particle area density of this incompressible structure can be written as

$$\eta_{\text{high}} = \frac{N}{A_{\text{hex}}(\sigma)} = \frac{2}{\sqrt{3}\sigma^2} \quad .$$

As η_{low} and η_{high} are the minimal and maximal values of the particle area density, all minimum

energy configurations (abbreviated "MECs", "MEC" in singular) for a given shoulder width λ have to be located on straight lines of slope $1/\eta$ with

$$\frac{1}{\eta_{\max}} \leq \frac{1}{\eta} \leq \frac{1}{\eta_{\min}} \quad ,$$

in an G^*-P^* -diagram. It is this fact we use to construct an algorithm for a systematic scan along the pressure axis: we first determine the pressure value which corresponds to the intersection point of the two lines representing the above discussed limiting cases in the G^*-P^* -diagram. For this pressure value, a GA is then employed, leading to a configuration of lower Gibbs free energy. This Gibbs free energy of the newly found structure is again represented by a straight line which can be intersected with the previous lines, yielding two new pressure values. At these values, GA runs are again performed. By iterating this procedure, we are able to investigate the whole pressure regime efficiently, without risking to miss a MEC due to an inappropriately spaced pressure grid. The Gibbs free energy $G^* = G^*(P^*)$ is obtained as a sequence of intersecting straight lines over the entire pressure range (see references [74, 75] for further details).

We start with our survey at a shoulder width of $\lambda = 1.5\sigma$ and show the MECs proposed by the GA in figure 6.1: at very low pressure, the particles were found to populate an ideal hexagonal lattice, avoiding overlapping coronas. Upon compression, the system must pay tribute to the reduced space in terms of an energy penalty, i. e. via a first overlap of shoulders, and lane-formation emerges as an energetically convenient solution. Along the lanes, particles are in direct contact, forming a one-dimensional close-packed arrangement. Parallel lanes try to avoid corona overlap and the shoulder width λ serves as a spacer (see magnified view in figure 6.1). As the pressure is further increased, new strategies are required to arrange particles in an energetically favourable way. While particles still prefer alignment along lanes, the internal arrangement is modified: rather than forming straight lines, the lanes are now zig-zag shaped, which is a tradeoff between the reduced available space and the energetic penalty due to additional corona overlaps. Neighbouring lanes are arranged in a way that each particle is now in direct contact with three others (see magnified view in figure 6.1). These staggered lanes can also be viewed as ring-like structures where six particles form elongated rings with λ fixing the width of the cage. Further compression causes the system to collapse into the hexagonally close-packed structure, where each particle is in direct contact with its six nearest neighbours.

Figure 6.2 displays the corresponding thermodynamic properties $G^*(P^*)$ and $U^*(P^*)$, where the characteristic features mentioned above are clearly visible: the internal energy appears as a distinct sequence of flat plateaus, each representing one of the MECs found, whereas the individual line segments, which compose the Gibbs free energy are also easily recognised in the G^*-P^* -diagram.

As we proceed to a shoulder width of $\lambda = 3\sigma$, the system develops completely different strate-

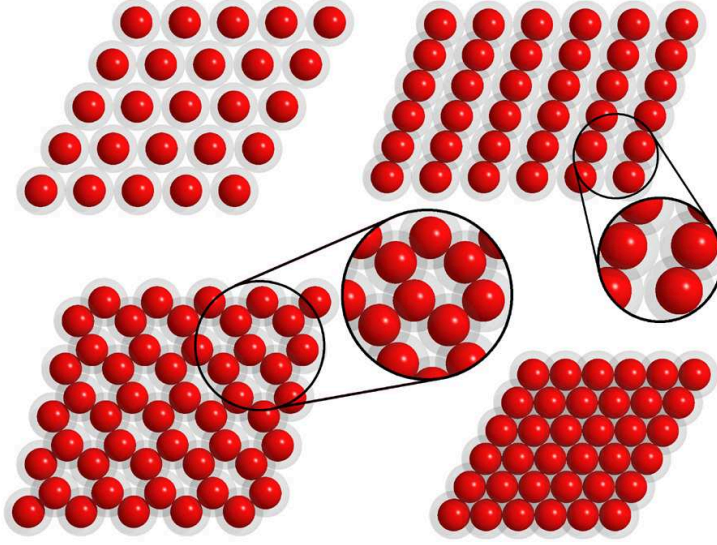


Figure 6.1: Complete sequence of MECs for the square-shoulder system of shoulder range $\lambda = 1.5\sigma$. Red spheres mark the particles' hard cores, whereas the repulsive shoulders are depicted as grey coronas. Configurations correspond (from left to right and from top to bottom) to pressure values indicated in figure 6.2 by vertical arrows.

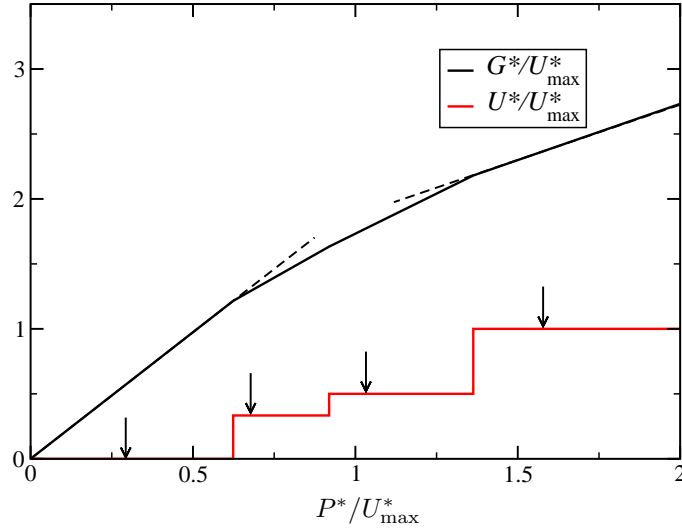


Figure 6.2: Gibbs free energy (black line), G^* , and internal energy (red line), U^* , as functions of P^* for a system of shoulder range $\lambda = 1.5\sigma$, all scaled with $U_{\max}^* = 3$, the internal energy of the hexagonally close-packed structure. Vertical arrows indicate MECs depicted in figure 6.1. Broken lines indicate limiting cases of MECs (see text).

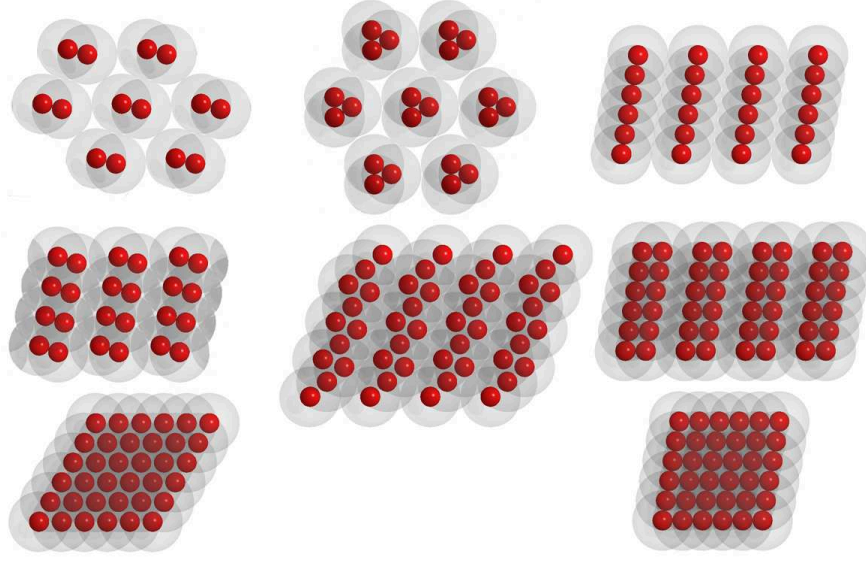


Figure 6.3: MECs for the square-shoulder system of shoulder range $\lambda = 3\sigma$. Configurations correspond (from left to right and from top to bottom) to pressure values indicated in figure 6.4 by vertical arrows. The sequence shown here is a representative selection from the MECs found. The full sequence can be found in appendix B.

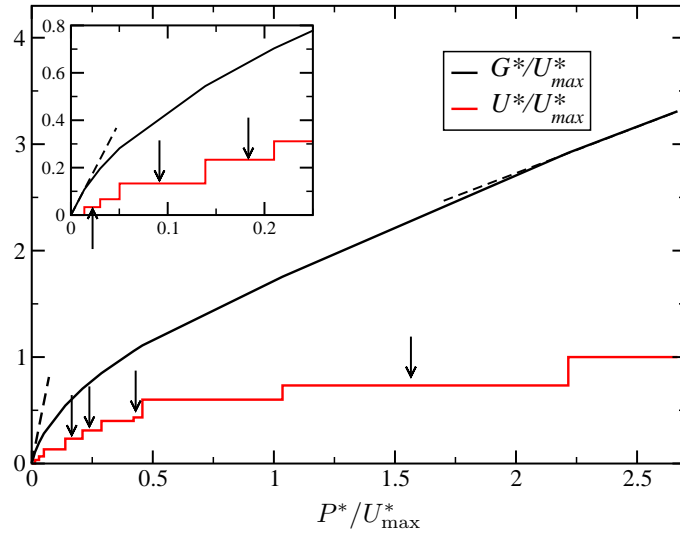


Figure 6.4: Gibbs free energy (black line), G^* , and internal energy (red line), U^* , as functions of P^* for a system of shoulder range $\lambda = 3\sigma$, all scaled with $U_{\max}^* = 15$, the internal energy of the hexagonally close-packed structure. Vertical arrows indicate MECs depicted in figure 6.3. Broken lines indicate limiting cases of MECs (see text).

gies to form MECs as the pressure is increased, leading to a considerably broader variety of different structures. The configurations shown in figure 6.3 capture the general trends observed by presenting a selection from the full sequence of MECs found, whereas the corresponding thermodynamic properties are displayed in figure 6.4.

The hexagonal pattern imposed by the non-overlapping coronas, which is observed for very low pressure values only and not displayed in figure 6.3, is soon superseded by a novel strategy, namely the formation of clusters. At low pressure, dimer- and trimer-clusters are observed to form distorted hexagonal lattices, where the degree of distortion is imposed by the shape of the clusters. In this way, the dimers form a strongly distorted lattice, whereas the trimers sit on an almost ideal hexagonal structure. As the system is further compressed, the formation of clusters becomes energetically less attractive and lane-formation sets in. In the beginning, each lane is built up by a single, linear chain of particles, resembling the first lane scenario encountered for $\lambda = 1.5\sigma$, but for increasing pressure, the internal architecture of the lanes gets more complex: besides the lanes formed by single chains of particles mentioned above, we observe a dense dimer phase, that can easily be interpreted as a lane-like scenario, a striped phase of double chains and pearl-necklace structures. As the pressure is increased further, the system collapses to close-packed structures characterised by a compact distribution of particles, until the high pressure limit of a hexagonally close-packed structure is finally reached, where the hard core of each particle is in direct contact with its six nearest neighbours.

This considerably richer wealth of MECs encountered for $\lambda = 3\sigma$ is reflected by the increased number of energy levels in the plot U^* vs. P^* and the number of intersecting straight line segments in the G^* - P^* -diagram in figure 6.4. The complete sequence of stable structures identified with the GA can be found in appendix B.

For $\lambda = 5\sigma$, the general trends already observed in the previous cases of $\lambda = 1.5\sigma$ and 3σ get more pronounced (see figure 6.5). Again, the structures presented in figure 6.5 are a representative selection from the complete sequence of MECs found for $\lambda = 5\sigma$, which is displayed in full detail in appendix B. Figure 6.6 displays the behaviour of the Gibbs free energy, G^* , and the internal energy per particle, U^* , for increasing pressure.

The low pressure regime is populated by clusters, arranged on an underlying distorted hexagonal lattice. As the pressure increases, those aggregates become larger until they reach a size of four particles. Upon further compression, the system again prefers to form lane-like structures of various shapes: we observe striped phases with up to four particles per lane as well as parallel zig-zag-shaped lanes. The increasing complexity of the inner structure of the lanes makes simple energetic explanations in terms of overlapping coronas hard to perceive, but the magnified views in figure 6.5 give evidence that the formation of the different lane structures is an efficient strategy to avoid an overlap between the coronas of particles belonging to neighbouring lanes. Above a certain pressure threshold, the formation of lanes is no longer energetically favourable and the

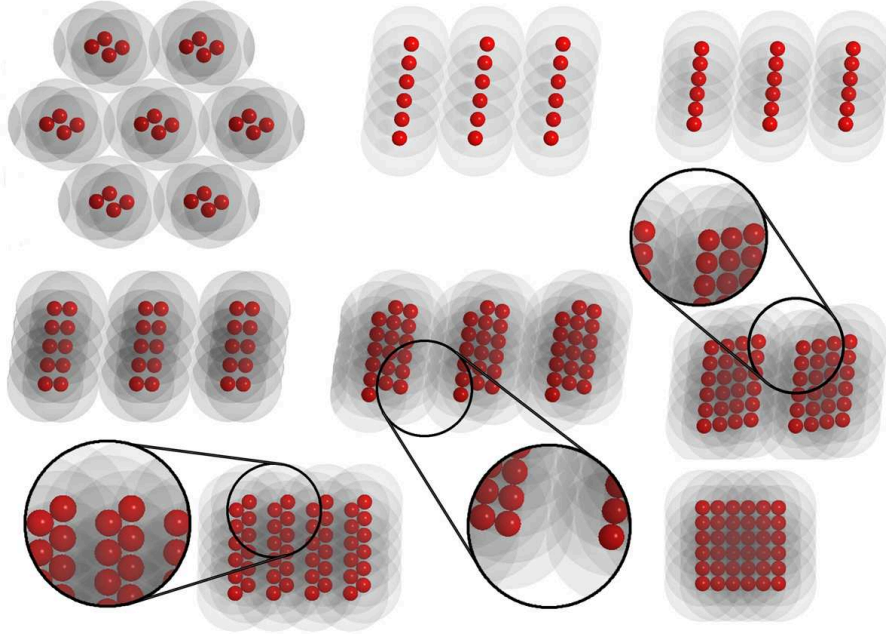


Figure 6.5: MECs for the square-shoulder system of shoulder range $\lambda = 5\sigma$. Configurations correspond (from left to right and from top to bottom) to pressure values indicated in figure 6.6 by vertical arrows. The sequence shown here is a representative selection from the MECs found.

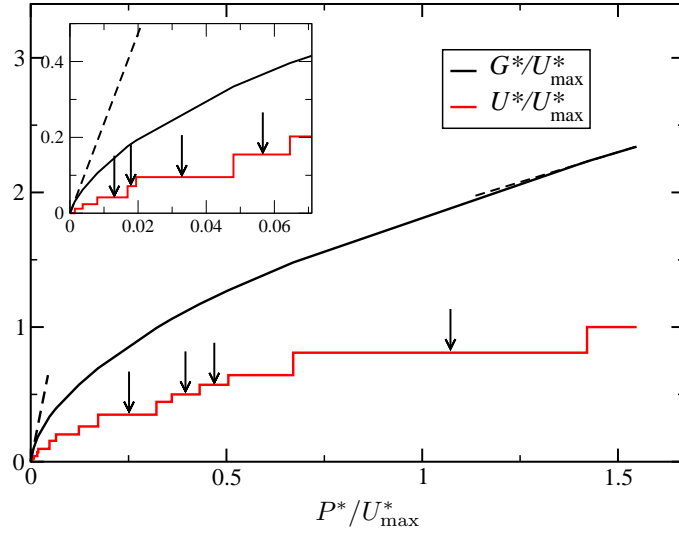


Figure 6.6: Gibbs free energy (black line), G^* , and internal energy (red line), U^* , as functions of P^* for a system of shoulder range $\lambda = 5\sigma$, all scaled with $U_{\max}^* = 42$, the internal energy of the hexagonally close-packed structure. Vertical arrows indicate MECs depicted in figure 6.5. Broken lines indicate limiting cases of MECs (see text).

system collapses to compact configurations with a dense distribution of particles, like the square lattice shown in figure 6.5.

Additionally, we encounter a phenomenon, that can be interpreted as a first observation of a narrow cross-over region from cluster-populated lattices to striped phases: single particles arrange in chains with two different inter-particle separations along the lane (cf. appendix B).

The complexity of internal arrangements increases further in all three types of encountered structures – clusters, lanes and compact arrangements – as the shoulder width changes to $\lambda = 7\sigma$. Figure 6.7 shows a representative collection of the already considerably large number of MECs proposed by the GA (see appendix B for the full sequence of stable configurations). The internal and Gibbs free energy per particle as a function of the pressure, $U^*(P^*)$ and $G^*(P^*)$, are displayed in figure 6.8.

Starting from the low density hexagonally close-packed structure, which is not depicted in figure 6.7, we observe clusters of growing size for increasing pressure: the dimers shown in figure 6.7 are soon superseded by trimers, and later by clusters consisting of four, six, or even eight particles. The eight-particle clusters are of an almost circular shape as can be seen in the magnified view in figure 6.7 and thus allow for an arrangement very close to the energetically favoured hexagonal configuration. Although the eight-particle cluster structure was found to be stable over a comparatively large range of pressure values (see figure 6.8), we however have to note that the occurrence of this particular cluster size is possibly due to the chosen parametrisation of lattices: the cluster-biased parameterisation as introduced in section 4.2.1 favours the formation of clusters consisting of six or eight particles, whereas clusters of seven particles, which allow for perfectly symmetric aggregates even closer to the preferred circular shape, are not available to the cluster-biased parameterisation and can enter the survey only via calculations employing the standard description of two-dimensional lattices (cf. section 4.2.1).

Similar to the cluster phases, also the lane-like structures increase in complexity as the shoulder width increases to $\lambda = 7\sigma$: arrangements of lanes that are two, three, four and six particles wide are found in the intermediate pressure regime, displaying a broad variety in their internal architecture. Surprisingly, structures consisting of single-particle chains fail completely to show up among the discovered MECs.

Furthermore, we can now distinguish two different cross-over regions for systems of shoulder width $\lambda = 7\sigma$: first, a cross-over regime from the clustered phases to the lane-like scenarios similar to the one observed for systems with $\lambda = 5\sigma$, where dimers arrange in lanes with the inter-dimer distance within one lane gradually decreasing as more pressure is applied to the system. Second, we observe a cross-over from lane-like structures to the compact configurations encountered at high pressure values, as dense particle distributions are found to alternate with phases exhibiting distinct stripes.

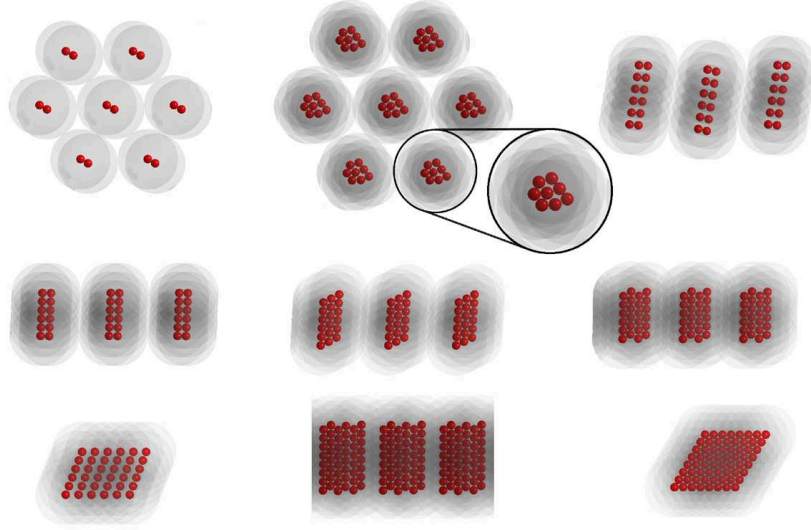


Figure 6.7: MECs for the square-shoulder system of shoulder range $\lambda = 7\sigma$. Configurations correspond (from left to right and from top to bottom) to pressure values indicated in figure 6.8 by vertical arrows. The sequence shown here is a representative selection from the MECs found.

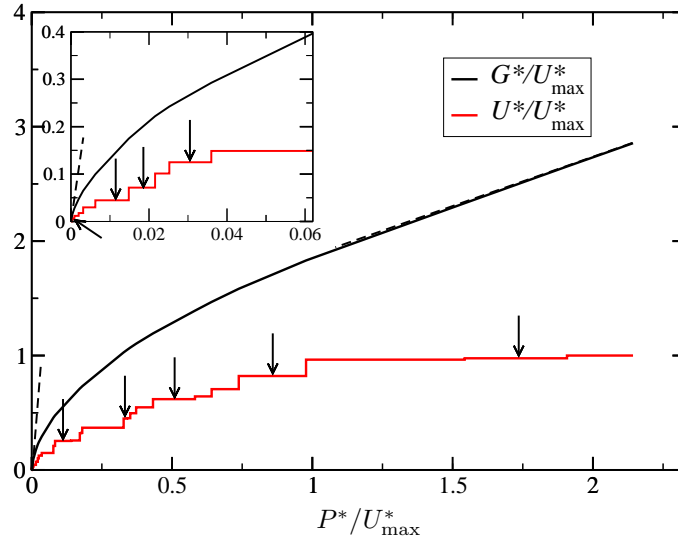


Figure 6.8: Gibbs free energy (black line), G^* , and internal energy (red line), U^* , as functions of P^* for a system of shoulder range $\lambda = 7\sigma$, all scaled with $U_{\max}^* = 84$, the internal energy of the hexagonally close-packed structure. Vertical arrows indicate MECs depicted in figure 6.7. Broken lines indicate limiting cases of MECs (see text).

Finally, for $\lambda = 10\sigma$, the largest shoulder width investigated, the strategies of the system to arrange particles in energetically favourable configurations seems to be similar to the previous cases at first sight: the hexagonal pattern of minimum density, which is not included in the selection of MECs shown in figure 6.9, is soon replaced as the system prefers the formation of clustered lattices. The formation of lanes of increasingly complex inner structure is preferred at intermediate and high pressure values, and the cross-over regions, first from cluster-shaped particle arrangements to lane-like structures and second from lanes to the compact regime are both visible and more pronounced as in the previous cases.

The differences between the MECs of the comparatively large shoulder length of $\lambda = 10\sigma$ and those obtained for the intermediate values discussed above, are of subtle nature and concern the internal arrangement of particles in the structures: although the growing cluster arrangements are located on slightly distorted hexagonal lattices as in the previous cases, the system's strategy to form MECs has changed, as we observe that inside a cluster the cores of the particles sometimes arrange in a disordered fashion (see magnified views in figure 6.9 and Appendix B), while for intermediate values of λ only clusters with an ordered internal particle arrangement occur. The reason for this change is obviously the following: once λ is sufficiently large to support cluster-formation, the system tries to arrange particles in clusters shaped as circular as possible. In turn, this guarantees that the underlying structure is close to the energetically most favourable hexagonal lattice. For intermediate shoulder widths, where the core region still represents a considerable fraction of the particle diameter, the system has to proceed rather carefully to fulfil this requirement, leading to an ordered arrangements of the cores. For $\lambda = 10$, however, the core region is nearly negligible with respect to the corona width. Now both regular and irregular particle arrangements inside the core can lead to circular-shaped clusters of the same size, having practically the same G -value (see figure 6.10).

If we extrapolate these results to even larger values of λ – or, equivalently, to a vanishing core – and briefly switch to three dimensions, we arrive at another soft matter model system that has been studied in detail in literature: the penetrable sphere model (PSM) [91]. Among the remarkable, well-documented features of this system is its ability to form cluster phases: at sufficiently high densities clusters of overlapping particles populate the lattice sites of a regular fcc lattice [92]. Detailed simulations of a closely related system that also shows clustering [13] have revealed that the internal structure of the clusters is completely random. These observations are consistent with our results in the sense that an increasing corona width (or, equivalently, a vanishing core) favours formation of disordered clusters of particles, which in turn populate sites of regular lattices. Obviously, first precursors of this phenomenon occur in systems of shoulder width $\lambda = 10\sigma$ [73, 93].

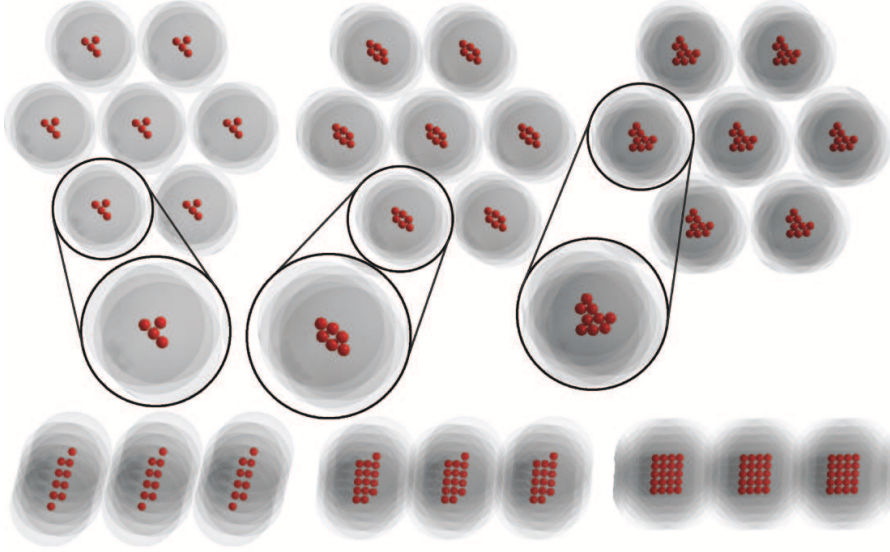


Figure 6.9: MECs for the square-shoulder system of shoulder range $\lambda = 10\sigma$. Configurations correspond (from left to right and from top to bottom) to pressure values indicated in figure 6.10 by vertical arrows. The sequence shown here is a representative selection from the MECs found.

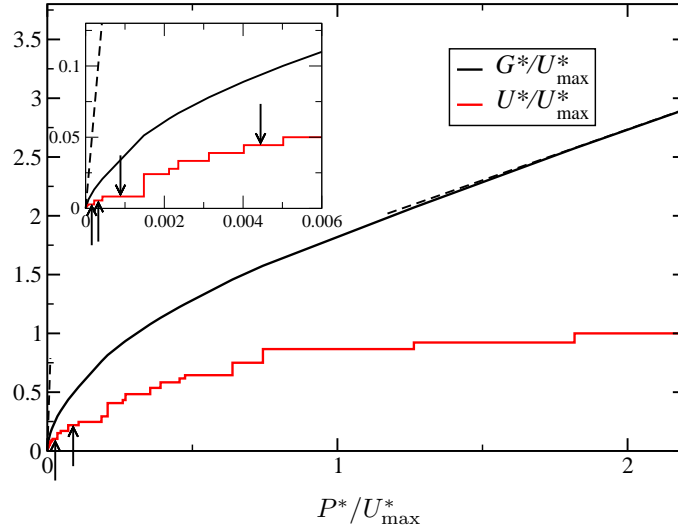


Figure 6.10: Gibbs free energy (black line), G^* , and internal energy (red line), U^* , as functions of P^* for a system of shoulder range $\lambda = 10\sigma$, all scaled with $U_{max}^* = 180$, the internal energy of the hexagonally close-packed structure. Vertical arrows indicate MECs depicted in figure 6.9. Broken lines indicate limiting cases of MECs (see text).

6.2 Binary mixture of dipolar colloids

In this section we investigate the minimum energy configurations formed by a binary mixture of dipolar colloids. The two involved particle species differ in size and thus in their dipole moment, leading to distinctly different potentials acting between the species (cf. section 2.2). After presenting the results obtained with our search strategy based on genetic algorithms, we compare our findings to experimental data and to structures discovered in simulations. The last part of this section is dedicated to the phonon band structures of the found equilibrium configurations; in particular we focus on the influence of the system parameters on the functional form of the dispersion relations.

6.2.1 Ordered equilibrium structures

The two parameters to be varied when investigating the ordered equilibrium structures of the dipolar binary mixture are the particle size ratio $z = R_B/R_A$ and the concentration of small particles in the system, $C = n_B/(n_A + n_B)$ (cf. section 2.2), where A labels the bigger particle species and B the smaller one. n_i is the number of particles of species i in the system. Here we consider structures with a particle area density $\eta\sigma^2 = (n_A + n_B)/A = 0.6$, a value for which we believe the average inter-particle distance to be still large enough to guarantee that the interactions are close to the ideal dipole-dipole behaviour (cf. section 2.2).

Due to practical reasons we have limited the number of particles per unit cell to $n_p = n_A + n_B = 8$, as the computational cost increases substantially with the number of particles and the GA-search is not able to find the global minimum of the free energy reliably if too many parameters are to be optimised. Thus, we can investigate values for the concentrations of the smaller particles, C , in the range of $C = 1/8, \dots, 7/8$. For particular fixed C -values we could therefore perform independent GA-runs for a given state point using unit cells of different size: for instance, a system with $C = 1/2$ could be realised using 2, 4, 6 or 8 particles per cell. Finally, we have also included the case $C = 2/9$ (i. e., $n_A + n_B = 9$) in our investigations, since this particular ratio is known to give rise to highly asymmetric structures [94].

In order to guarantee a high reliability of our method, each state point (characterised by concentration C and particle size ratio z) is considered in a two-step process: First, several independent GA-runs are performed with a cutoff radius r_c of considerable size (see below). These obtained structures and their respective energies are compared. The lattice with the overall lowest free energy is re-considered in the second step, but now with an even larger cutoff radius. The structure that emerges from this search is then taken as the MEC for this particular state point. This rather high numerical effort might seem exaggerated at first sight, but we have good reasons for this strategy: the large number of parameters that characterises a two-dimensional lattice leads to a rough energy landscape and the slowly decaying potential is responsible for the sensitivity

of the fitness function to the numerical parameters. Thus, GA-runs carried out for one state point using a moderate cutoff radius do not necessarily converge to the same energetic minimum, which forces us to suitably adapt the algorithm's parameters (i.e. the mutation rate, the number of individuals per generation etc.). Furthermore, performing identical runs provides additional information on the roughness of the energy landscape in the immediate surrounding of the found energy minimum and makes degenerate structures accessible (see below).

We used the following values for the numerical parameters in our investigations: In every run 200 generations were calculated, consisting of 1000 individuals each. The mutation rate was set to $p_m = 0.01$. For the encoding step we use twelve bits to encode a number, i.e. for the lattice parameters x , α_i , and β_i , and six bits for the angle ϕ (cf. section 4.2.1), as our numerical tests have given evidence that a larger number of genes does not increase the efficiency of the GA. Due to the slow decay in the inter-particle potentials, we have used in the first search step outlined above a cutoff radius, $r_c = 200\sigma_A$ for the evaluation of the lattice sum. This value for r_c guarantees even at high densities that an increase of r_c by 10% leads to a relative change of the lattice sum of less than 0.01%. For the second step in our search strategy, i.e., for the overall best structure, a cutoff $r_c = 1500\sigma_A$ was used.

In figures 6.11-6.14 we present the minimum energy configurations obtained with the GA-based search strategy described above for our mixture of dipolar colloids. For clarity we show our results on four different panels: Figure 6.11 shows the structures for concentrations of small particles $C \leq 1/2$ and particle size ratios z ranging from 0.1 to 0.41. Figure 6.12 contains the structures for the size ratios up to $z = 0.9$ at the same concentrations of small particles. Figures 6.13 and 6.14 show the minimum energy configurations obtained for $C > 1/2$. Structures of z -ratios marked by a star in figures 6.11 and 6.13 were originally obtained for $n = 2$ and rescaled using relation (2.9). All shown configurations are of a particle area density of $\eta\sigma^2 = 0.6$.

The main general trend to be observed for all investigated concentrations is the system's tendency to form lanes at large particle size ratios ($z \geq 0.5$, for examples see especially figure 6.14, (a)-(o)). This inclination to stripe-like structures might indicate a region of phase separation, a phenomenon not directly accessible due to our search algorithm's inherent restriction to periodic structures.

At $z = 0.8$ and above, the difference in size between the two particle species is no longer pronounced enough to produce distinctive deviations from a compact hexagonal lattice (see figure 6.12 (m)-(t) and figure 6.14 (p)-(y); the different colouring of the particles can be misleading to the eye in this respect). Additionally, the GA experiences difficulties in finding the global energy minimum as the energy-landscape flattens out due to the potentials getting increasingly alike. We will therefore exclude the results obtained for particle size ratios larger than $z = 0.7$ from the following discussion, and we will also omit the many degenerate structures, i.e. structures that

differ in their arrangement of particles but correspond to the same energy, found for $z \geq 0.8$ from our survey.

Results for $C \leq 1/2$

We start a more detailed discussion with the lattices obtained for $C \leq 1/2$ as their common features are easily visible. Increasing the concentration of small particles C results in decreasing the size of the area occupied by a hexagonal lattice formed only by the large particles. The particle size ratio z on the other hand influences the form of the cage, the large particles build around the small ones. If z is small, the small particles are incorporated into the hexagonal lattice of the large ones without disturbing their immediate surrounding ($z = 0.1 - 0.2$, see figure 6.11, (a), (b), (e), (f), (i), and (j)) so that they populate the centres of equilateral triangles of large particles. As z increases, the influence of the size of the small particles on their surrounding becomes more pronounced and the triangles of large particles around the small ones are distorted; first to a rhomboid ($z = 0.28$, figure 6.11, (m) and (n)) and then to a square with the small particle sitting at the centre ($z = 0.3296 - 0.5$, figure 6.11, (q) to (x), and figure 6.12, (a) to (d)). Finally, the square cage formed by the large particles then deforms to a rectangle (for examples see figure 6.12, (e), (f), (g), (i), and (j)), until it finally meets the requirements to fit into a hexagonal lattice and, for $z \geq 0.8$, we arrive at the compact case (see figure 6.12, the rectangle is clearly visible in (m), (n), and (q)). In the case of $C = 1/3$ and $1/2$, an additional phase appears for small values of z ($z \leq 0.28$). The triangular cages of the large particles arrange next to each other in alternating orientation, and stripes of small particles, meandering through a slightly deformed hexagonal lattice of large ones, emerge. We believe that similar ground states are to be expected for $C = 1/7$ and $1/5$, but which were inaccessible to our survey due to the limitation to a maximum of eight particles per cell.

We would like to point out that all the various structures displayed in figures 6.11 and 6.12 are built up by only a small number of different lattice elements or "tiles": an equilateral triangle of large particles, possibly decorated by a small one in its centre (see figure 6.11 (a) or (b) for examples), a lozenge of large particles containing a pair of small ones, which is aligned along the longer diagonal (e.g. figure 6.11, (d)), a large rectangle or square decorated by a small particle (e.g. figure 6.12, (i) or (c)), and an distorted hexagon with two small particles inside (figure 6.12, (h), (k), and (l)). We believe that this occurrence of "tiled" phases might be an indicator of the occurrence of so called "random tiling" phases [94] or even quasi-periodic structures – both are scenarios inaccessible to our search strategy.

Results for $C > 1/2$

General trends for mixtures with an abundance of small particles in the unit cell ($C > 1/2$) are harder to perceive as the structures get more complex with increasing C , though common features can be identified: at the very low value of $z = 0.1$, the small particles tend to group into small

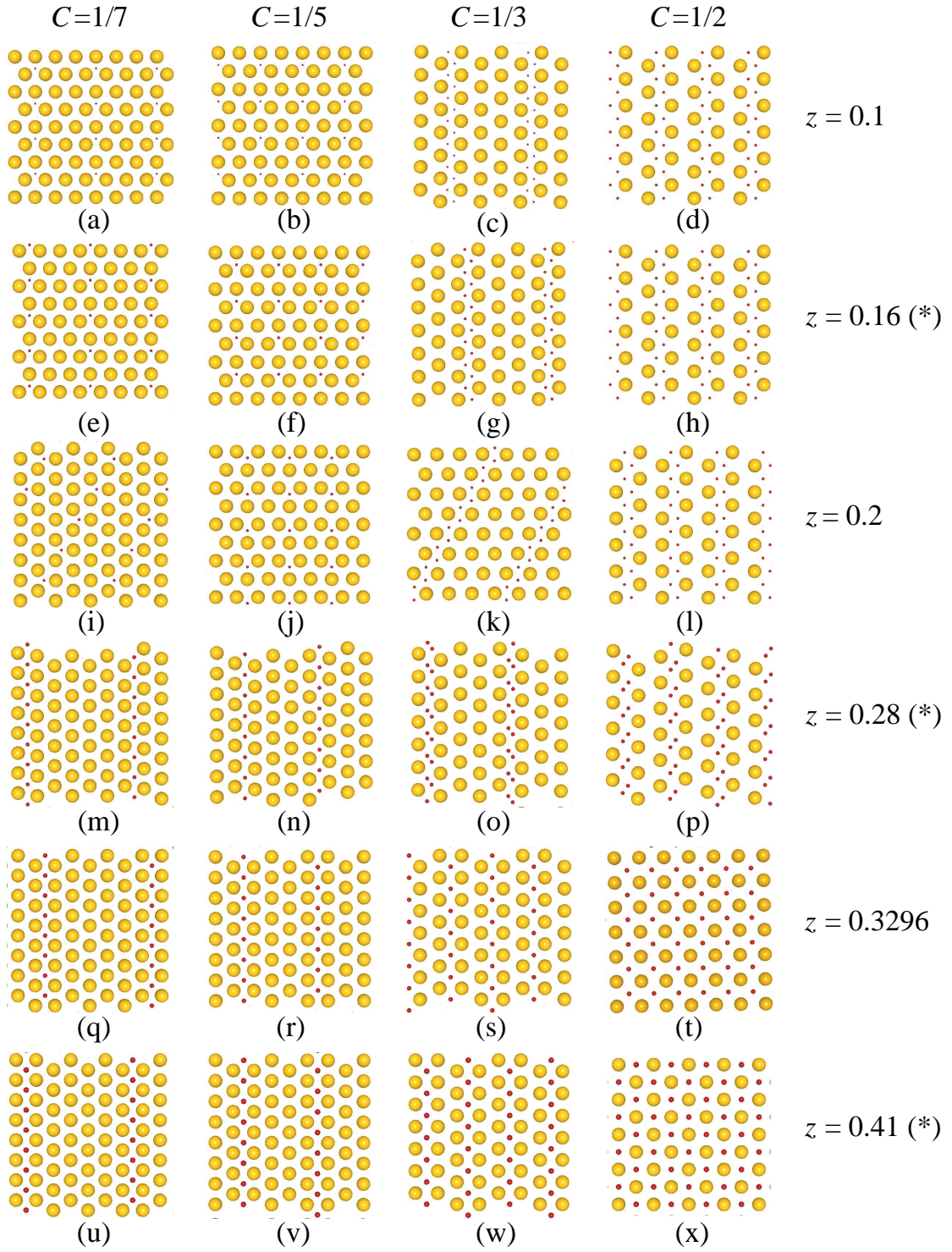


Figure 6.11: *Found minimum energy configurations for $C \leq 1/2$ and $z \leq 0.41$. The particles are not drawn to scale. Particle size ratios marked by a (*) were originally considered for $n = 2$ and rescaled using relation (2.9).*

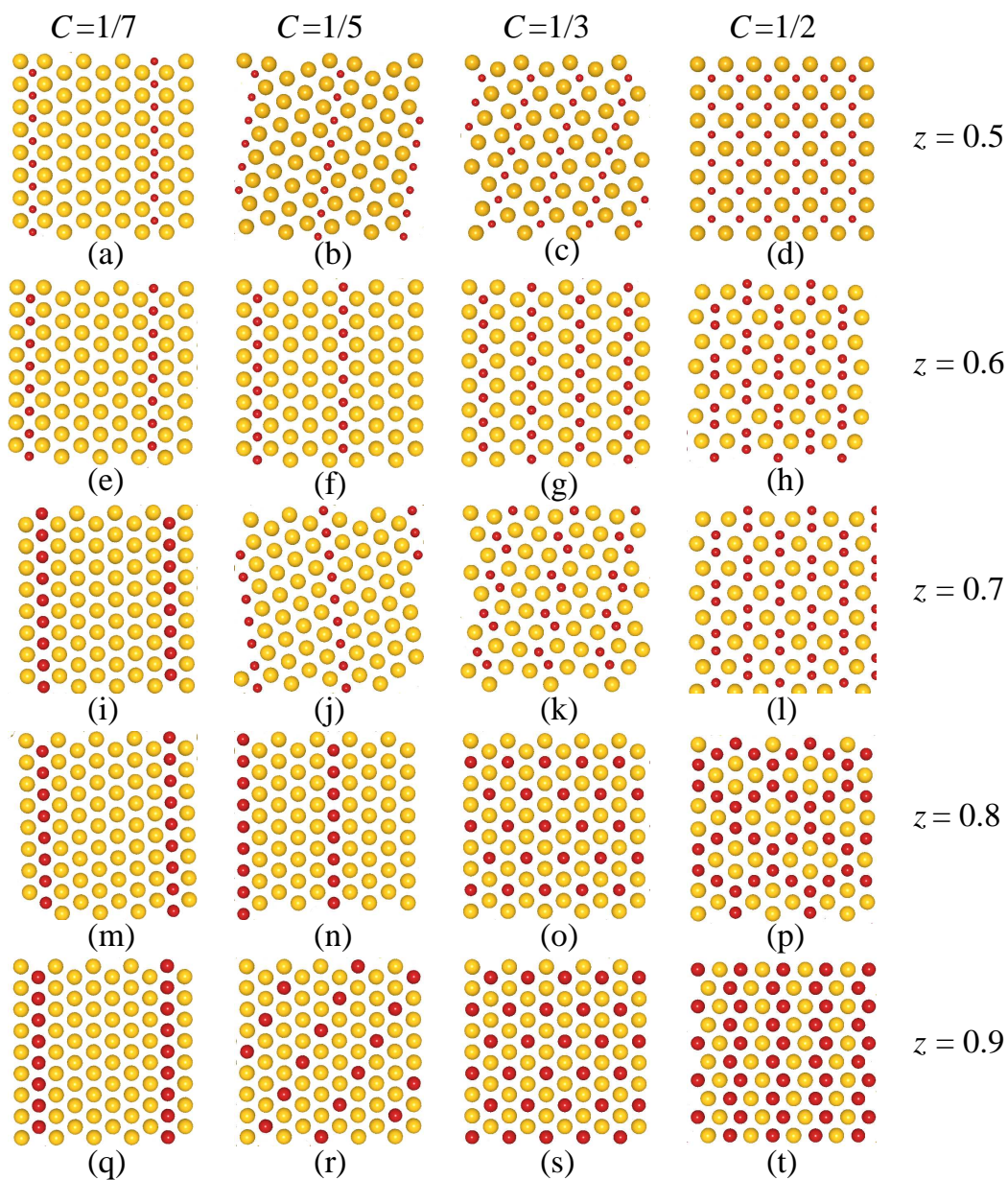


Figure 6.12: Found minimum energy configurations for $C \leq 1/2$ and $z > 0.41$. The particles are not drawn to scale.

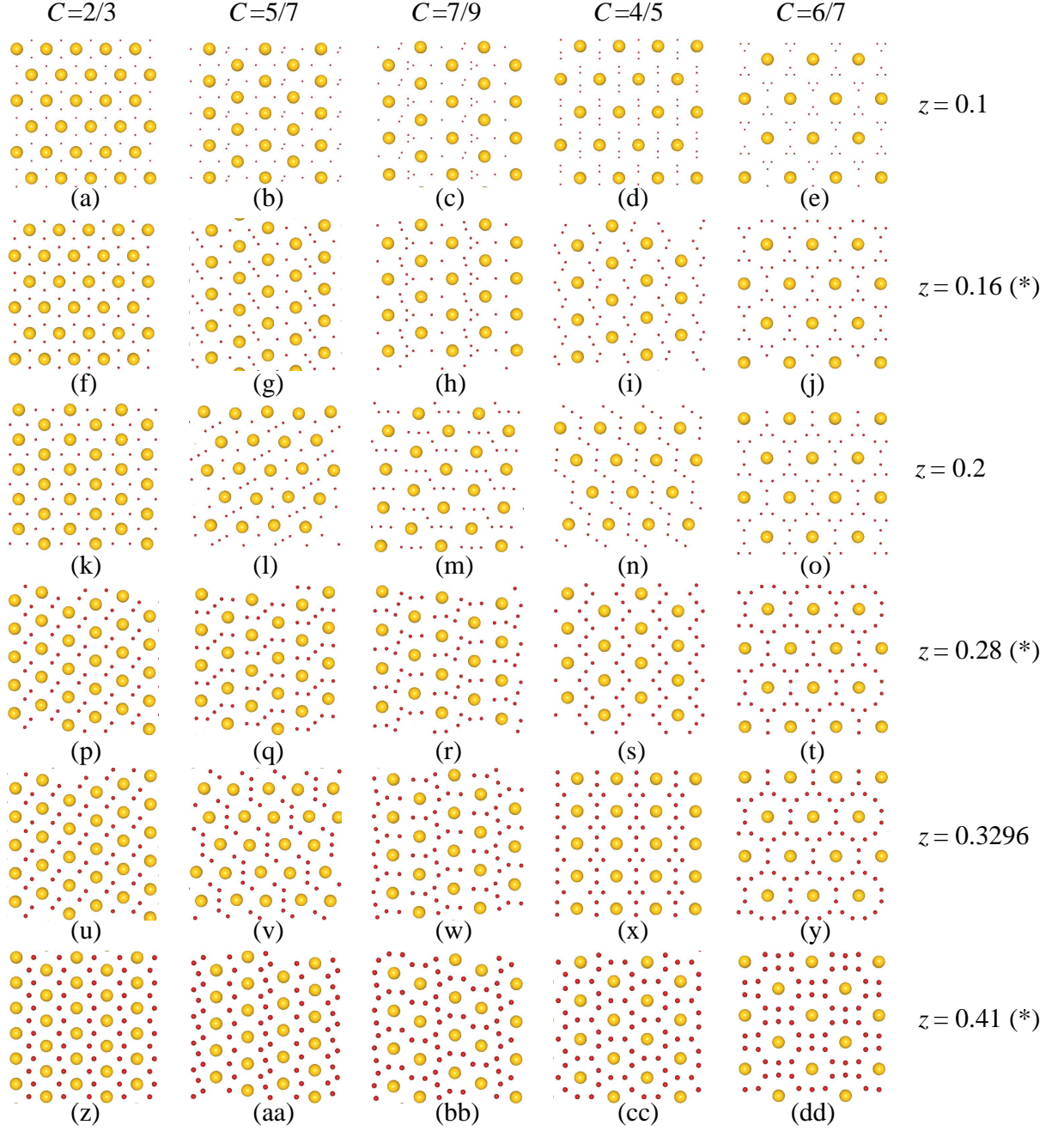


Figure 6.13: *Found minimum energy configurations for $C > 1/2$ and $z \leq 0.41$. The particles are not drawn to scale. Particle size ratios marked by a (*) were originally considered for $n = 2$ and rescaled using relation (2.9).*

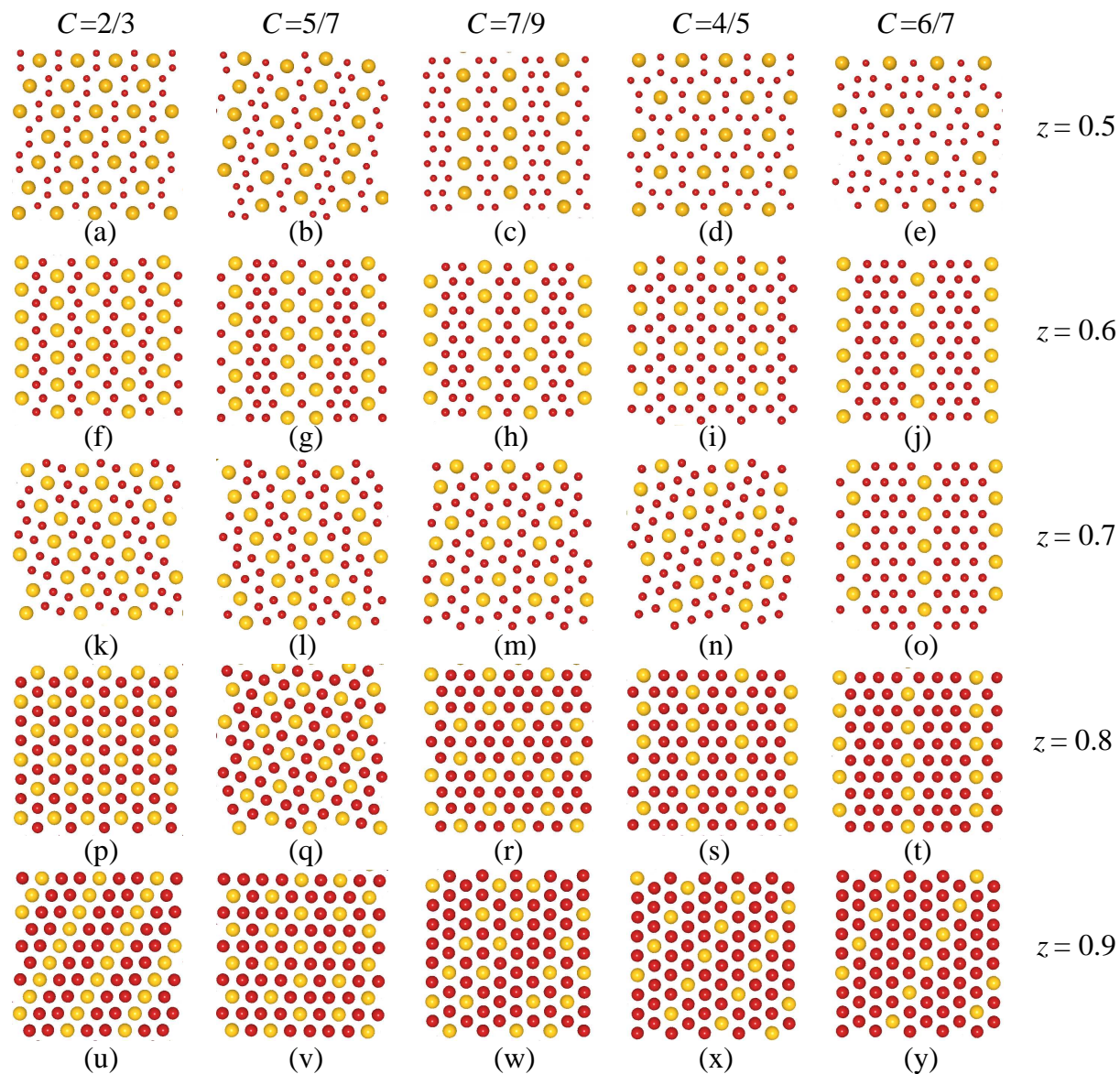


Figure 6.14: *Found minimum energy configurations for $C > 1/2$ and $z > 0.41$. The particles are not drawn to scale.*

clusters of various shape and occur as isolated single particles, populating the interstitials of an ideal hexagonal lattice of the large particles. As z increases, the formerly distinct groups of small particles merge ($0.1 < z \leq 0.41$), until finally stripe-like structures emerge ($0.41 < z \leq 0.7$).

We want to pay closer attention to how these complex structures form by discussing the obtained sequences in more detail. Because of the small unit cell involved, the general trend is clearly reflected in the sequence at $C = 2/3$: We start out with isolated single particles at the interstitials of the large particles' hexagonal lattice ($z = 0.1 - 0.2$, figure 6.13, (a), (f), and (k)). If the small particles increase in size, two of them approach each other, first forming a distinct pair ($z = 0.28$ and 0.3296 , figure 6.13, (p) and (u)) and then – by a small change in the relative orientation of the originally parallel aligned dimers – pairs from adjacent cells combine to zig-zag shaped lanes ($z = 0.41 - 0.6$, figure 6.13, (z) and figure 6.14, (a) and (f)).

For the next higher concentration of small particles, $C = 5/7$, the obtained sequence is considered much more complex. At very small particle size ratios, we find dimers in addition to isolated single small particles located at the interstitials of the hexagonal lattice of large particles ($z = 0.1$, figure 6.13, (b)). Increasing the size of the small particles leads to one single particle joining the adjacent dimer and elongated trimers emerge for $z = 0.16$ and $z = 0.2$ (figure 6.13, (g) and (l)). With further increase in size, every trimer is joined by two additional single particles to form zig-zag shaped pentamers ($z = 0.28$ and 0.3296 , figure 6.13, (q) and (v)), which, in turn, merge to form lanes ($z \geq 0.4$). As soon as neighbouring pentamers are close enough to merge, they "share" the particles at their respective ends and an additional, less populated lane of small particles emerges ($z = 0.41$, figure 6.13, (aa)). At size ratios from $z = 0.5$ to $z = 0.7$, rearrangements occur within the lanes, but the overall, stripe-like structure remains.

For $C = 7/9$, we encounter "cup-like" structures, where every large particle is surrounded by a ring segment of small particles (see figure 6.13, (r), (w), and (bb) for examples). The "cups" have their origin in the deformation of zig-zag-shaped heptamers, formed at low particle size ratios ($z = 0.2$, figure 6.13, (m)): increasing z first leads to a bending of the initially straight parts of the heptamers around the large particles in their surrounding ($z = 0.28$, figure 6.13, (r)). At a further increase of z neighbouring heptamers of small particles join together, thus forming the above mentioned cup-like arrangement of small particles around each of the large ones ($z = 0.3296$ and $z = 0.41$, figure 6.13, (w) and (bb)). At $z = 0.5$ and above, the cup-like features disappear and we arrive at a normal, lane-like lattice for $z = 0.5$ and $z = 0.6$, where neighbouring lanes formed by the small particles alternate in width and we can distinguish a hexagonal pattern in these stripes of small particles (see figure 6.14, (c) and (h)). For $z = 0.7$, we observe the arrangement of large particles into distinct pairs, as the lanes formed by the small particles are now interconnected (see figure 6.14, (m)).

This occurrence of "cups" can be interpreted as a precursor of the formation of rings, encountered for the concentrations $C = 4/5$ and $C = 6/7$. For $C = 6/7$, the rings of small particles surrounding the positions of the large ones, which in turn form a more or less ideal hexagonal

lattice, are already recognisable at very low values of z and remain stable over a long range of particle size ratios ($z = 0.1 - 0.3296$, figure 6.13, (e), (j), (o), (t), and (y)). The transition to the stripe-like phases takes place via a deformation of the underlying hexagonal lattice of the large particles ($z = 0.41$, figure 6.13, (dd)), to a slightly distorted square lattice at $z = 0.5$ (figure 6.14,(e)). This transformation is accompanied by a reduction of the number of small particles surrounding a large one from twelve ($z \leq 0.3296$), to ten ($z = 0.41$), and finally to nine at $z = 0.5$. At particle size ratios larger than $z = 0.5$, the system exhibits distinct stripes of large and small particles (see figure 6.14, (j) and (o)).

In the other case, at $C = 4/5$, we also observe the formation of small particle rings ($z = 0.41 - 0.6$, figure 6.13, (dd) and figure 6.14, (d) and (i)). This time they are not visible at small particle size ratios, but are preceded by a sequence of zig-zag-shaped or pearl-necklace lanes ($z = 0.16 - 0.3296$). Like at $C = 6/7$, the number of small particles forming a ring also becomes smaller at this concentration as z increases, starting with nine particles at $z = 0.41$ and $z = 0.5$ and diminishing to eight particles per ring at $z = 0.6$. For even higher values of z , the stripe scenario is realised once more.

Comparison to a hard-disc mixture

In an effort to understand the mechanisms leading to the observed minimum energy configurations, we compare our findings to the phase diagram of a hard disc mixture [94]. All of the ordered, periodic structures found to be stable in this study are also present in our current survey on dipolar colloids (see figure 6.15). Almost all of these lattices were found at z -values closest to the structures' "magical" values z^* , for which all neighbouring particles are in direct contact in the high-density, close-packed unit cell. For the parameter sets available through [94] and using the terms coined therein for the different lattices, we observe the following for the dipolar colloids:

At $C = 1/2$, the S_1 -structure is obtained for $z = 0.3296, 0.41$, and 0.5 and the H_2 -structure for $z = 0.6$ and 0.7 . At $C = 2/3$, the dipolar mixture forms T_1 -like structures at $z = 0.1 - 0.3296$ and H_1 -lattices at $z = 0.41 - 0.6$. An example of an H_3 -structure is found at $C = 7/9$, $z = 0.8$. S_2 occurs for $C = 4/5$, $z = 0.6$, while for $C = 6/7$, we encounter T_2 -structures in the range of $z = 0.1 - 0.3296$ (see table 6.1 for a summary).

Most differences occur because our method of investigation does not allow for non-periodic lattices like "lattice gas phases", "random tiling phases" or the possibility of a phase separation – all phenomena which were included in the survey of Likos and Henley [94]. Nonetheless, there are also cases in which the mixture of dipolar colloids shows a behaviour undiscovered in the hard-disc system: For low and intermediate values of z , the H_3 -structure ($C = 7/9$) is stable in the case of the hard-disc mixture [94]. The dipolar mixture shows distinctly different lattices throughout the whole range of particle size ratios (see figure 6.13, (c),(h), (m), (r), and (bb)), all of which were explicitly checked against the H_3 -structure and proved to be of lower energy. At $C = 4/5$, instead of the S_2 structure occurring for hard-discs, the dipolar mixture shows two different structures at

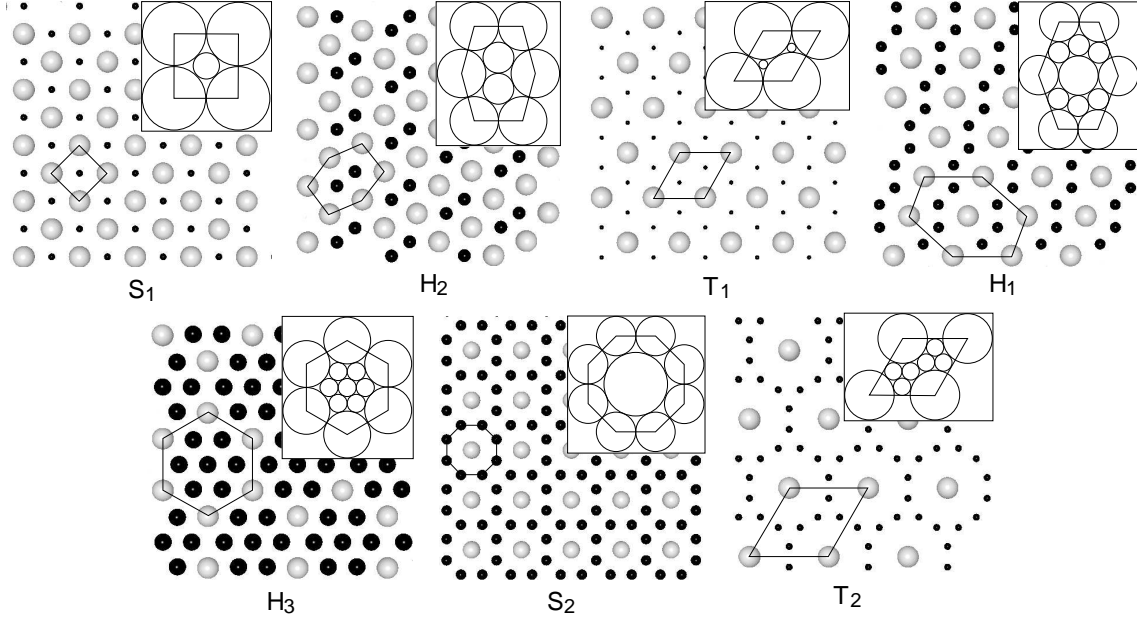


Figure 6.15: *Equilibrium structures of the dipolar binary mixture (large pictures) with the corresponding stable lattices of the hard-disc system (small pictures [94]). Symbols refer to the structures listed in table 6.1. A possible choice of the unit cell is marked in both cases.*

C	structure	z -values (dipolar colloids)	z -interval (hard-discs) [94]	z^* [94]
1/2	S_1	0.3296, 0.41, 0.5	[0.392, 0.414]	0.414
1/2	H_2	0.6, 0.7	(0.414, 0.438] \cup [0.627, 0.646]	0.637
2/3	T_1	0.1, 0.16, 0.2, 0.28, 0.3296	[0, 0.312]	0.155, 0.281
2/3	H_1	0.41, 0.5, 0.6	[0.517, 0.546]	0.533
7/9	H_3	0.8	(0.101, 0.110] \cup (0.378, 0.408]	0.386
4/5	S_2	0.3296, 0.6	(0.101, 0.123] \cup [0.193, 0.245]	0.216, 0.62
6/7	T_2	0.1, 0.16, 0.2, 0.28, 0.3296	[0, 0.157] \cup [0.315, 0.354]	0.101, 0.349

Table 6.1: *Comparison of the particle size ratios z for which certain structures were found for dipolar colloids (column 3) and in the hard-disc system (column 4). In the fifth column the "magical" particle size ratios z^* for each structure are given (see text).*

group	I	I	I	I	I	II	II	II	II
z	0.1	0.28	0.3296	0.41	0.41	0.1	0.2	0.41	0.6
C	1/5	1/7	2/3	2/3	4/5	1/2	1/2	1/3	7/9

Table 6.2: *Table of those values of the particle size ratio z and the concentration of small particles C for which degenerate structures were found for the binary mixture of dipolar colloids. The top row indicates the group of degenerate structures to which the individual cases belong to (see text).*

low z , both unique to the system: A hexagonal lattice of large particles with small dimers sitting at the interstitials (figure 6.13,(d)) and zig-zag-shaped lanes of small particles running through a hexagonal lattice of large particles (figure 6.13, (i)).

Degenerate structures

The method of investigation as introduced in the opening remarks of this section allows us to identify degenerate structures, i.e. configurations which differ in the arrangement of particles while corresponding to the same (minimal) value of the Helmholtz free energy.

As the numerical accuracy of our investigation procedure is mainly determined by the chosen cutoff radius in the calculation of the free energy, we define two structures to be energetically degenerate if the difference in their Helmholtz free energies per particle, ΔF , is of the same order of magnitude as the error due to the employment of a finite cutoff. Thus, two structures are considered degenerate, if their difference in energy is $\Delta F \lesssim 10^{-6}\varepsilon_I$, where ε_I refers to the energy scale of the system. ΔF thus corresponds to about 0.01% of the free energy per particle of the configurations in question.

In total, we encounter degenerate structures at nine of the 108 combinations of particle size ratio z and concentration C that were investigated (see table 6.2), excluding those configurations found at $z = 0.8$ and $z = 0.9$, where the difference between the particle species becomes very small and the GA experiences difficulties in identifying the global minimum of the Helmholtz free energy. These nine occasions of degeneracy can be divided into two groups: in the first group, labeled "I" in table 6.2, the additional structures resemble a particle arrangement previously encountered for a smaller or larger particle size ratio. The additional structure thus indicates a cross-over from one structure to another as the particle size ratio z changes. The second group, labeled "II" in table 6.2, consists of completely new configurations, which are not encountered at any other combination of z - and C -values.

The members of the first group are shown in figure 6.16, where in each respective panel on the right hand side, we see the structures already included into the overview of figures 6.11 to 6.14, while the additional, degenerate configurations are shown on the left hand side: for $z = 0.1$ and $C = 1/5$ (see figure 6.16, (a)), we find two configurations, which can be considered as tilings

formed by two different types of equilateral triangles of large particles. The first type is decorated by a small particle at its centre, the other tile is empty. In the first tiling, the two types of triangles share one corner, thus giving rise to distinct lanes of small particles running through the hexagonal lattice formed by the larger species (see figure 6.16, (a), left panel). In the other tiling, the two types of triangles share an edge, thus preventing the formation of lanes of small particles (see figure 6.16, (a), right panel). We interpret the first configuration as a strongly distorted precursor of the arrangement of rectangular cages encountered for intermediate and large values of z (cf. figure 6.11, (m), (q), (u) and figure 6.12, (b), (f), (j), and (n)).

For a particle size ratio of $z = 0.28$ and a concentration of $C = 1/7$, the two structures that were found to share the lowest free energy represent analogons to the minimum energy configurations obtained for $z = 0.2$ and $z = 0.3296$. In one structure (see figure 6.16, (b), left panel), the small particles do not distort their surrounding equilateral triangle of large particles like at the smaller particle size ratio of $z = 0.2$ (see figure 6.11, (i)). The small particles of the other structure (see figure 6.16, (b), right panel) sit at the centre of large rhombi and again form distinct lanes, thus being comparable to the arrangement found at $z = 0.3296$ (see figure 6.11, (q)).

The degenerate structures encountered at a concentration of $C = 2/3$ for particle size ratios of $z = 0.3296$ and $z = 0.41$ (see figure 6.16, (c) and (d)) forge a link between the distinct dimer configuration of small particles discovered at $z = 0.28$ (see figure 6.13, (p)) and the zig-zag shaped small-particle lanes that were found at $z = 0.5$ and $z = 0.6$ (see figure 6.14, (a) and (f)): at $z = 0.3296$, the formation of pairs with alternating orientation (figure 6.16, (c), left) is energetically as favourable as the strictly parallel orientation of the dimers (figure 6.16, (c), right): concomitantly, the hexagonal lattice formed by the large particles compensates for this alignment in the second case by a considerably stronger distortion. At $z = 0.41$, $C = 2/3$, structures displaying distinct four-particle aggregates (figure 6.16, (d), left) and zig-zag lanes of small particles (figure 6.16, (d), right) are of the same energy, once more illustrating the transition from aligned dimers (see figure 6.13, (p) and (u)) to zig-zag shaped lanes of small particles (see figure 6.13 (z) and figure 6.14 (a) and (f)).

Finally, the degenerate structures obtained for $z = 0.41$, $C = 4/5$ display the cross-over from the pearl-necklace configuration encountered at $z = 0.3296$ (cf. figure 6.13, (x)) and figure 6.16, (e), left) to the ring-like arrangements (figure 6.16, (e), right), which occur at higher particle size ratios (cf. figure 6.13, (cc) and figure 6.14, (d)). The formation of rings of small particles leads to a substantial modification of the lattice formed by the larger species, which changes from a rectangular structure to a hexagonal arrangement.

Pictures of the structures belonging to the second group of degenerate configurations are shown in figure 6.17. For a particle size ratio of $z = 0.1$ and a concentration $C = 1/2$, we find two configurations corresponding to the same minimal free energy. One structure shows stripes of small particles meandering through a hexagonal lattice formed by the larger one (see figure 6.17,

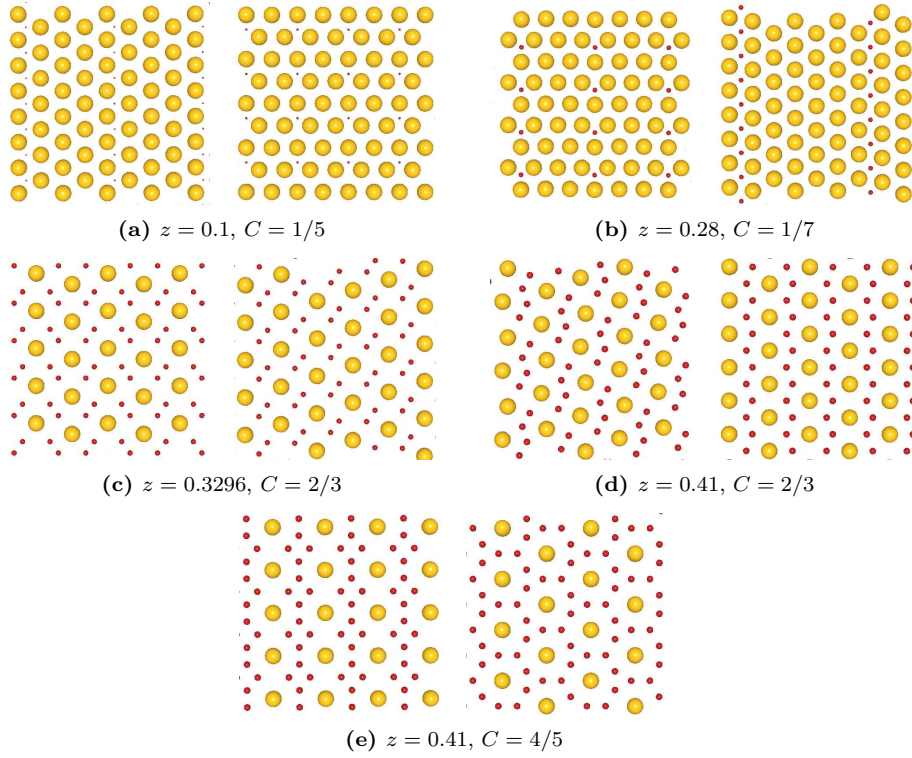


Figure 6.16: *Degenerate structures found for the dipolar mixture of particle belonging to group I (see text and table 6.2).*

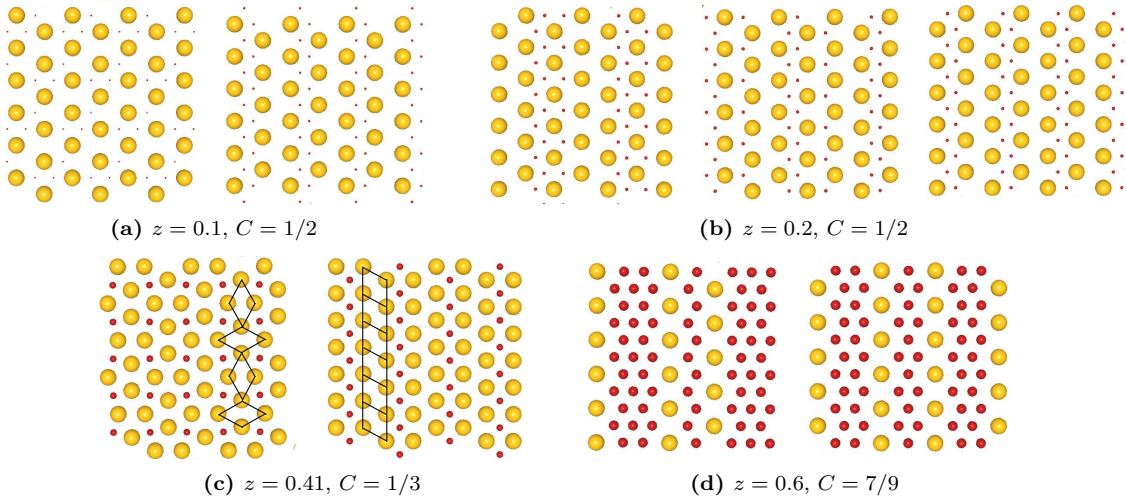


Figure 6.17: *Degenerate structures found for the dipolar mixture of particle size ratios $z = 0.1$ to $z = 0.6$ and concentrations $C = 1/2$ to $7/9$, belonging to group II (see text).*

(a), right panel), in the other, small particles arrange in groups of three particles, surrounding a large one in the form of a small arc (see figure 6.17, (a), left panel). Both configurations can be interpreted as variations of the same tiling, where the basic module consists of six equilateral triangles of large particles forming a hexagon. In both cases, three neighbouring triangles in each hexagon are decorated by a small particle in their centre. The emergence of the two different structures depends solely on the orientation of neighbouring hexagon-shaped tiles.

At the same concentration of small particles but for the slightly higher particle size ratio of $z = 0.2$, we encounter three energetically degenerate structures sharing the common feature of small particle lanes embedded in a hexagonal lattice of their larger counterparts. In the structure which was already included in the previous discussion in figure 6.11 (cf. section 6.2), neighbouring lanes of small particles are separated by a single stripe of undecorated rhombohedral unit cells (see figure 6.17, (b), right). In the other two configurations, the meandering stripes of small particles are farther apart, as two lanes of rhombohedral unit cells fit between the zig-zag-shaped stripes of small particles. Both of these structures also exhibit a single lane of isolated small particles in addition to the zig-zag-shaped lane; in one case, the isolated single lane is directly adjacent to the zig-zag-shaped arrangement, so that the impression of connected pentamers or cup-like structures emerge, which partially surround the large particles (see figure 6.17, (b), left panel), in the other case, the single stripe of isolated particles is distinctly separated from the zig-zag-shaped lane (see figure 6.17, (b), middle panel).

In the case of $z = 0.41$ and $C = 1/3$, both structures are built using the same two types of tiles: a square unit cell of large particles decorated with a small particle at its centre and an empty rhombohedral unit cell of large particles. In one structure, the rhombohedral unit cells are arranged parallel to each other, giving rise to a pattern of distinct alternating lanes of square and rhombohedral unit cells (see figure 6.17, (c), right panel. One of the rhombohedral lanes is emphasised in the picture.) The other structure can also be interpreted as an arrangement of alternating square and rhombohedral lanes, but in this case, the orientation of the tiles changes along the lanes, which obscures the pattern. Tiles belonging to one lane are of the same type and are connected via opposite corner points only (see figure 6.17, (c), left panel. One of the rhombohedral lanes is again highlighted in the picture.).

In the last case of degenerate structures discussed here, encountered for $z = 0.6$ and $C = 7/9$, the particles are again arranged in distinct lanes in the two configurations. The difference between the two degenerate structures lies with the width of the lanes consisting of small particles and the associated accommodation of these changes by the lattice of the large particles: In one case (see figure 6.17, (d), right panel), we observe double zig-zag-shaped lanes alternating with a pearl-necklace-like configuration of small particles. In the other case (see figure 6.17, (d), left panel), the small particle arrange in a sequence of single zig-zag-lanes and lanes of interconnected hexagons.

Summarising, the occurrence of degenerate tilings is observed in five of the in total nine cases of energetically degenerate structures, namely in the structures shown in figure 6.16, (a) and (b), and in figure 6.17, (a), (b), and (c). We interpret this repeated appearance of differently tiled phases that correspond to the same minimal free energy as a strong indication that the random tiling phases mentioned in reference [94] might be observed at those state points.

6.2.2 Comparison to simulations and experiments

We have chosen to investigate this binary mixture of dipolar colloids because of its realisability in experiments. As stated in section 2.2, there exist two different experimental setups for our model system: in system I, polystyrene particles are used, which float at an oil-water interface to ensure the two-dimensional geometry of the setup. The particles are of two different sizes and interact via an induced, effective dipole-dipole potential (cf. equations (2.4) to (2.6)) [40–42, 53]. System II consists of super-paramagnetic colloids, interacting via an ideal dipole-dipole potential, as an external magnetic field is employed to induce dipole moments perpendicular to the plane of the monolayer in the particles (see equation (2.8)). Like in system I, the particles are confined to an interface by gravity in order to provide their arrangement in monolayers. This time the interface is given by the surface of a pending water droplet [43–47]. In section 2.2, we have shown that these two systems are equivalent if the average spacing between particles is sufficiently large, i.e. if the particle area density is sufficiently low.

We compare the minimum energy configurations identified with the GA for system I to molecular dynamics simulations of this system [42] and to experimental data obtained from a realisation of system II [47, 95].

Comparison to molecular dynamics simulations

We start our discussion by comparing our results presented in the previous section to the structures obtained by T. Stirner and J. Sun for system I [42]. These authors employed molecular dynamics simulations (abbreviated "MD simulation") to determine the configuration corresponding to the global energy minimum, mimicking in detail the experimental setup of system I as it is described above. They investigated the system at different concentrations of small particles, namely $C = 2/3$, $C = 6/7$ and $C = 7/8$. As we did not include systems with a concentration of $C = 7/8$ in our survey, we will not discuss this case in the following.

In the simulations study [42], the particle size ratio z was fixed to $z = 0.32963$, as the diameters of the two particle species were restricted to the two values readily available to experimentalists, $\sigma_A = 2.7 \mu\text{m}$ and $\sigma_B = 0.89 \mu\text{m}$. Instead of changing the particle size ratio, Stirner and Sun investigated two different interaction regimes: a so-called strong interaction regime, where the exponent n in the interaction potentials given in (2.4)-(2.6) was set to $n = 3$, and a so-called weak interaction regime with $n = 2$, where the dipole moment of each particle scales with its surface area. Furthermore, the average distance between large particles was fixed to $d_A = 6 \mu\text{m} \approx 2.2\sigma_A$,

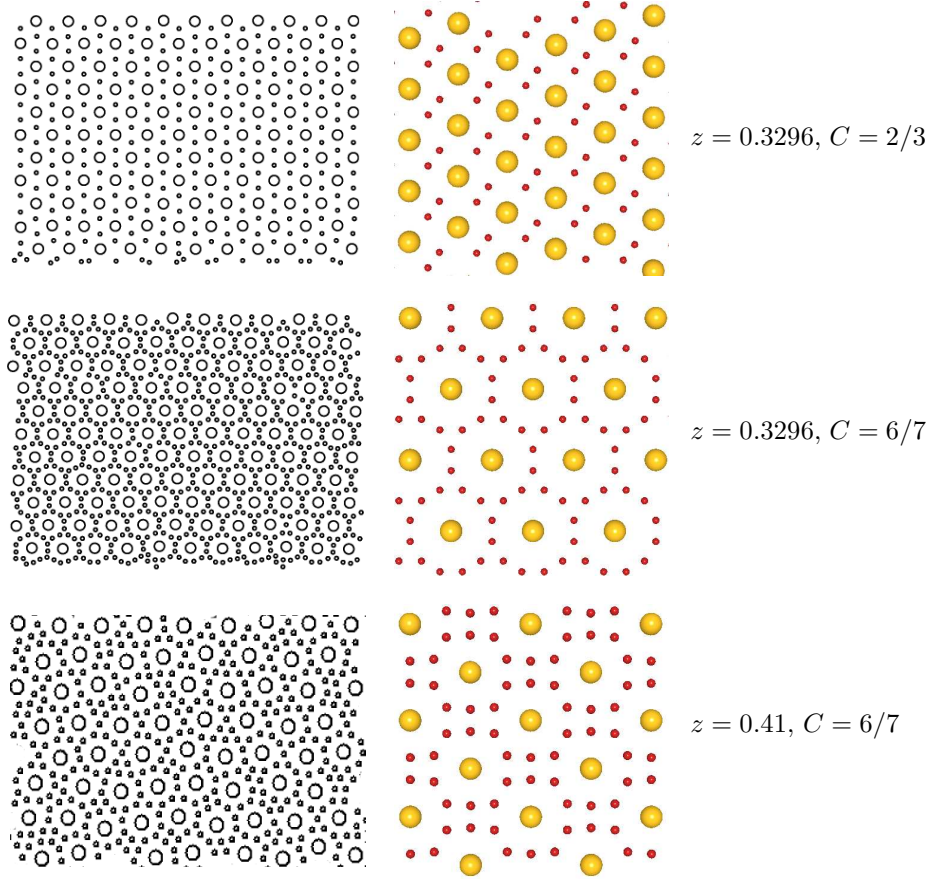


Figure 6.18: *Comparison of results obtained for a binary mixture of colloids interacting via an effective dipole-dipole interaction. The pictures were obtained for different particle size ratios and concentrations as indicated. Structures in the left column were found in molecular dynamics simulations (pictures were taken from reference [42]), those in the right column were identified using the GA-based search technique.*

irrespective of the concentration of small particles in the system. For $C = 2/3$, an average distance between large particles of $d_A = 2.2\sigma$ corresponds to an overall, dimensionless particle area density of $\eta\sigma_A^2 \approx 0.70$, whereas for $C = 6/7$, this value changes to $\eta\sigma_A^2 \approx 1.64$.

In the case of the strong interaction regime characterised by $n = 3$, we find good overall agreement between the structures found to be stable in simulations and those identified as minimum energy configurations by the GA: for $C = 2/3$, the GA and the simulations find large particles occupying an ideal hexagonal arrangement, where each equilateral triangle of this lattice has a small particle at its centre (see figure 6.18, top row). At $C = 6/7$, the MD simulations reveal a configuration where the large particles again form a hexagonal pattern, but each equilateral triangle of large particles is occupied by an inverted triangle of small particles. Thus, ring-like arrangements of twelve small particles are formed around each large one – a configurations that coincides well with the structure obtained with the GA (see figure 6.18, middle row).

As mentioned above, Stirner and Sun also provide results for their so-termed weak interaction

regime in [42]. Since they claim that no changes in the found structures occur if varying the particle coverage – and thus the particle area density – in their simulations, we are safe to assume that the simulations operate in the "ideal dipole limit" and relation (2.9) holds true to "translate" between the two interaction regimes, $n = 2$ and $n = 3$. Thus, simulations conducted for $z = 0.3296$ and $n = 2$ correspond to $z = 0.41$ in the strong interaction regime and comparisons to our findings presented in figures 6.11 to 6.14 are possible. For the weak interaction regime ($n = 2$), Stirner and Sun only provide us with structures obtained at concentrations $C = 6/7$ and $C = 7/8$, and as stated above, we exclude the latter from the following discussion. For $C = 6/7$, the simulations show a largely disordered structure as the minimum energy configuration in contrast to the well ordered structure identified with the GA (see figure 6.18, bottom row). We believe this to have several reasons: first, disordered structures are inaccessible to the applied GA-based search method. Second, the MD simulations were performed at finite temperature in contrast to our technique, which operates at $T = 0$. Even if the ratio of potential to kinetic energy was quite large in the simulations, $F/(Nk_B T) = 5 \cdot 10^2$ [42], the temperature applied to the system could already be high enough to "melt" the ordered equilibrium structure proposed by the GA for $T = 0$. This might even more be the case, since the much weaker interacting small particles are supposed to enter the liquid state at lower temperatures than their large counterparts. Yet another reason for the disagreement could stem from the starting configuration used in the simulation, which puts a bias on patterns with a homogeneous distribution of small particles: each simulation was started from a configuration with 121 large particles arranged on an ideal hexagonal lattice and the appropriate number of small particles distributed evenly inbetween. It is probable that the employment of such a starting configurations hinders the emergence of a structure with an anisotropic distribution of small particles, like the one identified with the GA and shown in figure 6.18.

Comparison to experimental data

Besides the MD simulations of T. Stirner and J. Sun, we also compare the results presented in section 6.2.1 to experimental data provided by F. Ebert et al. for system II [47, 95]. They investigated a binary mixture of super-paramagnetic colloids for different values of the system temperature in order to study its vitrification. The formation of locally ordered structures or *crystallites* was observed despite the globally disordered state of the system. These crystallites are believed to have their origin in the non-additivity of the interaction potential and the consequential partial clustering of the small particles in the system [54, 96]. The locally ordered regions are known to play a major role in the glass transition as their occurrence hinders the emergence of long range order in the system [97]. It is the structure of these stable crystal grains that we compare our findings to in the following.

The magnetisation ratio of the super-paramagnetic particles in use in the experiments was $m = \chi_B/\chi_A \approx 0.1$, where χ_i is the susceptibility of species i . This value of the magnetisation ratio corresponds to a particle size ratio of approximately $z = 0.398$ at $n = 3$ in the description

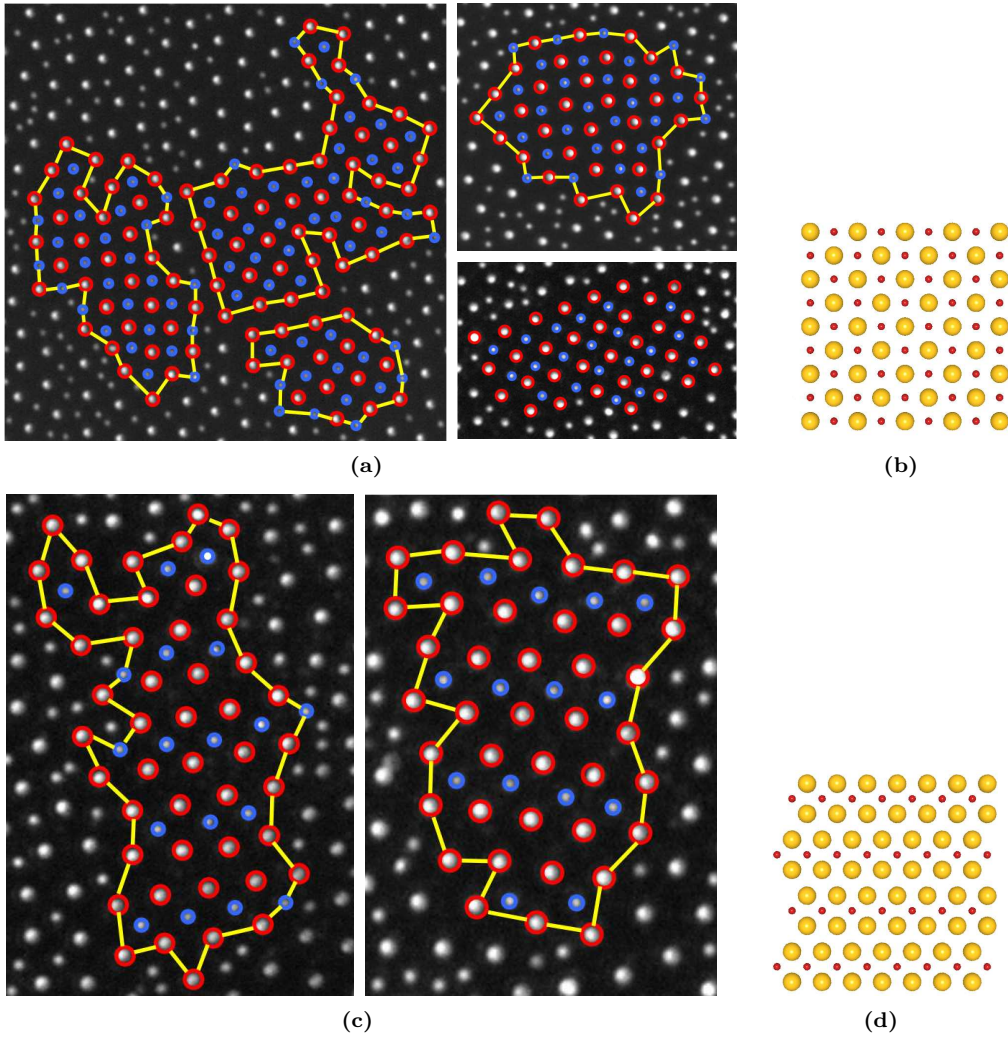


Figure 6.19: Comparison of stable crystallites found in experiments (a,c) to the GA-identified structure (b,d) at the corresponding values of $z = 0.41$ and the matching concentrations, $C = 1/2$ (top row) and $C = 1/3$ (bottom row). (Snapshots from experiments by courtesy of F. Ebert.)

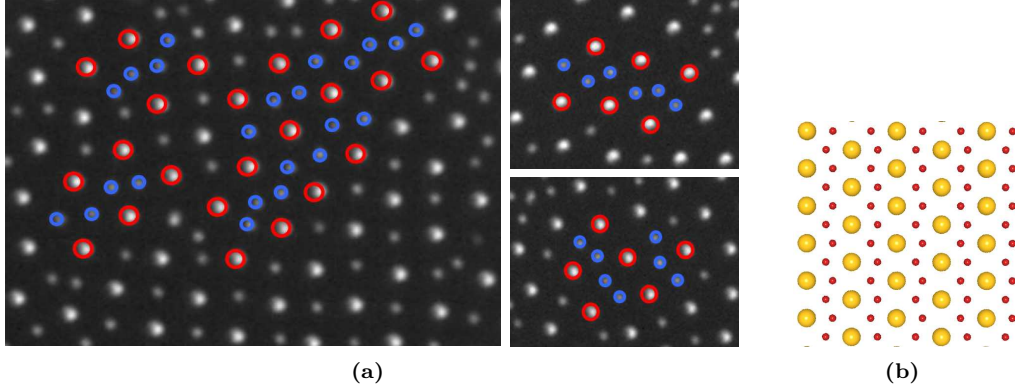


Figure 6.20: *Comparison of (a) stable crystallites found in experiments to (b) the GA-identified structure at the corresponding values of $z = 0.41$ and $C = 2/3$. (Snapshots from experiments by courtesy of F. Ebert.)*

of system I (cf. relation (2.9)). The percentage of small particles in the system varied between 29% to 45%. Video microscopy and standard image processing were utilised in the experiment to analyse the behaviour of the system [47]. The dimensionless interaction strength

$$\Gamma = \frac{E_{\text{magn.}}(\mathbf{B})}{Nk_bT} \quad ,$$

representing the inverse temperature of the system, was controlled via the strength of the external magnetic field \mathbf{B} and set to values between $\Gamma \approx 220$ and $\Gamma \approx 554$ [47].

Ebert et al. report two patterns to be predominant in their samples, irrespective of the overall concentration of small particles in the system: first, a hexagonal structure consisting of large particles only, and, second, the arrangement of large particles into squares, with a small particle at the centre. The individual crystallites exhibit either a hexagonal lattice formed by the large species only, a square structure, or an alternating composition of hexagonal and square unit cells, so that the local concentration of small particles in the crystal grains is either $C = 0$ for the hexagonal lattice of large particles, $C = 1/2$ for the square arrangement or $C = 1/3$ for the alternating configuration. Besides crystallites consisting of the two unit cells described above, zig-zag shaped lanes of small particles occur in the sample. Although these small particle chains are mostly rather short – usually four to eight small particles form a chain – they represent a distinct feature of the system. Despite the partial clustering, no other crystal grains consisting predominantly of small particles occur in the sample, as regions with a large majority of small particles are unlikely to form, due to the overall concentration of small particles C being well below $1/2$ in all experiments.

The particle size ratio which was investigated with the GA and most closely corresponds to the magnetisation ratio used in the experiments, is $z = 0.41$. When comparing the experimental data to the configurations identified by the GA for $z = 0.41$, we find good overall agreement in the structures found to be stable. The predominance of the two patterns – a hexagonal lattice

of large particles only and the square configuration with the small particle at its centre – and its independence from the overall concentration of small particles in the sample is generally in accord with the results obtained with the GA-based search technique, as all configurations identified with the GA which are of a concentration $C \leq 1/2$ consist of these two types of cells (cf. figure 6.11). Furthermore, each structure found in the individual stable crystallites corresponds to a minimum energy configuration identified with the GA: the square lattice, with the small particles sitting at the centre of each square was found for $C = 1/2$, the alternating sequence of hexagonal and square unit cells was identified for $C = 1/3$ (see figure 6.19), and the hexagonal structure is known to be the minimum energy configuration of a one component system, whose constituent particles interact via a dipole-dipole interaction [53]. Also the zig-zag chains of small particles have their representation in a minimum energy configuration obtained with the GA, as they closely resemble the structure the GA predicts to be stable for $C = 2/3$ (see figure 6.20).

6.2.3 Phonon band structures

Phonon band structures of colloidal dispersions have received intensive interest currently, especially in regard to the tuneability of the dispersion curves and the associated possibility of designing the elastic properties of a material [80, 90, 98–100]. In this section, we focus on the phonon band structures of the binary mixture of dipolar colloids and study the influence of the system parameters on the layout of the dispersion curves.

Under the assumption that the average particle separation is large enough to allow for describing the interaction by an ideal dipole-dipole potential, the following three parameters affect the phonon band structure: the susceptibility ratio $m = \chi_B/\chi_A$ and the concentration of small particles C control the ground state of the system and thus have major influence on the dispersion curves. The mass ratio $M = M_B/M_A$ of the two particle species involved is the third crucial parameter in this context, as two systems with identical minimum energy configurations but different mass ratios exhibit different phonon band structures (cf. section 5.1.2).

With future applications in mind, we restrict our investigations to those values of the susceptibility ratio and concentration that correspond to ground states verified in experiments, $m \approx 0.108$ and $C = 1/3, 1/2$, and $2/3$. Besides the value known from experiments [47], we investigate the phonon spectra at two other values of the mass ratio M , which reflect the two general methods to prepare magnetic colloidal particles [101]:

- $M \approx 0.2409$, the value known from experiments.
- $M \sim m$, corresponding to magnetic colloids produced via *encapsulation*: paramagnetic nano particles are incorporated into the growing colloid, yielding susceptibilities χ_A and χ_B proportional to the volume of the particle, i. e. $\chi_i \sim R_i^3$, where R_i denotes the radius of a particle of species i . Since the mass of each particle also directly relates to its volume,

$M_i \sim R_i^3$, it is justified to assume that the mass ratio M is proportional to the susceptibility ratio, i. e. $M \sim m$ in this case.

- $M \sim m^{3/2}$, which relates to super-paramagnetic colloids produced via coating processes: the magnetic component is contained in a layer on the particle's surface, so that the susceptibility χ_i of a colloid of species i scales with its surface area, $\chi_i \sim R_i^2$. As the mass is proportional to the volume of the particle, we obtain $M \sim m^{3/2}$ as the relation between mass ratio M and the susceptibility ratio m .

Figures 6.21, 6.22, and 6.23 contain the band structures $\omega_*^2(q)$ of the stable particle arrangements identified at $m \approx 0.107$ and $C = 1/3, 1/2$, and $2/3$ for decreasing values of the mass ratio, (a) $M = 0.2409$, (b) $M \sim m = 0.107$, (c) and $M \sim m^{3/2} \approx 0.035$. The respective minimum energy configurations are also depicted in the figures (see figures 6.21 to 6.23, (d)) together with their corresponding reciprocal lattices (see figures 6.21 to 6.23, (e)). The paths along which the phonon band structures are calculated encircle the irreducible sections of the respective first Brillouin zones (cf. section 5.1.2), and are marked in the pictures of the reciprocal lattices. Reduced units are used throughout the entire discussion, so that the dispersion curves $\omega_*^2(\mathbf{q})$ correspond to the frequencies $\omega(\mathbf{q})$ via $\omega_*^2(\mathbf{q}) = \omega^2(\mathbf{q})\sigma_A^2 M_A/\varepsilon_{II}$, where ε_{II} is the energy scale of the system and σ_A corresponds to the diameter of the larger particle species (cf. section 2.2).

In every band structure, we observe $2n_p$ individual branches, where n_p is the number of particles in the chosen unit cell. Two of these bands are acoustic, $2(n_p - 1)$ are optical branches. We start our discussion of the phonon band structures with the results obtained for a susceptibility ratio of $m \approx 0.107$ and a concentration of small particles $C = 1/3$ (see figure 6.21). At a mass ratio of $M \approx 0.2409$, the in total six branches of the band structure are distributed evenly over a small frequency range, from $\omega_*^2 = 0$ to a maximum value of $\omega_*^2 \approx 6.8$. Decreasing the mass ratio to $M \approx 0.107$ widens the frequency range covered by the band structure, as frequencies up to $\omega_*^2 \approx 11.0$ are reached by the topmost branches. The two topmost dispersion curves also detach from the rest of the spectrum, thus giving rise to a distinct gap in the band structure and yielding the system "opaque" to vibrations of frequencies in the range of $\omega_*^2 \approx 5.7$ to 9.4 . An additional effect of the decrease in the mass ratio is observed in the flattening of the detached optical branches, leaving the frequencies of the corresponding normal modes more insensitive to changes in the wave vector \mathbf{q} . Further enhancing the asymmetry in the mass of the two involved particle species to $M \approx 0.035$ considerably widens the observed gap – from $\omega_*^2 \approx 5.7$ to 27.4 – and even higher frequencies are covered by the phonon spectrum, the maximum value being $\omega_*^2 \approx 29.5$. In addition, the topmost two optical branches that decouple from the rest of the band structure appear again considerably flattened as the mass ratio is further decreased.

The dispersion curves obtained for $m \approx 0.107$ and $C = 1/2$ in general follow the trends observed for the previous system (see figure 6.22): at $M \approx 0.2409$, the phonon band structure consisting of four branches is rather compact with a maximum frequency value of $\omega_*^2 \approx 4.3$ and no gaps occur

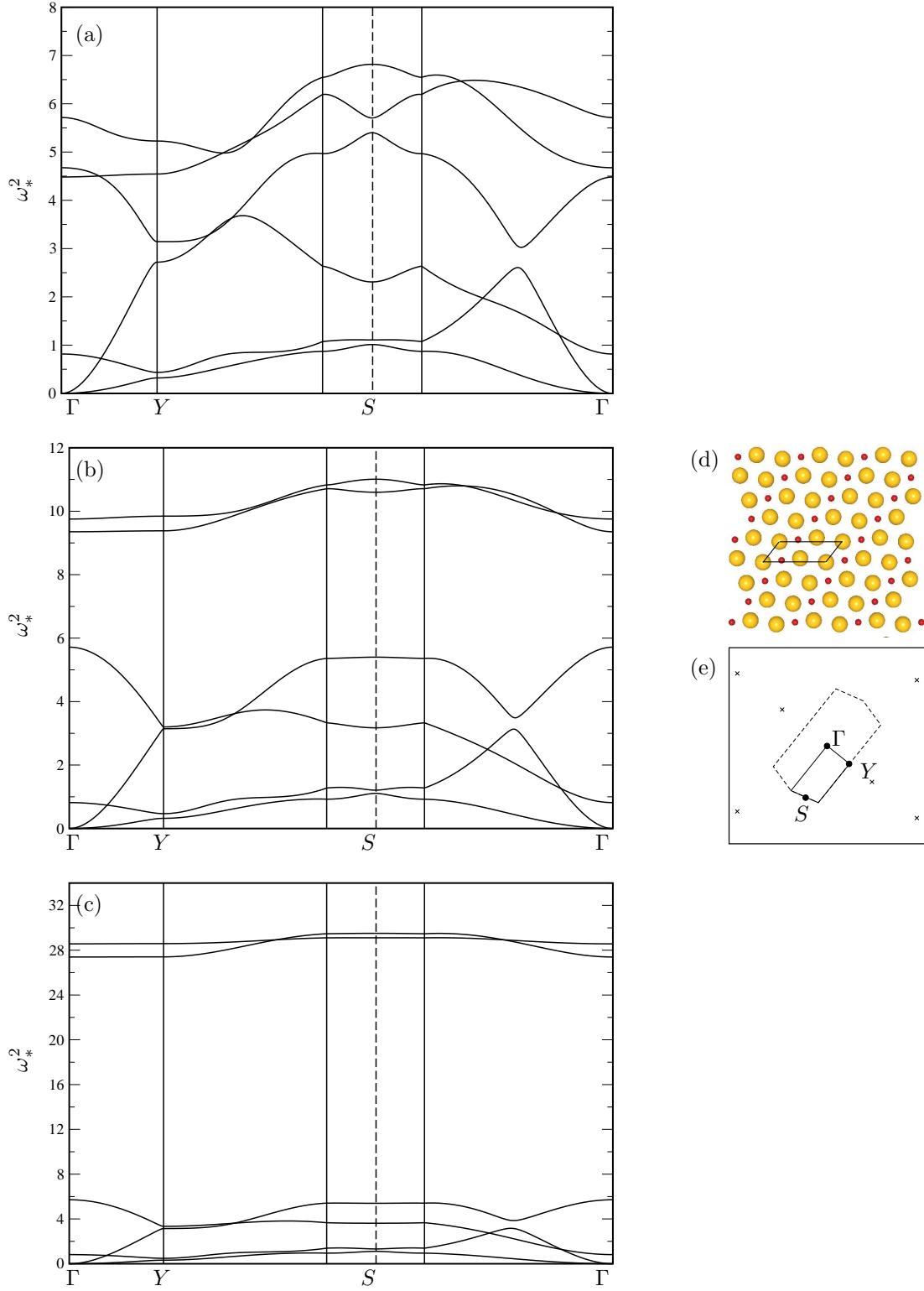


Figure 6.21: Phonon spectra obtained for the binary mixture of dipolar colloids for $m \approx 0.107$ and $C = 1/3$ at three values of the mass ratio, (a) $M = 0.24$, (b) $M \sim m \approx 0.107$, and (c) $M \sim m^{3/2} \approx 0.035$. The two small pictures show (d) the stable particle arrangement with the chosen unit cell (full line), and (e) the corresponding reciprocal lattice with the first Brillouin zone (dashed line) and the path along which the band structures were calculated (full line).

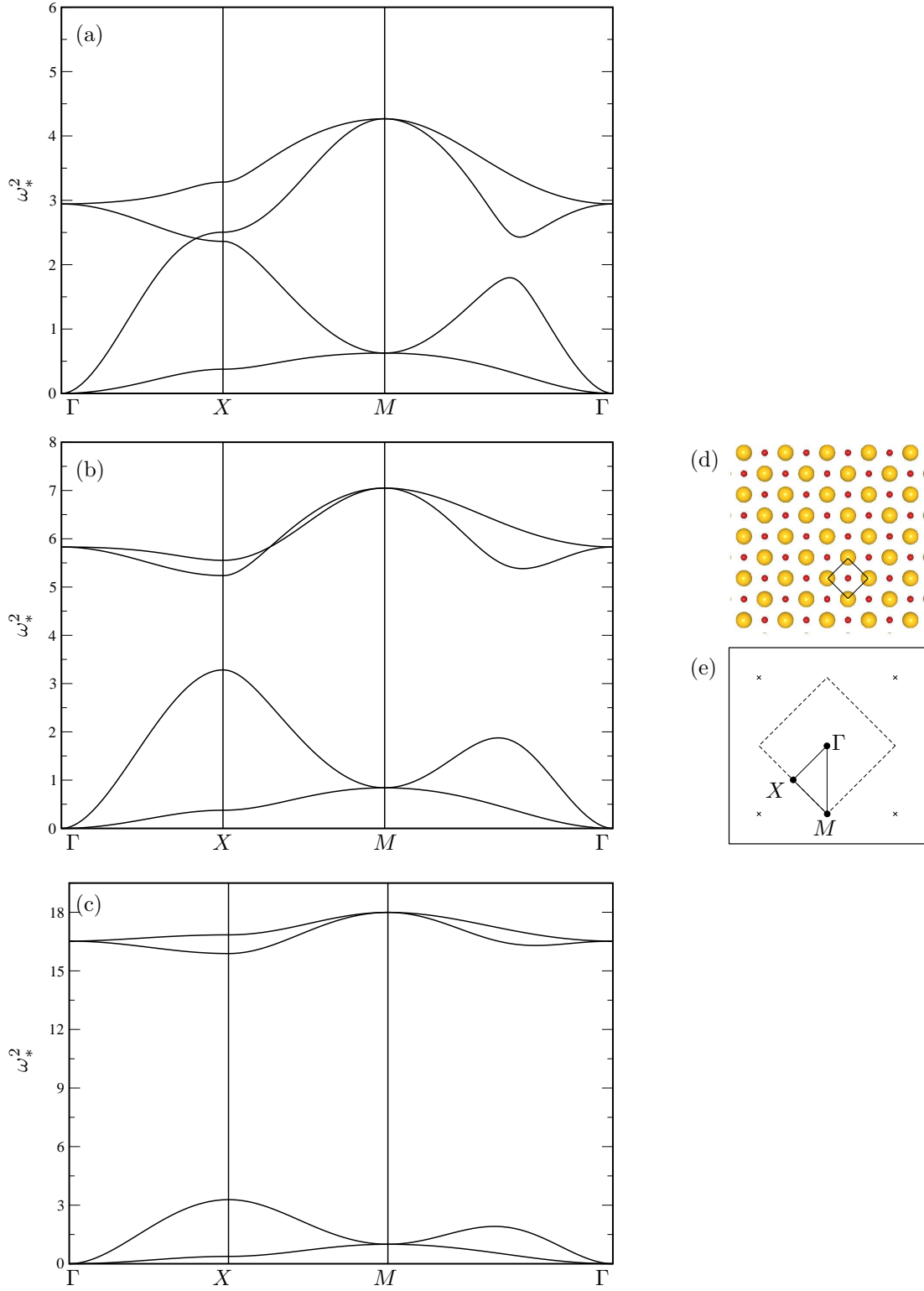


Figure 6.22: Phonon spectra obtained for the binary mixture of dipolar colloids for $m \approx 0.107$ and $C = 1/2$ at three values of the mass ratio, (a) $M = 0.24$, (b) $M \sim m \approx 0.107$, and (c) $M \sim m^{3/2} \approx 0.035$. The small pictures show (d) the stable particle arrangement with the chosen unit cell (full line), and (e) the corresponding reciprocal lattice with the first Brillouin zone (dashed line) and the path along which the band structures were calculated (full line).

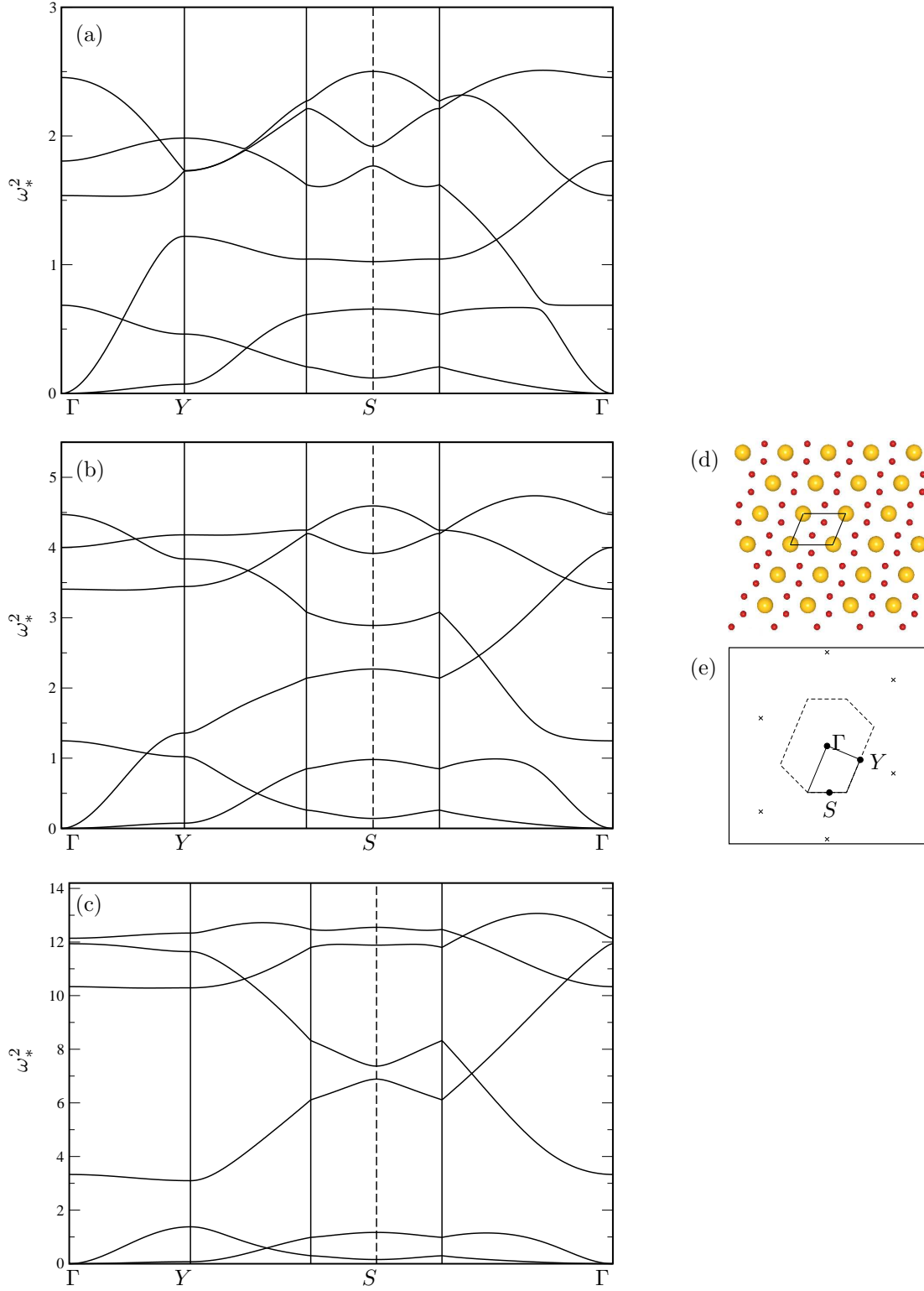


Figure 6.23: Phonon spectra obtained for the binary mixture of dipolar colloids for $m \approx 0.107$ and $C = 2/3$ at three values of the mass ratio, (a) $M = 0.24$, (b) $M \sim m \approx 0.107$, and (c) $M \sim m^{3/2} \approx 0.035$. The small pictures show (d) the stable particle arrangement with the chosen unit cell (full line), and (e) the corresponding reciprocal lattice with the first Brillouin zone (dashed line) and the path along which the band structures were calculated (full line).

in the spectrum. Lowering the mass ratio to $M \approx 0.107$ again opens a distinct gap in the band structure (see figure 6.22, (b)), as the two optical branches decouple from the acoustic bands and no normal modes exist that can pick up vibrations with frequencies between $\omega_*^2 \approx 3.3$ and 5.2. The topmost branch reaches a maximal frequency of $\omega_*^2 \approx 7.0$. A further decrease in the mass ratio to $M \approx 0.035$ widens the gap even more as the optical branches move to higher frequencies, the maximal value being $\omega_*^2 \approx 18.0$. The gap thus encompasses all frequencies in the range from $\omega_*^2 \approx 3.3$ to 15.9. Also in the case of $C = 1/2$, the optical branches appear less modulated as the mass ratio decreases.

At $m \approx 0.107$ and $C = 2/3$, the phonon band structures consist of six branches and exhibit a small variation of the trends observed so far (see figure 6.23): the first band structure, determined for $M \approx 0.2409$ and shown in figure 6.23 (a) is again the most compact structure overall, as it only covers frequencies from $\omega_*^2 = 0$ to $\omega_*^2 \approx 2.5$. The frequency range broadens with a decrease of the mass ratio, first to $\omega_*^2 \approx 4.7$ at $M \approx 0.107$, and then to $\omega_*^2 \approx 13.0$ at $M \approx 0.035$. A relatively small gap is only observed in the case of $M \approx 0.035$, where all four optical branches detach from the rest of the band structure, leaving frequencies from $\omega_*^2 \approx 1.4$ to 3.1 uncovered by the dispersion curves, so that the gap is located at relatively low frequencies, compared to the corresponding band structures determined for $C = 1/3$ and $C = 1/2$. We also observe the optical branches to be less flat than in the previous two cases.

Although not observed in experiments, we include the particle arrangement found for $m \approx 0.018$ and $C = 5/7$ into our discussion, as its phonon band structure exhibits the above mentioned features in a particularly pronounced fashion (see figure 6.24): the dispersion curves comprise a number of isolated, almost completely flat branches that give rise to seven gaps of considerable size. As the mass asymmetry is already very strong in the two investigated cases, $M \sim m \approx 0.018$ (figure 6.24, left panel, top) and $M \sim m^{3/2} \approx 0.0024$ (figure 6.24, left panel, bottom), the same band structure is observed for both values of the particle mass ratio.

In summary, we believe the susceptibility ratio m and the concentration of small particles C to have distinct influence on the overall appearance of the phonon band structures as the ground state of the system is defined by these two parameters. The positioning and number of eventual gaps seems to be connected to the number of small particles, n_B , and thus to the value of C , as the observed gaps in the phonon band structure are formed by $2n_B$ optical branches decoupling from the rest of the band structure in all investigated cases.

The mass ratio M on the other hand affects the frequency range covered by the dispersion curves, as an increasing asymmetry in the mass of the two particle species is observed to lead to higher maximal frequencies in the phonon spectra. However, this influence on the frequency seems to be non-uniform, since gaps in the phonon band structure open and close upon changes in the mass ratio. Furthermore, the value of M is found to have an effect on the modulation of the optical branches, yielding almost completely flat bands at small values of M .

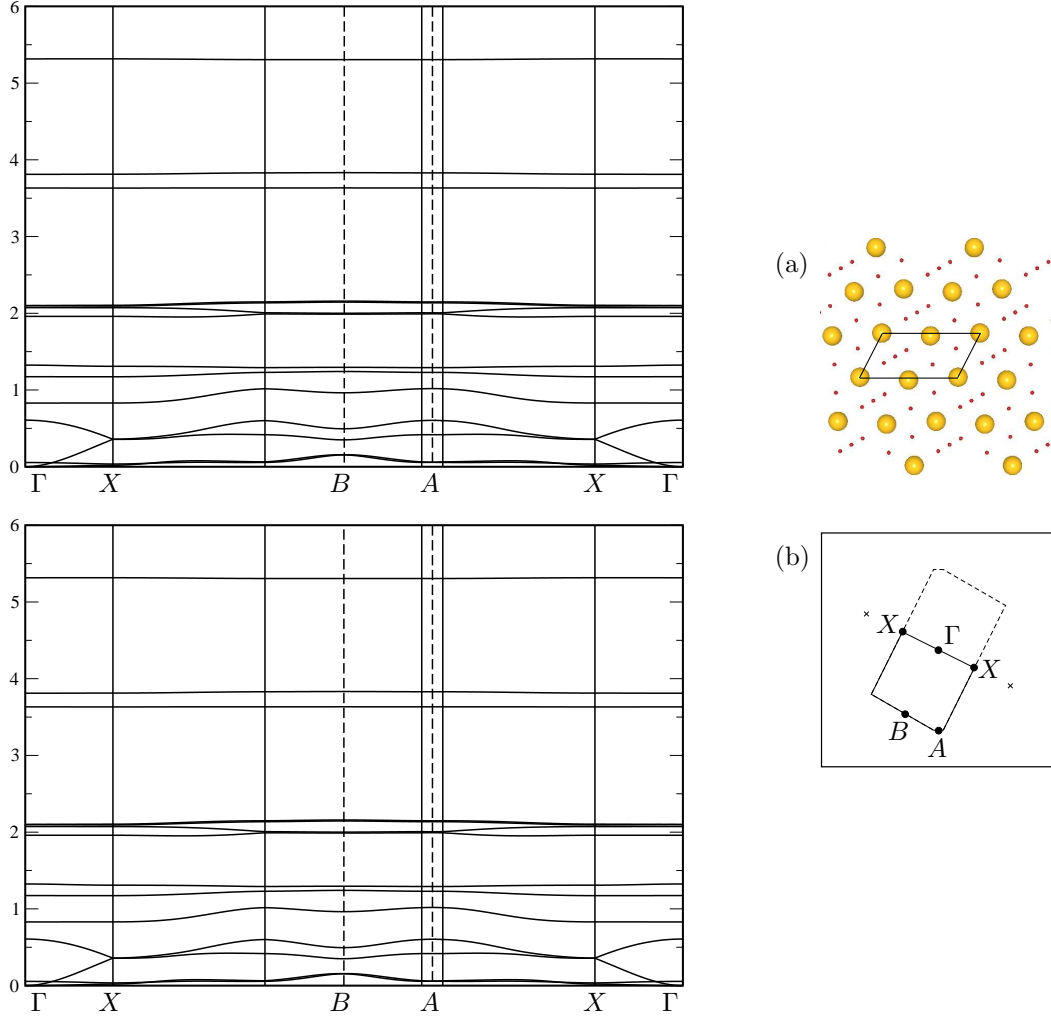


Figure 6.24: Phonon band structures (left panels) obtained for the binary mixture of dipolar colloids at $m \approx 0.018$ and $C = 5/7$, for two values of the particle mass ratio, $M \sim m$ (top) and $M \sim m^{3/2} \approx 0.0024$ (bottom). The small pictures show (a) the particle arrangement with the chosen unit cell marked by a full line and (b) the corresponding first Brillouin zone (dashed line) with the path along which the dispersion curves were calculated (full line). The points of special symmetry are also marked in panel (b).

6.3 Quasi-planar dipolar colloids

A one-component system of dipolar particles confined to a planar cell of variable thickness is the centre of our attention in this section. The impenetrable particles interact via a dipole-dipole potential, which is either purely repulsive, softened repulsive or attractive at short distances, depending on the cell thickness D (see section 2.3). By employing our optimisation technique based on genetic algorithms, we study the equilibrium structures of this system at the cross-over from two to three dimensions by varying the particle density for a number of different values of D . After presenting the configurations identified by the genetic algorithm, we set our investigations in a larger context by comparing the results to data obtained in experiments and Monte Carlo simulations.

6.3.1 Ordered equilibrium structures

We analyse the system's strategies to arrange particles in the energetically most favourable pattern for varying particle volume density $\rho\sigma^3$ and six different values of the cell thickness, $D = \sigma + h = 1.2\sigma, 1.445\sigma, 1.55\sigma, 1.6\sigma, 1.8\sigma$, and 2σ , with σ denoting the hard-core diameter of the particles and h being the maximal vertical displacement between two particles in the system. The investigated density region ranges from $\rho\sigma^3 = 0.5$ to $\rho\sigma^3 = 2.0$, with a step size of $\Delta\rho\sigma^3 \approx 0.08$. As all calculations are performed in an NVT -ensemble, the equilibrium structure at a given value of the particle volume density corresponds to a global minimum in the Helmholtz free energy.

The six different values of the cell thickness that were investigated cover all interaction regimes discussed in section 2.3: $D = 1.2\sigma$ and 1.445σ correspond to the purely repulsive regime of the interparticle potential; in the case of $D = 1.2\sigma$, the interaction still closely resembles the potential known from two-dimensional dipole-dipole interactions, whereas at $D = 1.445\sigma$ we are close to the cross-over to the regime of relative attraction. At a cell thickness of $D = 1.55\sigma$, the potential has a region of relative attraction adjacent to the impenetrable hard core of the particle, and at $D = 1.6\sigma$ and 1.8σ , the cell is wide enough to allow for an attractive interaction between particles at close distances. At the sixth investigated cell thickness, $D = 2\sigma$, two colloidal particles are able to arrange on top of each other, resembling the formation of lanes parallel to the external field, a behaviour well known from three dimensional systems of dipolar particles (cf. section 2.3).

The investigation on the minimum energy configurations of the quasi-planar system is performed in two steps: first, we use a parameterisation that includes the vertical displacements z_i of all n_p particles in the unit cell as parameters to optimise, in order to determine the vertical arrangement of the particles (cf. section 4.2.1.6). These preliminary calculations showed that all particles keep to either the very top or bottom of the cell without any particles populating intermediate vertical positions, i. e. $z_i = 0$ or h for all $i = 1, \dots, n_p$. Knowing about this particular vertical

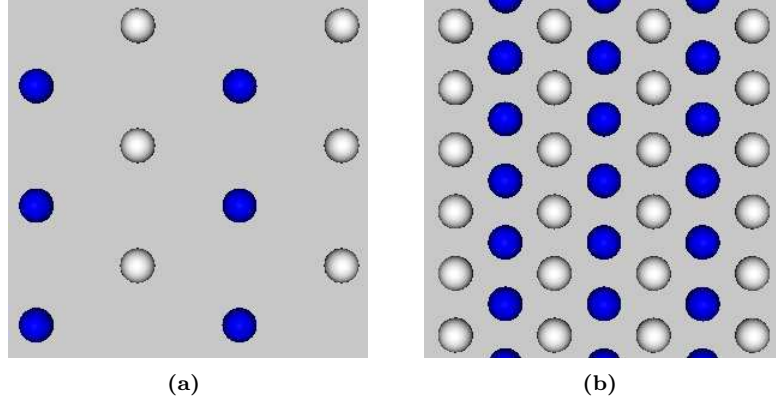


Figure 6.25: *Minimum energy configurations of a quasi-planar system of dipolar colloids at a cell thickness of $D = 1.2\sigma$ and two particle volume densities, (a) $\rho\sigma^3 = 0.5$ and (b) $\rho\sigma^3 = 2.0$. The different vertical positions of the particles are colour-coded: blue particles are located at the bottom of the cell, white particles at the top.*

distribution, we decide to employ the more efficient layer parametrisation in the second step of the investigation, where each structure is described as a stacking of n_l identical two-dimensional layers (see section 4.2.1.6). We considered systems of up to four layers, i. e. $n_l = 4$, and the distance between the outermost two of these layers was fixed to the maximal displacement h . In addition, we limit the number of particles per unit cell to $n_p = 6$ in each layer, with an exception for systems with a cell thickness of $D = 1.445\sigma$, where the maximum number of particles in the unit cell of a two-dimensional layer is set to $n_p = 8$.

In an effort to check the convergence and reliability of our algorithm, ten to forty independent runs are performed for every state point; the actual number of runs depends on the number of parameters to optimise. The Helmholtz free energies of the structures obtained in these independent implementations of the GA are then compared in a second step to determine the final configuration of minimal energy for the given state point (cf. the procedure employed in the investigations of the binary mixture of dipolar colloids in section 6.2). Due to the long range nature of the interaction potential (2.10), we have extended the lattice sums to distances as large as 500 times the particle diameter in each of the independently performed calculations.

Among the six values of the cell thickness that were investigated, we identify two limiting cases, for which no structural change is observed in the entire density range: the first, where $D = 1.2\sigma$, closely resembles the two-dimensional setup since the particles can vertically deviate from the plane only to a small extent. The particles at the top and at the bottom of the cell arrange in two rectangular structures which are mutually displaced, leading to an almost ideal hexagonal lattice in top view (see figure 6.25), as was to be expected for a quasi-planar system that close to the two-dimensional case. In the second limiting case, $D = 2\sigma$, the cell is wide enough to allow for two particles to arrange on top of each other. These vertical dimers arrange on the sites of an ideal hexagonal lattice (see figure 6.26). In terms of stacked layers, the identified structure consists of

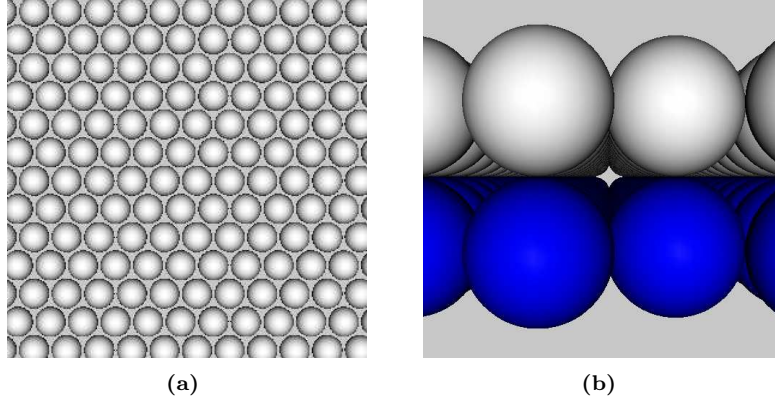


Figure 6.26: *Minimum energy configuration of a quasi-planar system of dipolar colloids at a cell thickness of $D = 2.0\sigma$ and a particle volume density of $\rho\sigma^3 = 2.0$. Picture (a) shows the structure in top view, picture (b) the same structure in side view. The different vertical positions of the particles are colour-coded: blue particles are located at the bottom of the cell, white particles at the top.*

two congruent hexagonal lattices with coinciding origins, placed at the top and bottom of the cell, respectively.

For all other values of the cell thickness, the obtained sequences of minimum energy configurations consist of a number of different structures. We start our discussion with the arrangements found to be stable for a cell thickness of $D = 1.445\sigma$; examples of the obtained configurations for increasing density are shown in figure 6.27. The configurations at the low end of the investigated density range can be viewed as a centred rectangular lattice, where the particles at the centre and at the corners of each rectangle populate opposite vertical positions (see figure 6.27, (a)). As the density increases, the centred rectangular lattice deforms to a square structure with the same vertical positioning of particles as in the preceding case (see figure 6.27, (b)). The square lattice is observed to be stable in the comparatively large density range from $\rho\sigma^3 = 0.583$ to $\rho\sigma^3 = 1.116$. Further increase of the density leads the system to change its strategy to arrange particles and formation of pairs – one particle in the pair located at the bottom of the cell and one at the top – is identified as the energetically favoured configuration (see figure 6.27, (c)). The particles at the bottom of the cell form a centred rectangular lattice as do their counterparts in the top layer where the sub-lattice is displaced along the direction of the smaller edge of the rectangle. The arrangement of particles to dimers is observed in the density range from $\rho\sigma^3 = 1.25$ to $\rho\sigma^3 = 1.417$. We interpret this occurrence of dimers as a precursor to the lane-like configuration that is found to be stable from $\rho\sigma^3 = 1.5$ onwards, where particles at the top and bottom positions alternate along the lane. Neighbouring lanes are out of registry by one effective particle diameter σ_e (see figure 6.27, (d)), so that in a top view, the structure resembles a square lattice which is compressed along one lattice vector and stretched in the direction of the other as far as possible. If we alternatively describe this structure as an arrangement of stacked layers, the lanes are built by two layers of a centred rectangular lattice, which are shifted by an effective particle diameter σ_e along the shorter

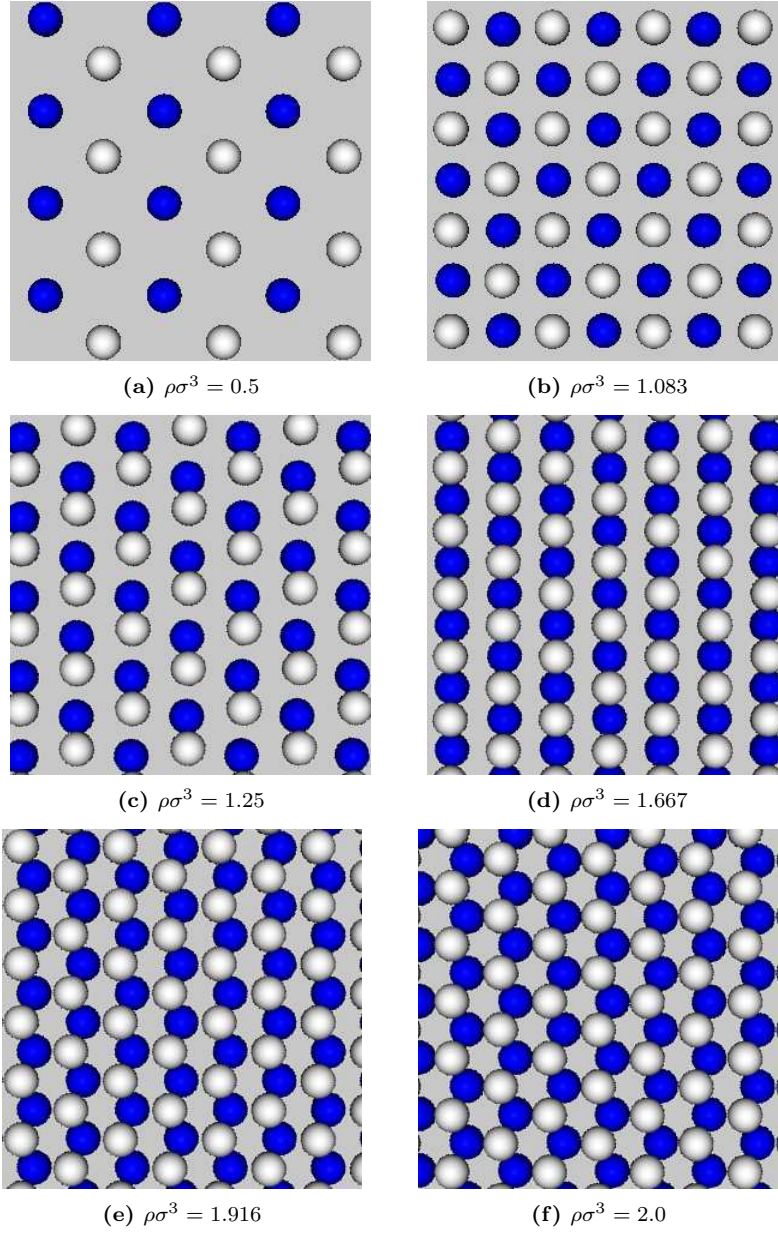


Figure 6.27: Exemplary pictures of the minimum energy configurations of a quasi-planar system of dipolar colloids at a cell thickness of $D = 1.445\sigma$. The different vertical positions of the particles are colour-coded: blue particles are located at the bottom of the cell, white particles at the top.

edge of the rectangle. At the high end of the investigated density regime, i. e. at $\rho\sigma^3 = 1.916$, the two layers forming the lane-like arrangement are shifted with respect to each other along the larger edge of the rectangle and staggered chains appear in consequence (see figure 6.27, (e)). We believe that this displacement of particles in a lane increases with the density until a honey comb lattice, like the one observed at $\rho\sigma^3 = 2.0$ is formed. In the honey comb structure, each particle has three nearest neighbours (see figure 6.27, (f)) – a number compatible with the energetically favoured up-down positioning of neighbouring particles.

The minimum energy configurations obtained for larger values of the cell thickness, $D = 1.55\sigma$, $D = 1.6\sigma$, and $D = 1.8\sigma$ where the interaction potential has attractive components, resemble in general the sequence discussed above for $D = 1.445\sigma$. Representative collections of the structures identified as MECs are shown in figures 6.28, 6.29, and 6.30. In these sequences of structures, we do observe the following changes though: rectangular or square lattices do not occur in the entire investigated density range for all three D -values. Additionally, the density region in which the formation of dimers is observed as the energetically most favourable arrangement gradually shrinks and moves to lower values of $\rho\sigma^3$: we obtain stable dimer configurations in cells of thickness $D = 1.55\sigma$ at $\rho\sigma^3 = 0.50, 0.5833, 0.667$, and 0.75 ; for a cell thickness of $D = 1.6\sigma$, dimers are obtained as the most favourable arrangement only at $\rho\sigma^3 = 0.5$, and for systems of a cell thickness $D = 1.8\sigma$, no dimer-phase is observed at all. Furthermore, arrangements of lane segments consisting of four particles appear among the observed structures for low values of the volume density as soon as the cell is wide enough for the interaction potential to display an attractive region adjacent to the hard core, i. e. for $D = 1.6\sigma$ and 1.8σ (see figures 6.29, (b) and 6.30, (b)). Concerning the formation of lanes, we observe the density regime for which the arrangement in alternating chains is the most favourable configuration to broaden and move to gradually lower values of the particle volume density at the same time: the GA identifies lanes as the minimum energy configuration for $D = 1.55\sigma$ at all investigated density values from $\rho\sigma^3 = 0.833$ to $\rho\sigma^3 = 1.5$. For cells of a thickness $D = 1.6\sigma$, lane-formation is first observed at $\rho\sigma^3 = 0.667$, and the arrangement in straight lanes persists until the onset of staggering at $\rho\sigma^3 = 1.5$. At $D = 1.8\sigma$, structures consisting of straight lanes appear for particle volume densities between $\rho\sigma^3 = 0.583$ and 1.667 . For all three systems, the honey comb lattice is approached at high values of the particle volume density. The structure is clearly visible for $D = 1.55\sigma$ and 1.6σ (see figures 6.28, (d) and 6.29, (d)), whereas the configuration obtained at the highest value of the particle volume density $\rho\sigma^3 = 2.0$ for $D = 1.8\sigma$ shows only the first inklings of the honey comb lattice (see figure 6.30, (d)).

6.3.2 Comparison to experiments and simulations

We compare the structures identified by the GA as minimum energy configurations to the arrangements observed in experiments and Monte Carlo simulations on quasi-planar systems of dipolar colloids presented in [9, 10].

The experiments conducted by Osterman et al. utilise super-paramagnetic colloids confined to

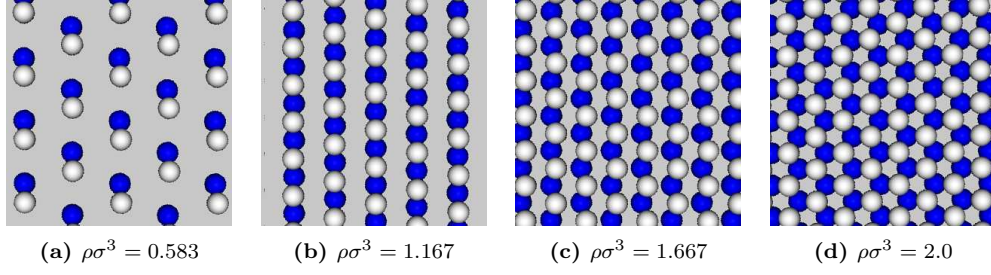


Figure 6.28: Representative examples of the minimum energy configurations of a quasi-planar system of dipolar colloids at a cell thickness of $D = 1.55\sigma$. The different vertical positions of the particles are colour-coded: blue particles are located at the bottom of the cell, white particles at the top.

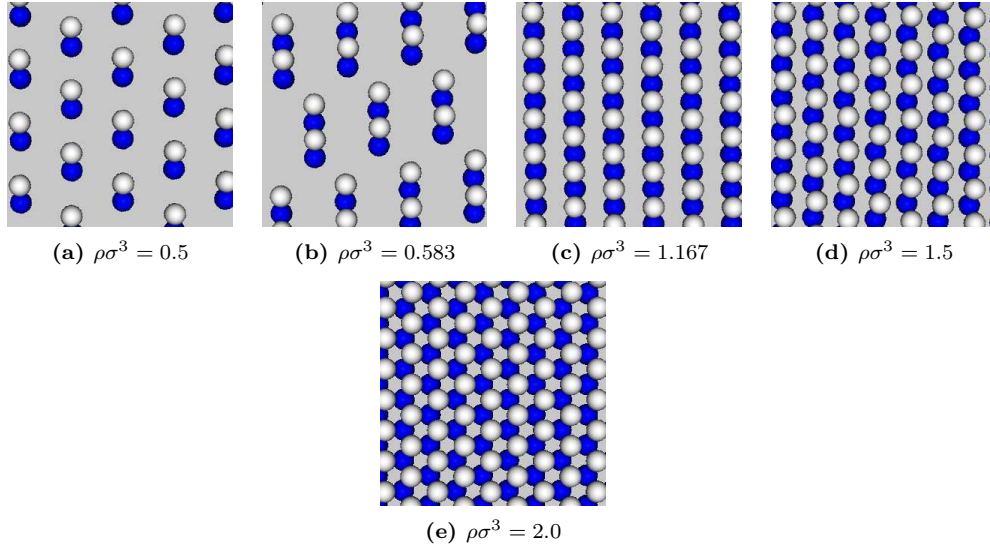


Figure 6.29: Representative examples of the minimum energy configurations of a quasi-planar system of dipolar colloids at a cell thickness of $D = 1.6\sigma$. The different vertical positions of the particles are colour-coded: blue particles are located at the bottom of the cell, white particles at the top.

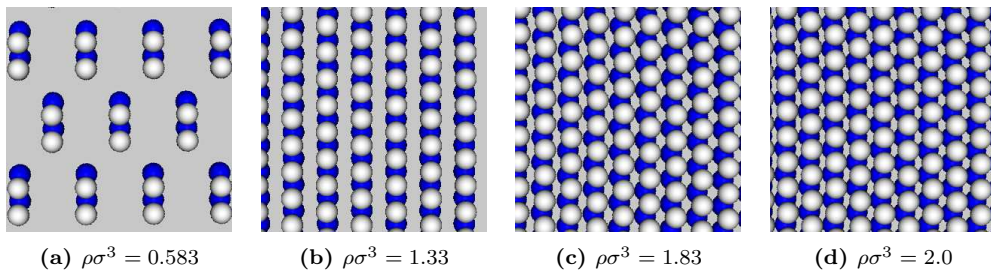


Figure 6.30: Representative examples of the minimum energy configurations of a quasi-planar system of dipolar colloids at a cell thickness of $D = 1.8\sigma$. The different vertical positions of the particles are colour-coded: blue particles are located at the bottom of the cell, white particles at the top.

a thin wedge-shaped cell [9]. An external magnetic field applied perpendicular to the basis plane of the cell induces magnetic moments in the colloidal particles and guarantees for the characteristic dipole-dipole interactions (cf. (2.10)). By tuning the strength of the magnetic field \mathbf{B} , the dimensionless interaction strength,

$$\Gamma = \frac{E_{\text{magn.}}(\mathbf{B})}{k_B T} ,$$

where $E_{\text{magn.}}$ is the potential energy, was set to $\Gamma \approx 400$, thus focusing the investigations on the low-temperature behaviour of the system. Osterman et al. investigated the structures formed at a cell thickness of $D = \sigma + h = 1.445\sigma$, which corresponds to an interaction close to the cross-over from the purely repulsive to the attractive regime (cf. section 2.3). The region in the wedge-shaped cell that exhibits the desired thickness was determined in the following indirect fashion: in the absence of a magnetic field, the colloidal particles cluster on contact. As the interaction between the colloids is still purely repulsive at $D = 1.445\sigma$, the sought-after region can be identified as the area where these clusters still fully disintegrate under the influence of the magnetic field [9]. The thus identified region of the cell was observed with an inverse optical microscope for gradually decreasing particle area fraction α , which is related to the dimensionless particle volume density $\rho\sigma^3$ via

$$\alpha = \frac{\pi\rho\sigma^3 h}{4\sigma} . \quad (6.3)$$

In the above equation, h denotes the maximal vertical shift that the particles can obtain in the cell and σ is the diameter of the colloidal particles.

In addition to the experimental investigations, Monte Carlo simulations (abbreviated "MC simulations") were performed by Dobnikar et al. [9, 10] to provide a better understanding of the experimentally obtained sequence of structures. As in the experiments, the vertical displacement of the particles was limited to $h = 0.445\sigma$ and the emerging configurations were observed for varying values of the particle area fraction α . Samples of up to 1000 particles were considered in various simulation box geometries, employing horizontally periodic boundary conditions. The MC simulations were conducted at two different values of the interaction strength, $\Gamma = 375$ and $\Gamma = 125$. The lower value, $\Gamma = 125$, was employed in dense systems in order to speed up convergence.

The sequences of configurations obtained in experiments and simulations comprise the following structures, as illustrated in figure 6.31 (taken from reference [9]) by suitably selected snapshots: an expanded hexagonal lattice is found at very low densities where the vertical displacements of the particles seem to be uncorrelated and, in addition, are distributed evenly across the available range of $z = 0$ to $h = 0.445\sigma$. If the density is increased, the expanded hexagonal lattice is soon superseded by an expanded square structure, where the particles keep exclusively to the top and the bottom of the cell. A further increase in density leads to the emergence of short and

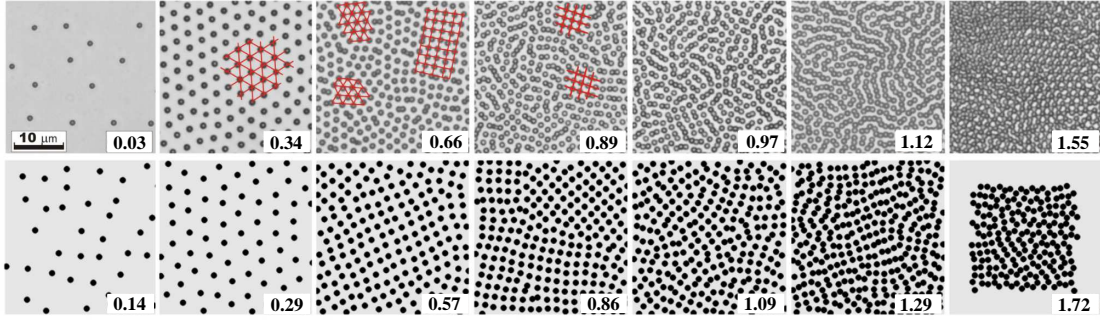


Figure 6.31: Pictures of the structures observed for a cell thickness of $D = 1.445\sigma$ in experiments (top row) and MC simulations (bottom row) when varying the particle volume density. Patches of the identified lattices are emphasised in some pictures. (Figure taken from [9] and labels changed from particle area fraction to the corresponding values of the particle volume density $\rho\sigma^3$ according to equation (6.3)).

long chains of particles instead of the formation of a square lattice. The vertical position of the particles along the chains alternate between the two extreme positions $z = 0$ and $z = h$. As the density is increased further, these chains interconnect and labyrinthine structures are formed. In the high density regime, honey comb lattices and dense square structures are observed, where the respective nearest neighbours occupy opposite vertical positions in the cell, thus maximising the distance between particles.

Apart from information on the emerging structures, the MC simulations also provide us with the corresponding energies of the different particle arrangements. Figure 6.32 shows the energy per particle for the hexagonal and the square phase as they were calculated in reference [9] in units of ε (cf. section 2.3) and scaled with the particle area fraction $\alpha^{3/2}$, as a function of the particle area fraction α . The energy per particle of the arrangements obtained in the MC simulations is also shown in this figure. Although determined at a different temperature ($T = 0$), we have included the energies of the structures identified by the GA into the plot in colour.

The general trends in the formation of stable structures observed in simulations and experiments are well reproduced in our study with the GA-based optimisation technique: with increasing density, we find square lattices, the arrangement of particles into lanes and the formation of a honey comb structure in the same sequence as in the experiments and the simulations. Although not included in the survey presented in reference [9], also the dimer phase was observed as the stable arrangement between the square lattice and the formation of chains in previous investigations [10]. In addition, we can interpret the centred rectangular structure observed with the GA at low densities (see figure 6.27, (a)) as a transitory state between the square lattice and the disordered hexagonal phase, the latter inaccessible to the GA due to its disordered nature. The dense square phase mentioned in [9] might have been missed in our investigation due to an unsuitably chosen density range.

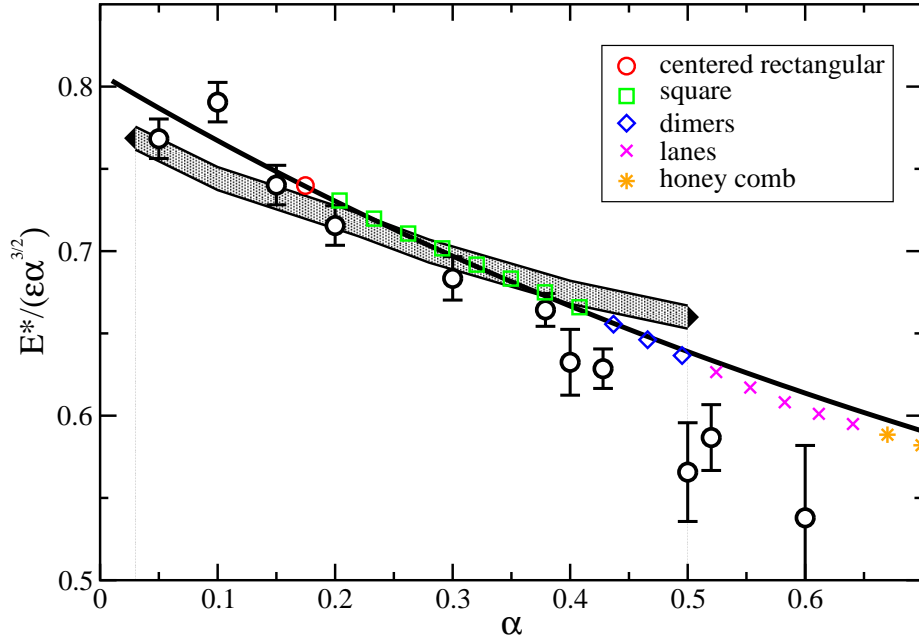


Figure 6.32: Energy per particle E^* in units of ϵ and scaled with the particle area fraction α vs. the particle area fraction α , obtained for a quasi-planar system of cell thickness $D = 1.445\sigma$. The depicted results are from numerical optimisations of the hexagonal (broad shaded line) and the square lattice (solid black line) [9] and from the structures observed in Monte Carlo simulations (open circles with error bars) [9]. The values for the structures identified to be stable at $T = 0$ by the GA are marked by other symbols as indicated.

It seems that most of the discrepancies between the results obtained by experiments and simulations and the findings of the GA-approach have their origin in the fact that both, experiments and simulation were conducted at finite temperature and thus allow for the arrangement of particles in disordered patterns like the labyrinthine structure or the expanded hexagonal phase with its uncorrelated vertical positioning of particles. The GA-approach, on the other hand, was restricted to $T = 0$ and therefore only included ordered structures into the search for the minimum energy configuration.

Chapter 7

Conclusions

In this work, we have studied the ordered equilibrium structures of two-dimensional soft matter systems. To identify the stable particle arrangements, an optimisation technique based on genetic algorithms [26] has been employed, which allowed for an unbiased search among all lattice structures. Despite of the simple, radially symmetric interactions in all investigated systems, we have been able to identify a rich variety of often complex and highly asymmetric configurations – a demonstration of the power of our search strategy to reliably determine the minimum energy configurations even if confronted with a rugged potential energy landscape.

With the aid of this highly efficient method, we have investigated the solid phases of three model systems at zero temperature: first, we have studied hard-core particles interacting via a purely repulsive, step-shaped shoulder of variable width at varying pressure. The identified minimum energy configurations can be separated into three groups: above a certain width of the repulsive shoulder, clusters composed of as many as nine particles populating the sites of ordered lattices have been observed in the low pressure regime. At intermediate values of the pressure, lane-like structures of various shape emerge, superseding the cluster phases. The third group of stable patterns, which has been found in the high pressure regime, consist of compact configurations characterised by a dense distribution of particles. As the shoulder width increases, the internal arrangement of particles inside the observed clusters appeared less and less ordered, thus establishing a link to various other models in soft matter physics that exhibit cluster phases [13, 91, 92].

The variety of ordered structures that has been encountered for the second system – a binary mixture of dipolar colloids – is even more extensive. Depending on the polarisability ratio of the constituent particle species and on the composition of the mixture the monolayer has been observed to order in a vast number of different alloy phases, most of which are highly complex and exhibit only a low degree of symmetry: as the number of weaker dipoles increase in the system, the particles arrange in more and more intricate patterns and, depending on the polarisability ratio,

dipoles group together or form distinct lane-like structures. If the particles of lower polarisability represent the minority in the system, however, the formed configurations are composed of only a small set of recurrent lattice elements or "tiles". Since different tilings with approximately the same energy have been discovered in our survey, randomly tiled phases [94] might be among the ground states of the binary mixture of dipolar colloids. In an effort to understand the mechanisms leading to this immense diversity of non-trivial structures and to investigate the influence of the interactions on structure formation, we have compared our findings to the stable configurations of a binary hard-disc mixture [94], revealing that even in dilute systems, packing arguments play an important role in how particles are arranged to energetically favourable configurations. In addition, two different experimental realisations [40, 41, 47, 95] of our model system provide us with the possibility to verify our results. Although the dynamics of crystal growth impedes the formation of extended crystals, and only locally ordered structures emerge in experiments, we have been able to confirm several patterns that have been identified with the genetic algorithm-based method.

As the last system, we have investigated monodisperse dipolar colloids in a horizontally confined cell for different values of the cell thickness and varying density. The system illustrates the cross-over from two to three dimensions, as particles are allowed to buckle from the strict two-dimensional setup. The nature of the pair potential acting between colloids is controlled via the spatial constraints and ranges from the purely repulsive dipole-dipole interactions typical for two-dimensional systems, to potentials which are attractive at short distances. Independent of the density and the cell thickness, particles have been observed to keep to either the top or the bottom positions in the cell, thus maximising the distance between nearest neighbours in the emerging structure. Since only a small number of ordered configurations is compatible with this preferred up-down arrangement of particles, the identified sequences of minimum energy configurations show a much smaller diversity than those observed in the previous cases and consist of largely the same, recurrent mesophases: square or rectangular lattices have been found at low densities, dimer phases or larger segments of particle chains as well as various lane-like arrangements populate the region of intermediate density and at high densities, particles have been found to form honey-comb structures. Where available, results obtained in experiments and Monte Carlo simulations largely agree with our theoretical predictions. We point out, that at intermediate cell thickness, where the interaction is still purely repulsive, the sequences of stable structures closely resemble the minimum energy configurations formed by the square-shoulder system at small values of the shoulder width – a fact that leads us to the notion the exact functional form of the interaction potential might be of minor importance in structure formation.

Motivated by a rapidly growing interest and prospective technological applications [80, 90, 98–100], we have also investigated the dispersion relations of several of the obtained particle arrangements. Focusing on a few examples, we have been able to demonstrate that the soft matter

compounds studied in this thesis offer a new way to tune the phonon band structures of soft materials. By controlling the composition of the mixture and the mass ratio of the two particle species, multiple phononic gaps have been opened in the band structures, yielding the system "opaque" to vibrations within a certain frequency range. In addition, optical branches have been observed to flatten considerably, if the mass ratio is sufficiently reduced.

Like every PhD thesis, also this work has its loose ends: the phase diagram of the quasi-planar system of dipolar colloids is currently revised, considering a broader density range and additional values of the cell thickness in order to fully understand the transitions between the observed solid phases. Also the promising results obtained in the study of the phononic spectra warrant closer investigations, as the observed dependencies of the dispersion curves on the system parameters are in need of further verification.

Due to an increase in the efficiency in the last few years, the implementation of computationally and conceptually more sophisticated tools to determine the energy of a given system – like density functional theory [19–21] – can now be considered within reach, so that another logical next step in our investigations is to extend the search technique to systems at finite temperature.

Appendix A

An unambiguous lattice parametrisation

Inequality (4.6) is derived in the following way: Let us choose a configuration K , the minimal description in the above mentioned way. Therefore the transformations ((4.4), (4.5)) cannot yield a unit cell of smaller circumference. Without loss of generality we can set $\mathbf{a}, \mathbf{b} \geq \mathbf{0}$ and $|\mathbf{a}| > |\mathbf{b}|$ and thus only need to take

$$(\mathbf{a}, \mathbf{b}) \rightarrow (\mathbf{a} - \mathbf{b}, \mathbf{b})$$

into account. With

$$\mathbf{a} = a(1, 0) \quad , \quad \mathbf{b} = ax(\cos \phi, \sin \phi)$$

this leads to

$$\begin{aligned} |\mathbf{a}| + |\mathbf{b}| &\leq |\mathbf{a} - \mathbf{b}| + |\mathbf{b}| \rightarrow \\ a^2 &\leq (a - ax \cos \phi)^2 + (ax \sin \phi)^2 \rightarrow \\ 2 \cos \phi &\leq x \quad , \end{aligned}$$

because of our first assumption of K being the configuration of minimal circumference.

Appendix B

Square Shoulder System: Minimum energy configurations

Full sequence of MECs for $\lambda = 1.5\sigma$

structure	U^*	$\eta\sigma^2$	stable P^* -range
(a)	0	0.5132	0.0 – 1.872
(b)	1	0.7071	1.872 – 2.757
(c)	3/2	0.8111	2.757 – 4.089
(d)	3	1.1547	4.089 – ∞

Table B.1: *Properties of the MECs proposed by the GA for a square-shoulder system of shoulder width $\lambda = 1.5\sigma$: the internal energy per particle in reduced units, U^* , the particle area density $\eta\sigma^2$, and the range of pressure values P^* , for which the structures were found to be stable (cf. section 6.1). The letters given in the first column to distinguish the individual structures refer to figure B.1.*

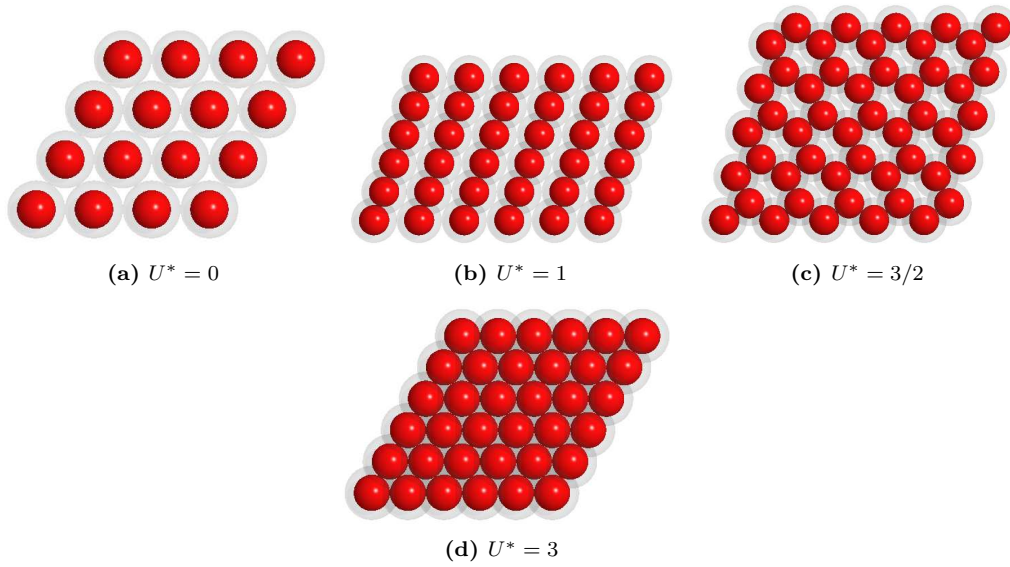


Figure B.1: *Full sequence of minimum energy configurations found for a square-shoulder system of shoulder range $\lambda = 1.5\sigma$ with their respective internal energy per particle U^* in reduced units (cf. section 6.1) .*

Full sequence of MECs for $\lambda = 3\sigma$

structure	U^*	$\eta\sigma^2$	stable P^* -range
(a)	0	0.1283	0.0 – 0.2078
(b)	1/2	0.1856	0.2078 – 0.4534
(c)	1	0.2334	0.4534 – 0.7536
(d)	2	0.3380	0.7536 – 2.0834
(e)	7/2	0.4468	2.0834 – 3.1488
(f)	14/3	0.5355	3.1488 – 4.3196
(g)	6	0.6415	4.3196 – 6.3156
(h)	13/2	0.6758	6.3156 – 6.8564
(i)	9	0.8968	6.8564 – 15.5370
(j)	11	1.0138	15.5370 – 33.2379
(k)	15	1.1547	33.2379 – ∞

Table B.2: *Properties of the MECs proposed by the GA for a square-shoulder system of shoulder width $\lambda = 3\sigma$: the internal energy per particle in reduced units, U^* , the particle area density $\eta\sigma^2$, and the range of pressure values P^* , for which the structures were found to be stable (cf. section 6.1). The letters given in the first column refer to the pictures shown in figure B.2.*

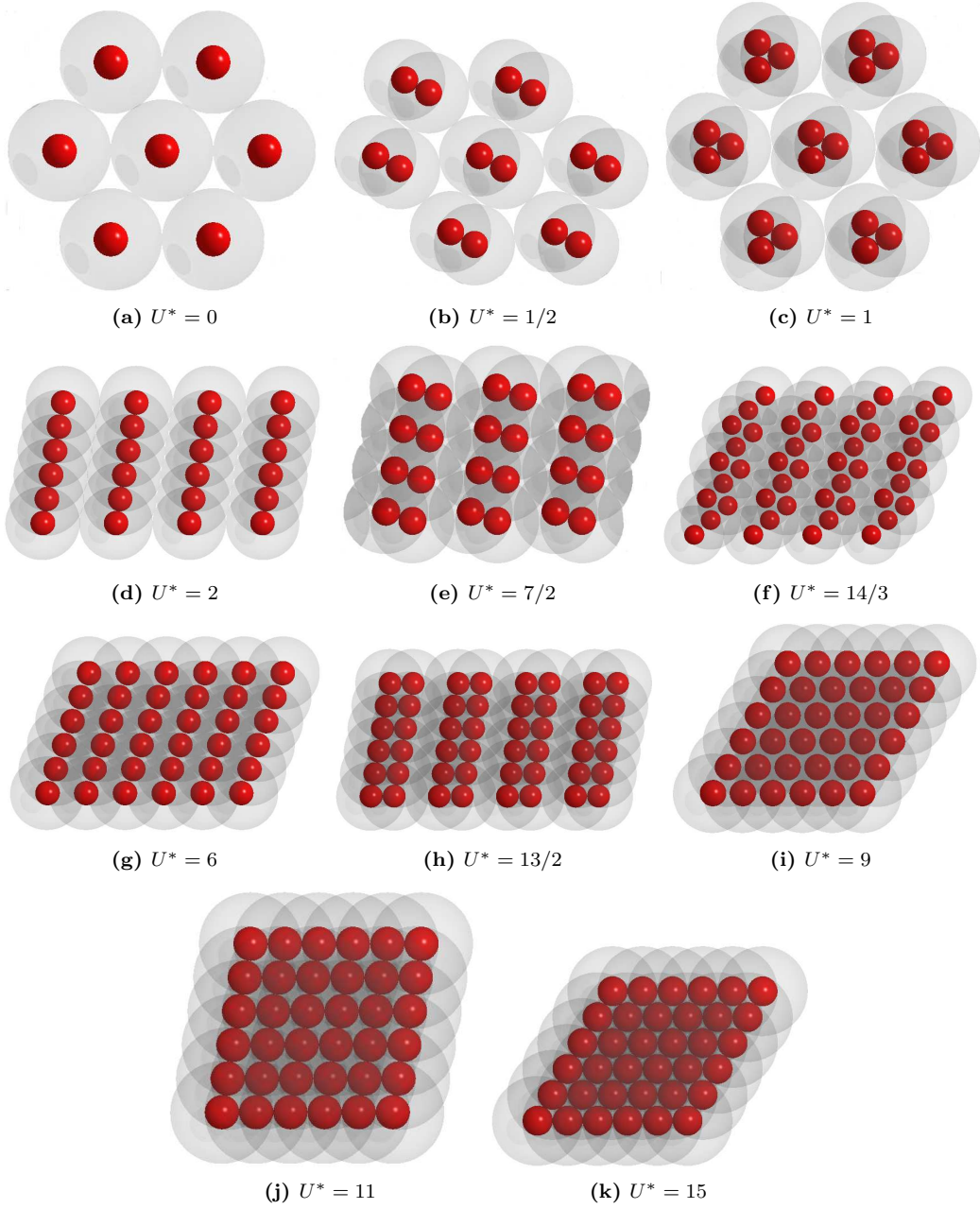


Figure B.2: *Full sequence of minimum energy configurations found for a square-shoulder system of shoulder range $\lambda = 3\sigma$ with their respective internal energy per particle U^* in reduced units (cf. section 6.1).*

Full sequence of MECs for $\lambda = 5\sigma$

structure	U^*	$\eta\sigma^2$	stable P^* -range
(a)	0	0.0000	0.0000 – 0.0604
(b)	1/2	0.0748	0.0604 – 0.1571
(c)	1.	0.0982	0.1571 – 0.3372
(d)	7/4	0.1256	0.3372 – 0.7107
(e)	3	0.1613	0.7107 – 0.8153
(f)	4	0.2010	0.8153 – 2.0153
(g)	13/2	0.2678	2.0153 – 2.7117
(h)	17/2	0.3337	2.7117 – 5.1711
(i)	11	0.3979	5.1711 – 7.2312
(j)	44/3	0.4984	7.2312 – 13.4869
(k)	56/3	0.5849	13.4869 – 15.1363
(l)	21	0.6428	15.1363 – 18.1230
(m)	24	0.7194	18.1230 – 21.2024
(n)	27	0.8009	21.2024 – 28.1631
(o)	34	0.9999	28.1631 – 59.6821
(p)	42	1.1547	59.6821 – ∞

Table B.3: *Properties of the MECs proposed by the GA for a square-shoulder system of shoulder width $\lambda = 5\sigma$: the internal energy per particle in reduced units, U^* , the particle area density $\eta\sigma^2$, and the range of pressure values P^* , for which the structures were found to be stable (cf. section 6.1). The letters given in the first column refer to the pictures shown in figure B.3*

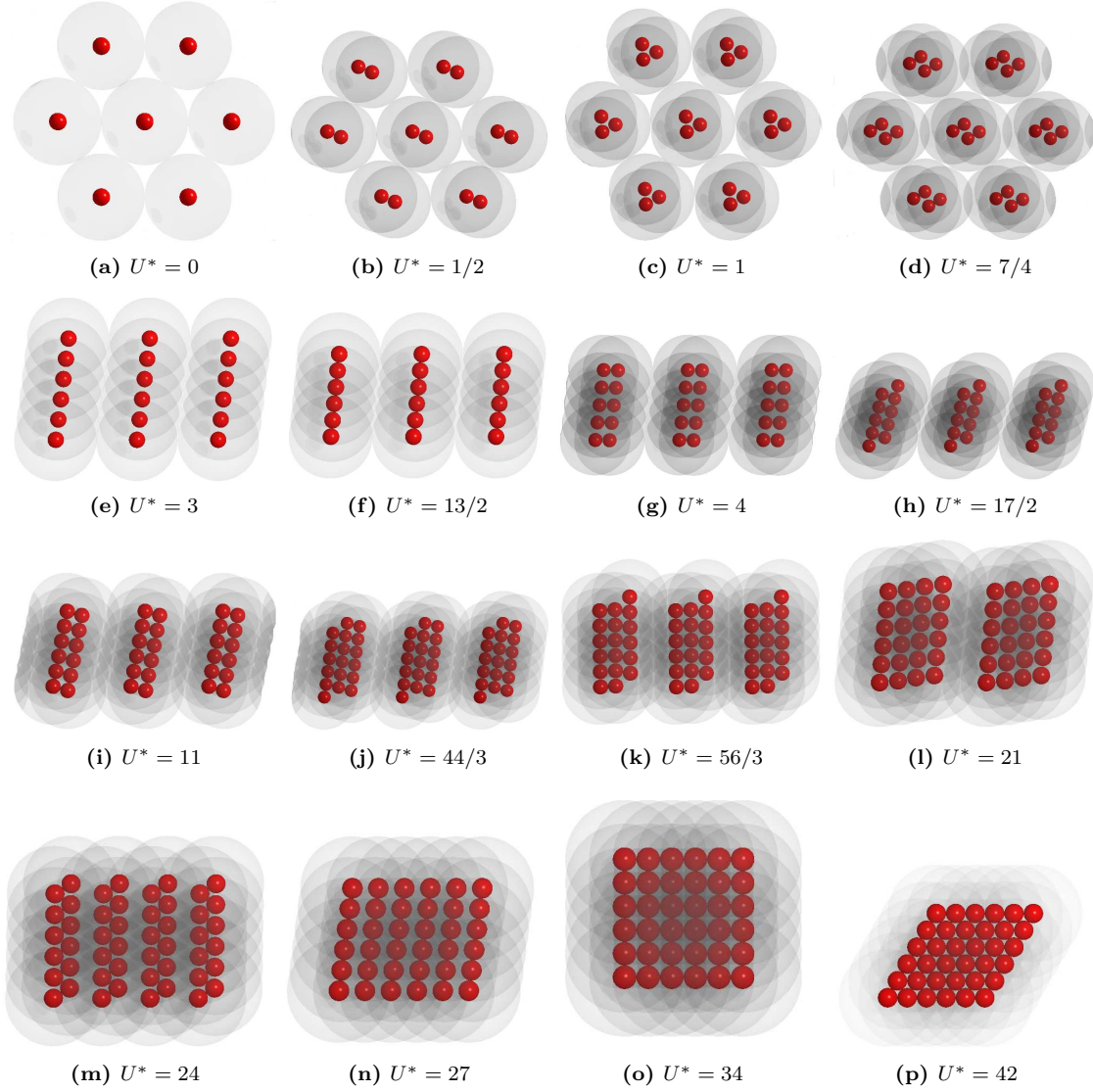


Figure B.3: *Full sequence of minimum energy configurations found for a square-shoulder system of shoulder range $\lambda = 5\sigma$ with their respective internal energy per particle U^* in reduced units (cf. section 6.1).*

Full sequence of MECs for $\lambda = 7\sigma$

structure	U^*	$\eta\sigma^2$	stable P^* -range
(a)	0	0.0236	0.0000 – 0.0282
(b)	1/2	0.0405	0.0282 – 0.0744
(c)	1	0.0556	0.0744 – 0.1654
(d)	3/2	0.0668	0.1654 – 0.2636
(e)	5/2	0.0895	0.2636 – 0.5245
(f)	15/4	0.1138	0.5245 – 1.5452
(g)	17/2	0.1785	1.5452 – 2.1180
(h)	21/2	0.2157	2.1180 – 3.0214
(i)	25/2	0.2502	3.0214 – 6.4725
(j)	53/3	0.3127	6.4725 – 6.9967
(k)	64/3	0.3740	6.9967 – 11.7793
(l)	65/3	0.3780	11.7793 – 14.3968
(m)	27	0.4395	14.3968 – 14.8260
(n)	55/2	0.4428	14.8260 – 15.1357
(o)	31	0.4974	15.1357 – 27.5137
(p)	109/4	0.5665	27.5137 – 28.5437
(q)	38	0.5693	28.5437 – 29.4987
(r)	125/3	0.6127	29.4987 – 31.2630
(s)	46	0.6696	31.2630 – 36.3017
(t)	52	0.7529	36.3017 – 48.8709
(u)	54	0.7768	48.8709 – 53.8705
(v)	178/3	0.8415	53.8705 – 71.9874
(w)	81	1.1284	71.9874 – 129.6095
(x)	82	1.1383	129.6095 – 160.2448
(y)	84	1.1547	160.2448 – ∞

Table B.4: *Properties of the MECs proposed by the GA for a square-shoulder system of shoulder width $\lambda = 7\sigma$: the internal energy per particle in reduced units, U^* , the particle area density $\eta\sigma^2$, and the range of pressure values P^* , for which the structures were found to be stable (cf. section 6.1). The letters given in the first column refer to the pictures shown in figure B.4.*

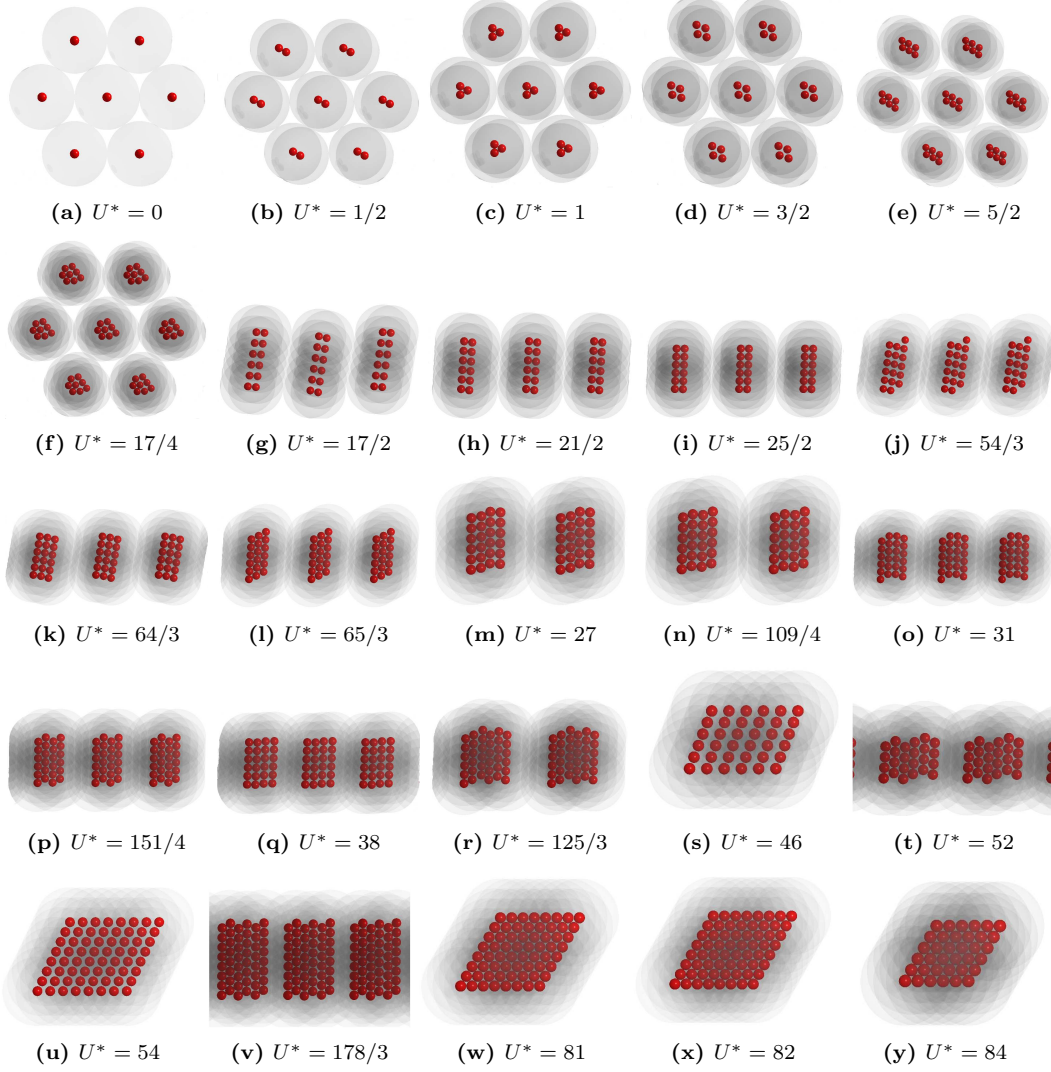


Figure B.4: *Full sequence of minimum energy configurations found for a square-shoulder system of shoulder range $\lambda = 7\sigma$ with their respective internal energy per particle U^* in reduced units (cf. section 6.1).*

Full sequence of MECs for $\lambda = 10\sigma$

structure	U^*	$\eta\sigma^2$	stable P^* -range
(B.5,a)	0	0.0125	0.0000 – 0.0130
(B.5,b)	1/2	0.0207	0.0130 – 0.0391
(B.5,c)	1	0.0282	0.0391 – 0.0767
(B.5,d)	3/2	0.0345	0.0767 – 0.2666
(B.5,e)	5/2	0.0496	0.2666 – 0.3816
(B.5,f)	4	0.0669	0.3816 – 0.4237
(B.5,g)	6	0.0702	0.4237 – 0.5640
(B.5,h)	7	0.0802	0.5640 – 0.7236
(B.5,i)	8	0.0901	0.7236 – 0.9037
(B.6,a)	9	0.1001	0.9037 – 1.6948
(B.6,b)	25/2	0.1262	1.6948 – 1.9126
(B.6,c)	29/2	0.1454	1.9126 – 2.6294
(B.6,d)	33/2	0.1635	2.6294 – 3.2887
(B.6,e)	37/2	0.1816	3.2887 – 6.2722
(B.6,f)	82/3	0.2439	6.2722 – 8.3190
(B.6,g)	92/3	0.2703	8.3190 – 12.9347
(B.6,h)	79/2	0.3315	12.9347 – 19.3908
(B.6,i)	89/2	0.3625	19.3908 – 33.6106
(B.6,j)	53	0.3991	33.6106 – 37.4077
(B.6,k)	220/3	0.5097	37.4077 – 46.8181
(B.6,l)	78	0.5370	46.8181 – 48.4984
(B.7,a)	87	0.5964	48.4984 – 63.8452
(B.7,b)	193/2	0.6545	63.8452 – 70.2321
(B.7,c)	105	0.7108	70.2321 – 82.0690
(B.7,d)	111	0.7498	82.0690 – 85.4410
(B.7,e)	116	0.7842	85.4410 – 113.8668
(B.7,f)	135	0.9011	114.8668 – 133.7881
(B.7,g)	156	1.0495	133.7881 – 227.4269
(B.7,h)	166	1.1003	227.4269 – 327.1034
(B.7,i)	180	1.1547	327.1034 – ∞

Table B.5: *Properties of the MECs proposed by the GA for a square-shoulder system of shoulder width $\lambda = 10\sigma$: the internal energy per particle in reduced units, U^* , the particle area density $\eta\sigma^2$, and the range of pressure values P^* , for which the structures were found to be stable (cf. section 6.1). The letters given in the first column refer to the pictures shown in figures B.5 to B.7.*

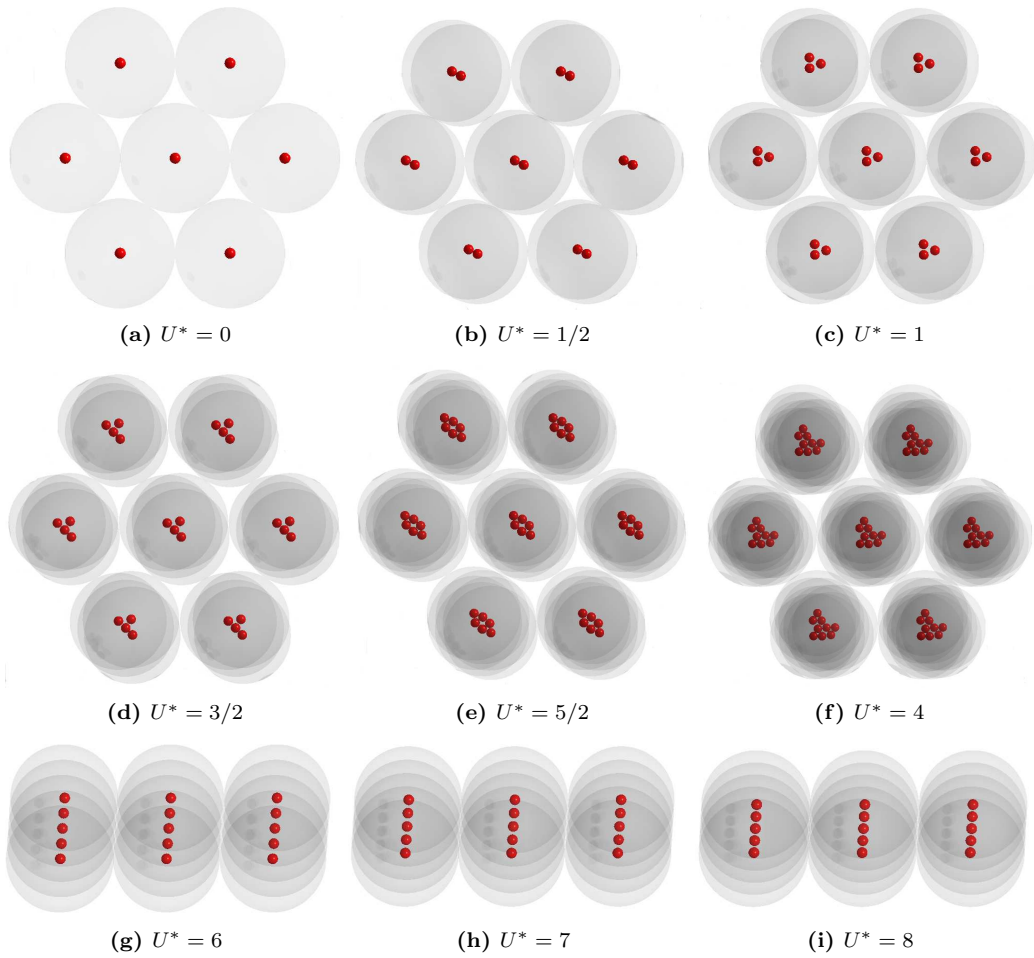


Figure B.5: Full sequence of minimum energy configurations found for the square-shoulder system of shoulder range $\lambda = 10\sigma$ with their respective internal energy per particle U^* in reduced units (cf. section 6.1)

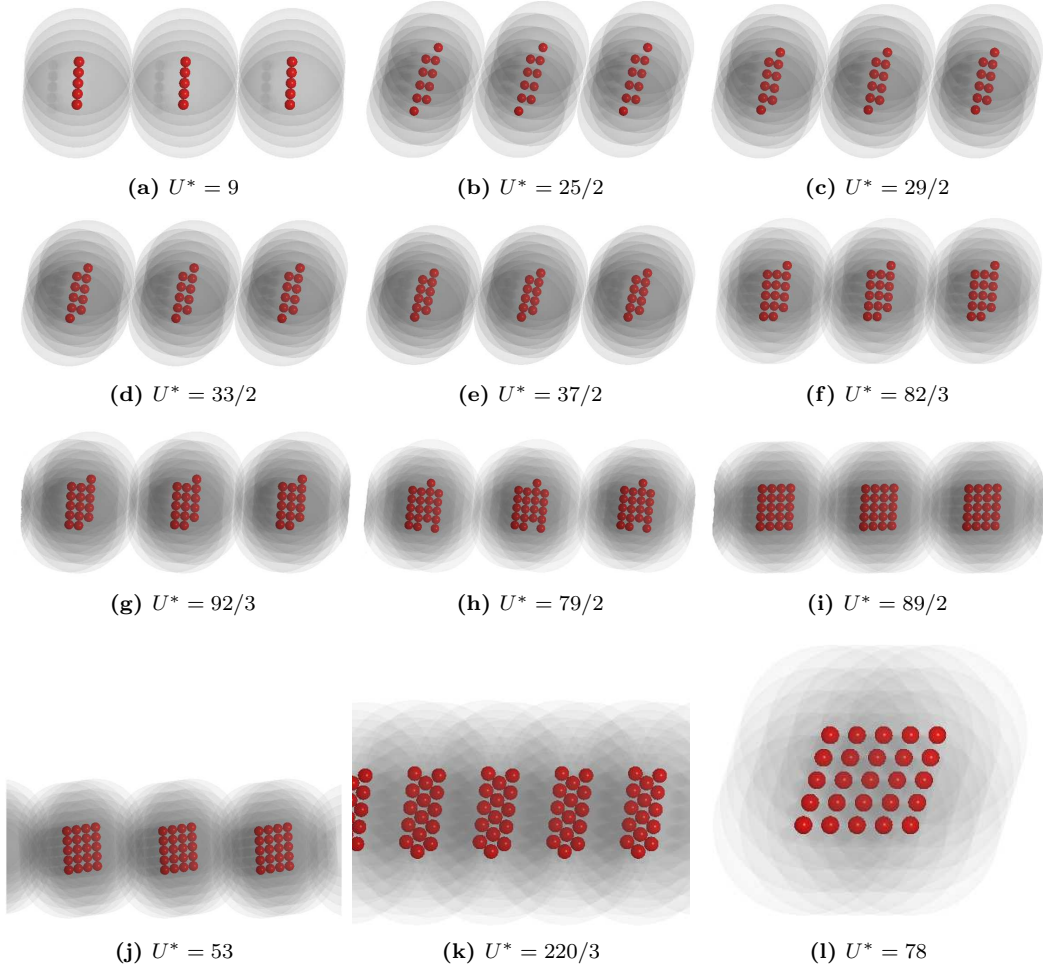


Figure B.6: *Full sequence of minimum energy configurations found for the square-shoulder system of shoulder range $\lambda = 10\sigma$ with their respective internal energy per particle U^* in reduced units (continued from figure B.5).*

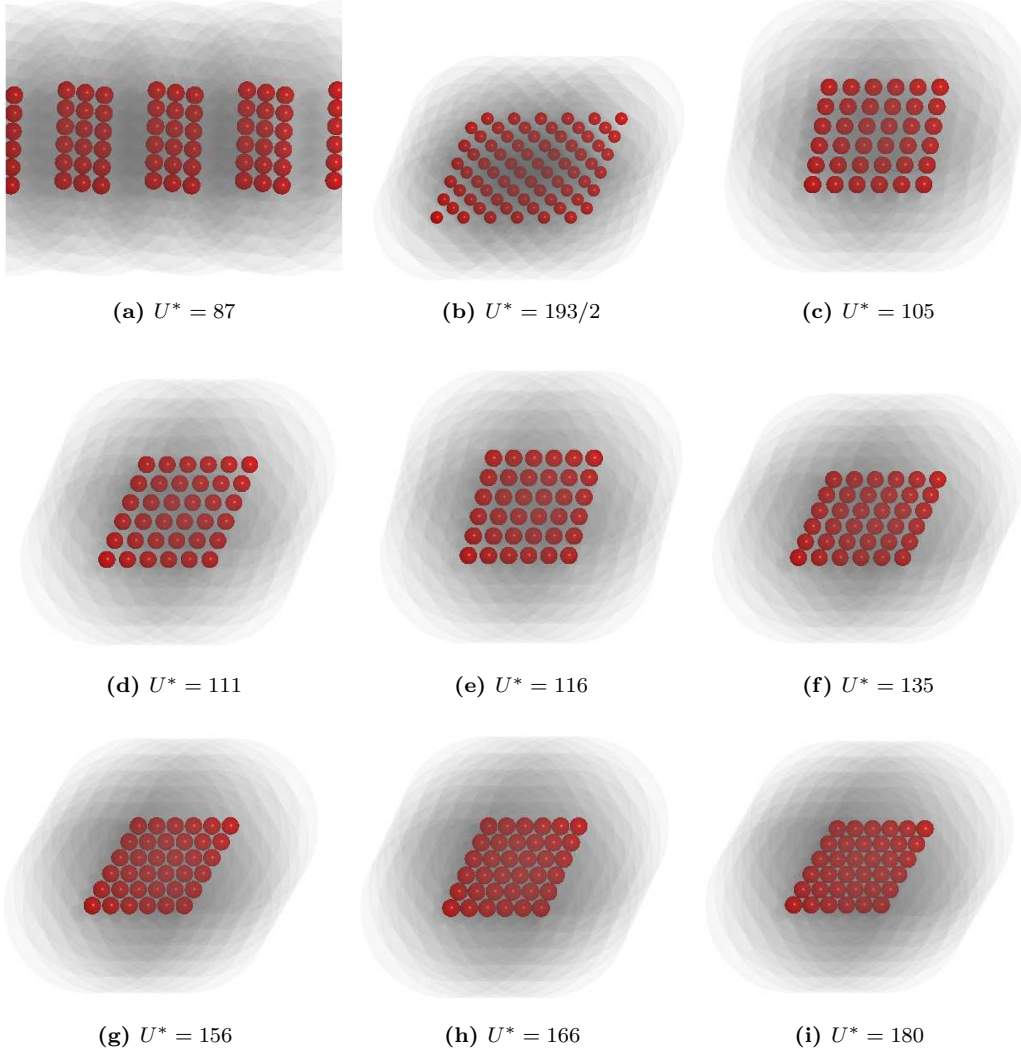


Figure B.7: Full sequence of minimum energy configurations found for the square-shoulder system of shoulder range $\lambda = 10\sigma$ with their respective internal energy per particle U^* in reduced units (continued from figure B.6).

Bibliography

- [1] R. Hunter, *Foundations of Colloid Science, Vol I*, Clarendon Press, Oxford, 1986.
- [2] W.B. Russel, D.A. Saville and W.R. Schowalter, *Colloidal Dispersions*, Cambridge University Press, Cambridge, 1990.
- [3] W.G. McMillan Jr. and J.E. Mayer, *J. Chem. Phys.*, 1945, **13**, 276.
- [4] J.G. Kirkwood and F.P. Buff, *J. Chem. Phys.*, 1951, **19**, 774.
- [5] C.N. Likos, *Phys. Rep.*, 2001, **348**, 267.
- [6] B.M. Mladek, G. Kahl and C.N. Likos, *Phys. Rev. Lett.*, 2008, **100**, 028301.
- [7] C.A. Murray and D.G. Grier, *Annu. Rev. Phys. Chem.*, 1996, **47**, 421.
- [8] A. Ashkin, *Phys. Rev. Lett.*, 1970, **24**, 156.
- [9] N. Osterman, D. Babič, I. Poberaj, J. Dobnikar and P. Ziherl, *Phys. Rev. Lett.*, 2007, **99**, 248301.
- [10] J. Dobnikar, J. Fornleitner and G. Kahl, *J. Phys.-Condens. Mat.*, 2008, **20**, 494220.
- [11] P. Ziherl and R. Kamien, *Phys. Rev. Lett.*, 2000, **85**, 3528.
- [12] M. Glaser, G. Grason, R. Kamien, A. Košmrlj, C. Santangelo and P. Ziherl, *Europhys. Lett.*, 2007, **78**, 46004.
- [13] B.M. Mladek, D. Gottwald, G. Kahl, M. Neumann and C.N. Likos, *Phys. Rev. Lett.*, 2006, **96**, 045701.
- [14] P.J. Camp, *Phys. Rev. E*, 2003, **68**, 061506.
- [15] G. Malescio and G. Pellicane, *Phys. Rev. E*, 2004, **70**, 021202.
- [16] D. Hajduk, P. Harper, S. Gruner, C. Honeker, G. Kim, E. Thomas and L. Fetters, *Macromolecules*, 1994, **27**, 4063.
- [17] W. Matsen, *J. Chem. Phys.*, 1998, **108**, 785.

- [18] C.K. Ullal, M. Maldovan, E.L. Thomas, G. Chen, Y.J. Han and S. Yang, *Appl. Phys. Lett.*, 2004, **84**, 5434–5436.
 - [19] Y. Singh, *Phys. Rep.*, 1991, **207**, 351.
 - [20] R. Evans, in *Fundamentals of Inhomogeneous Fluids*, ed. D. Henderson, Marcel Dekker, New York, 1992, ch. 3, pp. 85–175.
 - [21] M. Schmidt, *J. Phys.: Condens. Mat.*, 2003, **15**, 101.
 - [22] J.-P. Hansen and I.R. McDonald, *Theory of Simple Liquids*, Academic Press, London, 3rd edn., 2006.
 - [23] E. Velasco, L. Mederos and G. Navascués, *Langmuir*, 1998, **14**, 5652.
 - [24] E. Velasco, L. Mederos, G. Navascués, P.C. Hemmer and G. Stell, *Phys. Rev. Lett.*, 2000, **85**, 122–125.
 - [25] P. Ziherl and R. Kamien, *J. Phys. Chem. B*, 2001, **105**, 10147.
 - [26] J. Holland, *Adaption in Natural and Artificial Systems*, The University of Michigan Press, Ann Arbor, 1975.
 - [27] S.M. Woodley, P.D. Battle, J.D. Gale and C.R.A. Catlow, *Phys. Chem. Chem. Phys.*, 1999, **1**, 2535–2542.
 - [28] A.R. Oganov and C.W. Glass, *J. Chem. Phys.*, 2006, **124**, 244704.
 - [29] P. Siepmann, C. Martin, I. Vancea, P. Moriarty and N. Krasnogor, *Nano Letters*, 2007, **7**, 1985–1990.
 - [30] D. Gottwald, G. Kahl and C.N. Likos, *J. Chem. Phys.*, 2005, **122**, 204503–1.
 - [31] D. Gottwald, *Ph.D. thesis*, Institut für Theoretische Physik, TU Wien, 2005.
 - [32] E. Jagla, *J. Chem. Phys.*, 1999, **110**, 451.
 - [33] G. Malescio and G. Pellicane, *Nat. Mater.*, 2003, **2**, 97.
 - [34] D. Gottwald, C.N. Likos, G. Kahl and H. Löwen, *Phys. Rev. Lett.*, 2004, **92**, 068301.
 - [35] D. Gottwald, C.N. Likos, G. Kahl and H. Löwen, *J. Chem. Phys.*, 2005, **122**, 074903.
 - [36] Y. Norizoe and T. Kawakatsu, *Europhys. Lett.*, 2005, **72**, 583.
 - [37] V.S.K. Balagurusamy, G. Ungar, V. Perec and G. Johansson, *J. Am. Chem. Soc.*, 1997, **119**, 1539.
 - [38] G.A. McConnell and A.P. Gast, *Phys. Rev. E*, 1996, **54**, 5447.
-

-
- [39] G.A. McConnell and A.P. Gast, *Macromolecules*, 1997, **30**, 435.
- [40] R. Aveyard, J. Clint, D. Nees and V. Paunov, *Langmuir*, 2000, **16**, 1969–1979.
- [41] R. Aveyard, J. Clint, D. Nees and N. Quirke, *Langmuir*, 2000, **16**, 8820–8828.
- [42] T. Stirner and J. Sun, *Langmuir*, 2005, **21**, 6636–6641.
- [43] K. Zahn, J.M. Méndez-Alcaraz and G. Maret, *Phys. Rev. Lett.*, 1997, **79**, 175.
- [44] K. Zahn, R. Lenke and G. Maret, *Phys. Rev. Lett.*, 1999, **82**, 2721.
- [45] K. Zahn and G. Maret, *Phys. Rev. Lett.*, 2000, **85**, 3656.
- [46] K. Zahn, A. Wille, G. Maret, S. Sengupta and P. Nielaba, *Phys. Rev. Lett.*, 2003, **90**, 155506.
- [47] F. Ebert, P. Keim and G. Maret, *Eur. Phys. J. E*, 2008, **26**, 161.
- [48] D.A. Young and B. J. Alder, *Phys. Rev. Lett.*, 1977, **38**, 1213.
- [49] D.A. Young and B.J. Alder, *J. Chem. Phys.*, 1979, **70**, 473.
- [50] S.V. Buldyrev, G. Franzese, N. Giovambattista, G. Malescio, M.R. Sadr-Lahijany, A. Scala, A. Skibinsky and H. E. Stanley, *Physica A*, 2002, **304**, 23.
- [51] A.A. Koulakov, M.M. Fogler and B.I. Shklovskii, *Phys. Rev. Lett.*, 1996, **76**, 499.
- [52] M.M. Fogler, A.A. Koulakov and B.I. Shklovskii, *Phys. Rev. B*, 1996, **54**, 1853.
- [53] J. Sun and T. Stirner, *Langmuir*, 2001, **17**, 3103–3108.
- [54] N. Hoffmann, F. Ebert, C.N. Likos, H. Löwen and G. Maret, *Phys. Rev. Lett.*, 2006, **97**, 098301.
- [55] L. Assoud, R. Messina and H. Löwen, *Europhysics Letters*, 2007, **80**, 48001.
- [56] M. Toda, R. Kubo and N. Saito, *Statistical Physics I - Equilibrium Statistical Mechanics*, Springer-Verlag, Berlin, 1983.
- [57] W. Greiner, L. Neise and H. Stöcker, *Thermodynamik und Statistische Mechanik*, Verlag Harry Deutsch, Thun, 1987.
- [58] D. Chandler, *Introduction to Modern Statistical Mechanics*, Oxford University Press, Oxford, 1987.
- [59] C. Garrod, *Statistical Mechanics and Thermodynamics*, Oxford University Press, New York, 1995.
- [60] L.E. Reichl, *A modern course in statistical physics*, John Wiley and Sons, New York, 1998.
-

- [61] N.W. Ashcroft and N.D. Mermin, *Solid State Physics*, Saunders College Publishing, Harcourt Brace College Publishers, Fort Worth, 1976.
 - [62] J. Fornleitner, F. Lo Verso, G. Kahl and C.N. Likos, *Soft Matter*, 2008, **4**, 480.
 - [63] R.S. Rosenberg, *Mathematical Biosciences*, 1970, **8**, 1–37.
 - [64] R. Weinberg, *Ph.D. thesis*, University of Michigan, 1970.
 - [65] J. D. Bagley, *Ph.D. thesis*, University of Michigan, 1967.
 - [66] D. Cavicchio, *Ph.D. thesis*, University of Michigan, 1970.
 - [67] E. Schöneburg, *Genetische Algorithmen und Evolutionsstrategien*, Addison-Wesley Publishing Company, Bonn, Paris, 1994.
 - [68] D. Frenkel and B. Smit, *Understanding Molecular Simulation*, Academic Press, London, 2nd edn., 2002.
 - [69] S. Kirkpatrick, C.D. Gelatt Jr. and M.P. Vecchi, *Science*, 1983, **220**, 671.
 - [70] V. Cerny, *J. Optimiz. Theory App.*, 1985, **45**, 41.
 - [71] A.R. Oganov and C.W. Glass, *J. Phys.: Condens. Mat.*, 2008, **20**, 064210.
 - [72] B.M. Mladek, D. Gottwald, G. Kahl, M. Neumann and C.N. Likos, *Phys. Rev. Lett.*, 2006, **97**, 019901.
 - [73] B.M. Mladek, D. Gottwald, G. Kahl, M. Neumann and C.N. Likos, *J. Phys. Chem. B*, 2008, **111**, 12799–12808.
 - [74] G.J. Pauschenwein and G. Kahl, *Soft Matter*, 2008, **4**, 1396–1399.
 - [75] G.J. Pauschenwein, *Ph.D. thesis*, Institut für Theoretische Physik, TU Wien, 2008.
 - [76] M. Marder, *Condensed Matter Physics*, John Wiley and Sons, New York, 2000.
 - [77] H. Nowotny, *Theoretische Festkörperphysik II*, Institut für Theoretische Physik, TU Wien, 1997.
 - [78] A.J. Hurd, N.A. Clark, R.C. Mockler and W.J. O'Sullivan, *Phys. Rev. A*, 1982, **26**, 2869.
 - [79] Y.N. Ohshima and I. Nishio, *J. Chem. Phys.*, 2001, **114**, 8649.
 - [80] H.H. von Grünberg and J. Baumgartl, *Phys. Rev. E*, 2007, **75**, 051406.
 - [81] M. Hoppenbrouwers and W. van de Water, *Phys. Rev. Lett.*, 1998, **80**, 3871.
 - [82] P.P. Schram, A.G. Sitenkob and V.I. Zasenkov, *Physica B*, 1996, **228**, 197.
-

-
- [83] J.T. Padding and A.A. Louis, *Phys. Rev. E*, 2006, **74**, 031402.
- [84] A.J. Hurd, N.A. Clark, R.C. Mockler and W.J. O'Sullivan, *J. Fluid Mech.*, 1985, **153**, 401.
- [85] J.M. Hofman, H.J. Clercx and P.P. Schram, *Physica A*, 1999, **268**, 326.
- [86] J.M. Hofman, H.J. Clercx and P.P. Schram, *Physica A*, 1999, **268**, 353.
- [87] P. Keim, G. Maret, U. Herz and H.H. von Grünberg, *Phys. Rev. Lett.*, 2004, **92**, 215504.
- [88] R. Piazza and V. Degiorgio, *Phys. Rev. Lett.*, 1991, **67**, 3868.
- [89] Z. Cheng, J. Zhu, W.B. Russel and P.M. Chaikin, *Phys. Rev. Lett.*, 2000, **85**, 1460.
- [90] J. Baumgartl, M. Zvyagolskaya and C. Bechinger, *Phys. Rev. Lett.*, 2007, **99**, 205503.
- [91] C.N. Likos, M. Watzlawek and H. Löwen, *Phys. Rev. E*, 1998, **58**, 3135.
- [92] B. Mladek, G. Falkinger and G. Kahl, private communications.
- [93] C.N. Likos, B.M. Mladek, D. Gottwald and G. Kahl, *J. Chem. Phys.*, 2007, **126**, 224502.
- [94] C.N. Likos and C.L. Henley, *Philos. Mag. B*, 1993, **68**, 85–113.
- [95] F. Ebert, P. Keim and G. Maret, private communications.
- [96] N. Hoffmann, C.N. Likos and H. Löwen, *J. Phys. - Condens. Mat.*, 2006, **18**, 10193.
- [97] H. Shintani and H. Tanaka, *Nature*, 2006, **2**, 200.
- [98] W. Cheng, J. Wang, U. Jonas, G. Fytas and N. Stefanou, *Nat. Mater.*, 2006, **5**, 830.
- [99] J. Baumgartl, J. Dietrich, J. Dobnikar, C. Bechinger and H.H. v. Grünberg, *Soft Matter*, 2008, **4**, 2199–2206.
- [100] T. Still, W. Cheng, M. Retsch, R. Sainidou, J. Wang, U. Jonas, N. Stefanou and G. Fytas, *Phys. Rev. Lett.*, 2008, **100**, 194301.
- [101] U. Jeong, X. Teng, Y. Wang, H. Yang and Y. Xia, *Adv. Mater.*, 2007, **19**, 33–60.
-

Acknowledgements

During the time I spent working on this thesis, I was surrounded by a lot of people who contributed their share and helped me along in these three years. I would like to thank

Gerhard Kahl, for your support and your encouragement, and for providing me with all the skills, tips, and tricks necessary to get a good start in science. I consider myself very lucky to have a supervisor like you.

Christos Likos, for your enthusiasm, which carried me off most of the time, and for making things as simple as they should be.

Federica Lo Verso, for proposing new systems to investigate, for your hospitality during my stay at the Heinrich–Heine–Universität Düsseldorf, and most important of all, your friendship.

Dieter Gottwald the "father of the GA" at the TU Wien, for introducing a wonderful new method and for the time you spent explaining it to me.

Primož Ziherl and Jure Dobnikar, for inviting me to an enjoyable and fruitful collaboration and for your great ideas.

Florian Ebert, Peter Keim and Georg Maret, for the helpful discussions on the experimental realisation of the dipolar binary mixture and for providing me with the snapshots shown in section 6.2.2.

my fellow group members at TU Wien Daniele Coslovich, Günther Doppelbauer, Georg Falkinger, Maria Josè Fernaud Espinosa, Mario Kahn, Jan Kurzidim, Bianca Mladek, and Dieter Schwanzer, for keeping me good company at lunch and during all these long office hours. Especially Bianca, for your counsel and your tips on all the different problems and for a good time at each conference, and Mario, for your help with the layer parametrisation.

the friendly crowd from Heinrich–Heine–Universität Düsseldorf, especially Christian Mayer, Martin Rex and Sven van Teeffelen, for your warm welcome, playing soccer and the trips to the city in the evening.

Martina Jedinger, Gernot Pauschenwein, and Alexander Paulsen, simply for being friends. It means a lot to me.

meinen Eltern, Luise Fornleitner und Josef Krammer, für eure Unterstützung, wann immer ich sie benötige, euren Rat und die Freiheit, meine eigenen Ideen und Ziele zu verfolgen, und zwar in meinem eigenen Tempo und zu dem Zeitpunkt, der für mich der richtige ist. Und auch dafür, dass Ihr mir immer das Gefühl gegeben habt, das wäre selbstverständlich.

Stefan Uttenthaler, for flying more than a thousand miles each month, just to be with me.

This work was supported by the Österreichische Forschungsfond (FWF) under Project No. P17823. Further financial support by the European Science Foundation (ESF, SIMBIOMA - Short Visit Grant 1730) and COST-STSM-P13-2969 (MOLSIMU) is gratefully acknowledged

Curriculum Vitae

Personal Data

Name: Julia Fornleitner

Birth Date: May 14th, 1980

Birth Place: Vienna, Austria

Citizenship: Austrian

Educational History

1986 - 1990 Volksschule Landsteinerergasse, Vienna

1990 - 1998 Bundesrealgymnasium BG XV, Auf der Schmelz, Vienna

1998 - 2005 Studies of Technical Physics at the Vienna University of Technology

2004 - 2008 PhD in Physics at the Vienna University of Technology

Employment History

1999 - 2000 Tutor at the "Institut für Allgemeine Physik", Vienna University of Technology

2000 - 2003 Tutor at the "Institut für theoretische Physik", Vienna University of Technology

2005 - 2008 PhD position funded by the FWF

Don't let it end like this!
Tell them, I said something.
Pancho Villa